

MASTER'S THESIS

**Master's degree in Materials Science and Engineering**

**DESIGN AND STUDY OF SPD PROCESSES; HPT AND MF**

**Report and Annex**

**Author:** Arrebola Bernet, Juan José  
**Director:** Dr. Cabrera, José M<sup>a</sup>  
**Co-Director:** Dr. Zhilyaev, Alexander  
**Semester:** Autumn 2017/2018



## Abstract

This master thesis aims to model the severe plastic deformation through the HPT (High Pressure Torsion) and MDF (Multi Directional Forging) methods in order to determine the necessary external loads. These external loads, see torque and pressure or exerted load, have been calculated through a finite element method and CAE software, and they will be used in a future project to develop a hydraulic torsion press in order to be able to develop the HPT SPD processes in the PROCOMAME (*Procesos de Conformado de Materiales Metálicos*) group laboratories in the EEBE (*Escola d'Enginyeria de Barcelona Est*) faculty of the Technical University of Catalonia (UPC).

The results show the relation between the numbers of turns, torque, load and the effect of those over the material, illustrating the effective strain and stress accumulated along the process. The accumulated torque data is very promising, and shows a saturation in few turns, giving a reliable constant torque with which a hydraulic and torsion machine would be effectively designed, giving, of course, a safe margin of security.

On the other hand, in cooperation with a research group from Autonomous National University of Mexico (UNAM), new state-of-the-art studies have been simulated in terms of a modified HPT processes. The process has the particularity that torsion and compression are applied at the same time, whereas normally pressure is first applied before torsion. The established relationship in México's machine is 1 turn per 5 mm, and the main objective is to obtain the external loads and if the accumulated effective strain would be enough to process an ultra-fine grain material with the expected material properties. As a previous essay, a mechanical buckling effect is analytically performed beforehand in order to avoid this effect due to the small section as a function of sample length. The obtained results show a new possible method to obtain severe plastic deformation materials with a bigger size than other processes avoiding the plausible buckling effect, which is estimated around 40 and 70 mm for Aluminium 1100 depending on the set-up chosen.

Finally, a thermal analysis simulation is performed for the MDF method in order to study the heat flux and its evolution generated along the process and after that, the heat flux dispersion evacuated out of the system.

The results show a great concordance with empirical data obtained in a different master thesis developed in parallel inside the same department, reaching to temperatures of 1°C in the external face of the dies.

## Resumen

Este trabajo final de máster tiene como objetivo la modelización de procesos de deformación plástica severa mediante los métodos de HPT (High Pressure Torsion, o Torsión de Alta Presión) y MDF (Multi-Directional Forging, o Forja Multi-Axial) para poder determinar las cargas externas necesarias. Estas fuerzas externas, véase par motor y presión o carga ejercida, han sido calculadas mediante el método de los elementos finitos y un software apropiado, y serán utilizadas en un futuro proyecto para el desarrollo de una prensa hidráulica con torsión para poder producir la deformación plástica de materiales en los laboratorios del grupo PROCOMAME (Procesos de Conformación de Materiales Metálicos) en Escola d'Enginyeria de Barcelona Est (EEBE) de la Universidad Politècnica de Catalunya (UPC).

Los resultados muestran la relación entre el número de vueltas, par motor, fuerza ejercida y los efectos de estos sobre el material, ilustrando la deformación acumulada y tensiones esperadas durante este proceso. Los valores de par obtenidos son prometedores y muestran una saturación al cabo de pocas vueltas, dando unos valores de par constantes que facilitan el diseño de una futura prensa para HPT, siempre y cuando se acepte un cierto margen de seguridad.

Así mismo, en colaboración con un grupo de investigación de la Universidad Nacional Autónoma de México (UNAM) se han realizado nuevos estudios sobre un método HPT modificado que han arrojado excelentes datos en una máquina donde la torsión y presión se hacen a la vez en una relación de avance de 5mm por vuelta. El principal objetivo era obtener las cargas externas necesarias y analizar si la deformación acumulada y tensiones obtenidas serían suficiente para crear un material con grano ultra fino y con las propiedades esperadas, además de evitar un posible pandeo debido a la relación entre la altura y la sección.

Los resultados obtenidos muestran un nuevo posible método de obtención de materiales con deformación plástica severa con un tamaño más grande de lo que normalmente ofrecen otros métodos SPD evitando el pandeo, estimado en muestras de Aluminio 1100 alrededor de entre 40 mm y 70 mm dependiendo de la configuración.

Finalmente, se ha realizado un análisis térmico sobre un modelo de forja múltiple para estimar el flujo térmico y su evolución a lo largo del tiempo durante el proceso, y después la evacuación de este calor generado.

Los resultados muestran una concordancia con datos empíricos obtenidos en un proyecto desarrollado en paralelo dentro del mismo grupo, llegando a temperaturas de 1°C en las caras externas de los soportes.



## Resum

Aquest treball final de màster té com a objectiu la modelització de processos de deformació plàstica severa mitjançant els mètodes de HPT (Alta pressió i torsió) i MDF (Forja Multi-Axial) per poder determinar les càrregues externes necessàries. Aquestes càrregues externes, vegeu parell motor i pressió o càrrega exercida, han estat calculades mitjançant el mètode dels elements finits i seran utilitzades en un futur projecte per al desenvolupament d'una premsa hidràulica amb torsió per poder produir la deformació plàstica de materials en els laboratoris del departament de PROCOMAME (*Processament i Conformat de Materials Metàl·lics*) en la facultat EEBE (*Escola d'Enginyeria de Barcelona Est*) a l'Universitat Politècnica de Catalunya.

Els resultats mostren la relació entre el nombre de voltes, parell motor, força exercida i els efectes d'aquests sobre el material, il·lustrant la deformació acumulada i tensions esperades durant aquest procés. Els valors obtinguts de parell són prometedors i mostren una saturació al cap de poques voltes, donant uns valors de parell constants que faciliten el disseny d'una futura premsa per HPT, sempre que s'accepti un cert marge de seguretat.

Així mateix, en col·laboració la universitat de Nacional Autònoma de Mèxic (UNAM) s'han realitzat nous estudis sobre un mètode HPT, obtinguent excel·lents dades en una màquina on la torsió i la pressió es fan alhora en una relació de 5mm per volta. El principal objectiu era obtenir les càrregues externes necessàries i si la deformació acumulada i tensions obtingudes serien suficient per crear un material amb gra ultra fi i amb les propietats esperades, a més d'evitar un possible vinclament a causa de la relació entre l'altura i la secció.

Els resultats obtinguts mostren un nou possible mètode d'obtenció de materials amb deformació plàstica severa amb una grandària més gran del que normalment ofereixen altres mètodes SPD evitant el vinclament, estimat en mostres d'Alumini 1100 al voltant d'entre 40 mm i 70 mm depenent de la configuració.

Finalment, una anàlisi tèrmica sobre un model de forja múltiple ha estat realitzat per estimar el flux tèrmic i la seva evolució al llarg del temps durant el procés, i després l'evacuació d'aquesta calor generada.

Els resultats mostren una concordança amb dades empíriques obtingudes en un projecte desenvolupat en paral·lel dins del mateix departament, arribant a temperatures de 1°C en les cares externes dels suports.

## Acknowledgments

To begin with, I would like to thank Homero and Mario, whose dedication and effort at the beginning of the project has helped me to get along with the software and for their great written report (Torres Maldonado and Cadena Hernández 2017) on which the Multidirectional forging sections is based on.

I would like to thank as well the director of this project, Dr. José María Cabrera for his attention, corrections and precisions along the project, which has helped me to develop the present project and to PhD. Alexander Zhilyaev, whose extensive book (Ruslan Z. Valiev, Zhilyaev, and Langdon 2013) has helped me to understand the brand new world that Bulk Nano Materials is, and specifically Severe Plastic Deformation.

And finally but nonetheless, I would like to appreciate the support and help of my wife, Sofia Zaitceva, whose extreme patience and attention has helped me to develop and correct the current report.

Juan José Arrebola Bernet  
Barcelona, 9<sup>th</sup> of January 2018

## Glossary

*BNM – Bulk Nanostructured Materials*

*UFC – Ultrafine-grained*

*NC – Nanocrystalline (materials)*

*NS – Nanostructured (materials)*

*SPD – Severe Plastic Deformation*

*HPT – High Pressure Torsion*

*HPTE - High Pressure Torsion & Extrusion*

*MDF – Multidirectional Forging*

*ECAP – Equal Channel Angular Pressing*

*ARB – Accumulative Roll-Bonding*

*FEM – Finite Element Method*

*PDE – Partial Differential Equation*

*CAD – Computer Aided Design*

*CAE – Computer Aided Engineering*

*DOF – Degrees of Freedom*

*STL – File extension that stands for: Stereo Lithography File*

$\sigma_y$  – Yield Stress [Pa]

$\sigma_0$  – Friction Stress [Pa]

$k_y$  – Constant of Yielding [Pa · m<sup>1/2</sup>]

$d$  – Grain size [m]

$\gamma$  – Torsional strain [rad]

$r$  – Distance from the center of the disk [m]

$d$  – Diameter of the sample [m]

$h$  – Sample thickness [m]  
 $\varphi$  – Torsional angle [rad]  
 $\varepsilon$  – True equivalent strain [–]  
 $a$  – Constant [–]  
 $\tau$  – Shear Stress [Pa]  
 $m_s$  – Constant Shear Coefficient [–]  
 $k$  – Shear strength of the slave material (sample) [Pa]  
 $\mu$  – Coefficient of Friction (Coulomb) [–]  
 $P_i$  – Normal Pressure at the interface [Pa]  
 $P$  – Pressure [Pa]  
 $A$  – Area [m<sup>2</sup>]  
 $F$  – Force/Load [N]  
 $v$  – Lineal velocity/speed [m · s<sup>-1</sup>]  
 $\omega$  – Angular speed [rad · s<sup>-1</sup>]  
 $I$  – Second momentum of Area (or Momentum of Inertiae) [m<sup>4</sup>]  
 $K$  – Constant of buckling model [–]  
 $E$  – Young Modulus [Pa]  
 $L$  – Sample length [mm]  
 $n$  – Strain exponent [–]  
 $m$  – Strain rate exponent [–]  
 $c$  – Constant [Pa · s<sup>-1</sup>]  
 $y$  – Constant [Pa]

# Table of Content

<b>ABSTRACT</b>	<b>I</b>
<b>RESUMEN</b>	<b>II</b>
<b>RESUM</b>	<b>III</b>
<b>ACKNOWLEDGMENTS</b>	<b>IV</b>
<b>GLOSSARY</b>	<b>V</b>
<b>1. PREFACE</b>	<b>1</b>
1.2. Motivation.....	1
<b>2. INTRODUCTION</b>	<b>2</b>
2.1. Objectives of the project .....	2
2.2. Extension of the project.....	2
<b>3. BACKGROUND KNOWLEDGE</b>	<b>3</b>
3.1. Bulk Nanostructured Materials (BNM).....	3
3.1.1. Severe Plastic Deformation (SPD); Idea and process.....	3
3.1.2. Different types of SPD .....	4
3.1.3. Properties of SPD UFG Metals.....	8
3.1.4. Applications and industrial interest .....	8
3.2. Finite Element Method (FEM) .....	9
3.2.1. Finite Element Method description .....	9
3.2.2. Software.....	10
3.2.3. Advantages and Disadvantages of Computer Aided Software.....	11
3.3. Mechanical background.....	12
3.3.1. Coulomb's friction model and Shear friction model.....	12
3.3.2. Buckling.....	13
<b>4. CAE SOFTWARE: DEFORM</b>	<b>15</b>
4.1. Pre-processor study .....	15
4.1.1. Meshing .....	15
4.1.2. Re-meshing.....	20
<b>5. HIGH PRESSURE TORSION: PRELUDE</b>	<b>24</b>
5.1. Pre-processor configuration .....	24
5.1.1. Work piece geometry, material and meshing .....	24

5.1.2.	Anvils geometry .....	24
5.1.3.	Simulation Parameters .....	25
5.1.4.	Results .....	26
5.1.5.	Friction Coefficient Discussion.....	28
<b>6.</b>	<b>HIGH PRESSURE TORSION SIMULATIONS</b> .....	<b>29</b>
6.1.	HPT Cases Introduction .....	29
6.1.1.	Description of the method.....	29
6.1.2.	Experimental and Theoretical Results.....	30
6.2.	HPT Case 1: Semi-Constrained Type B .....	31
6.2.1.	Case Study .....	31
6.2.2.	Results for Copper sample (Ideal case with shear coefficient 2.0; 1 GPa; 1.5 Turns) .....	36
6.2.3.	Results for Copper sample.....	38
6.2.4.	Results for Aluminium sample.....	41
6.3.	HPT Case 2: Unconstrained .....	44
6.3.1.	Case Study .....	44
6.3.2.	Results for Aluminium sample (Ideal Case; High Pressure; 0.5 Turn; 0.61 coefficient) .....	49
6.3.3.	Results for Copper sample (Ideal Case; High Pressure; 0.5 Turn; 0.58 coefficient) .....	56
6.3.4.	Results for Aluminium sample (Real Case; 1 GPa; 4 turns; 0.61 coefficient).....	63
6.4.	HPT Case 3: New simulation process .....	68
6.4.1.	Introduction .....	68
6.4.2.	Case Study .....	70
6.4.3.	Results for Aluminium 1100 sample with depression anvils.....	73
6.4.4.	Results for Aluminium 1100 sample without depression anvils .....	80
6.5.	Comparison between different cases and literature .....	87
6.5.1.	Comparison of strain evolution .....	87
6.5.2.	Comparison of stress evolution .....	90
6.5.3.	Comparison of torque evolution .....	92
<b>7.</b>	<b>MULTI-DIRECTIONAL FORGING (MDF)</b> .....	<b>94</b>
7.1.	Introduction and previous works .....	94
7.2.	Case Study: Thermal Simulation.....	94
7.3.	Results for Aluminium sample.....	98
7.3.1.	Short Term Evolution (Sample heating) .....	98

<b>CONCLUSION</b>	<b>104</b>
<b>SOURCES</b>	<b>105</b>
<b>ANNEX A. MESH AND RE-MESH STUDY</b>	<b>117</b>
A1. Mesh Study 1 .....	117
A2. Mesh Study 2 .....	119
A3. Mesh Study 3 .....	120
A4. Mesh Study 4 .....	123
A5. Mesh Study 5 .....	124
A6. Mesh Study 6 .....	125
A7. Mesh Study 7 .....	129
A8. Mesh Study 8 : Re-mesh evolution .....	131
A9. Mesh Study 9 : Friction Effect .....	133
<b>ANNEX B. TECHNICAL DRAWINGS</b>	<b>134</b>
B1. HPT Prelude & HPT Case 1 : Semi-Constraint B .....	134
B2. HPT Case 2 .....	136
B3. HPT Case 3 .....	140





# 1. Preface

The unceasing and constant evolution and research on metallic materials and its application in industry makes necessary the apparition of new methodologies in the manufacturing processes. The development of bulk nanostructured materials (BNM) has become one of the most promising methodologies to produce new materials with outstanding properties, as, for example, their very high strength, ductility, fatigue endurance and enhanced functions in general (electric, magnetic, corrosion, etc...).

Bulk nanostructured materials can be obtained with two different approaches, the so-called “bottom-up” and “top-down” techniques. In this thesis, the “top-down” approach is followed to the synthesis of the fine grain bulk materials due to the significant development and attention paid to them by the industry over the last years.

“Top-down” approach is based on grain refinement through heavy straining, shock wave loading, etc... and specially by severe plastic deformation (SPD) techniques (High Pressure Torsion (HPT), Multi Directional Forging (MDF), Equal Channel Angular Pressing (ECAP)...) which are object of this study and of huge attraction for commercial production of bulk nanostructured materials as presented in section 2.

The Finite Element Method (FEM) is an outstanding tool for engineers to study, analyse and model beforehand; based on a mathematical model approach, the physical process and resulting product can be estimated, lowering the costs such as time and financial expenses. FEM will be used along this project in order to achieve the best solutions for the designing problems, in order to produce empirical tests in future projects.

## 1.2. Motivation

The motivation of this project is to overview the engineering development process behind an empirical scientific approach with good results, as, for example, previous studies on HPT and MF, to produce a better and more efficient process with the actual machinery as a resource limitation and estimate the capabilities of production, as long to be able to create new machinery.

The necessity of keeping up at the state-of-the-art techniques development to be competitive against different methods motivates as well the necessity of studying new approaches.

## 2. Introduction

This project is a further development of the Sever Plastic Deformation method analysis using Finite Element Method in the PROCOMAME (Metal Forming group) along some other projects in current development or already finished. The final aim of this project is to obtain enough qualitative data in order to proceed in further experimentations with the manufacturing of an empirical experimental design. The specific objectives will be presented in the next section.

### 2.1. Objectives of the project

The specific objectives of these projects are: The simulation of the High Pressure Torsion technique (HPT) by the Finite Element Method (FEM), specifically under two different cases, namely unconstraint HPT and semi-constraint and for a given Al alloy, and the simulation of a Multidirectional forging process for different pure materials; i.e. Aluminium and Copper. Following these simulations, the stress distributions, deformation of the samples and effective strain distribution, as long as resulting efforts will be used to quantify or estimate the necessary external forces necessary for a HPT manufacturing process using the actual machinery in the university and a modification of the actual process of multidirectional forging develop by previous researchers in UPC (Torres Maldonado and Cadena Hernández 2017).

Further simulations on modified HPT processes have been developed as an extension of this thesis with the collaboration of UNAM – México.

### 2.2. Extension of the project

The extension of this project takes from, initially the requirements and solicitations of new processes for severe plastic deformation (multidirectional forging and high pressure torsion), the study of the current techniques, its simulation in order to achieve the necessary efforts to produce such products and the study, design and simulation of these new processes with the whole information to produce fine grain metals following the initial requirements.

### 3. Background Knowledge

In order to understand the present project, the knowledge of some particular topics are required such as Bulk Nanostructured Materials (BNM), Finite Element Method (FEM) and Mechanical background. The following sections are meant to be an introduction to these topics in order to understand further discussions, ( Valiev 2013, Hutton 2005, Callister 2009).

#### 3.1. Bulk Nanostructured Materials (BNM)

Bulk Nanostructured Materials (or BNM) are basically bulk materials, which grain size is below 1000 nm, and with a homogenous distribution of nano-structural elements in the entire sample. The interest of this new metal conformation are various. To begin with, the well know Hall-Petch equation (Eq. 3.1) illustrates that the polycrystalline materials yield stress is highly determined (almost dominantly) by its average grain size ( $d$ ).

$$\sigma_y = \sigma_0 + k_y \cdot d^{-1/2} \quad (\text{Eq. 3.1})$$

This is of the utmost importance, because it follows that the strength increases with the reduction of the grain size, i.e. bulk nanostructured materials have extraordinary high-strength parameters.

Bulk nanostructured materials have other enhanced and interesting properties that will be analysed in the next sections, explicitly for bulk nanostructured materials manufactured by Severe Plastic Deformation (SPD) methods.

##### 3.1.1. Severe Plastic Deformation (SPD); Idea and process

Severe Plastic Deformation is a “top-down” approach, which takes a bulk solid sample with a coarse grain size morphology produce an ultra-fine grained (UFG) material. One of the main advantages of “top-down” approaches compared to the “bottom-up” ones, which is based on the fabrication of materials by assembling individual atoms, is the avoidance of small product size and contamination.

SPD processing does not only refer to one specific methodology, but a various set of experimental procedures of metal forming that produce sever plastic deformation through the imposition of very high strains on materials, leading to a fine microstructure (Pedersen et al. 2015)

One of the most important features of the SPD methodology is that the overall dimension of the sample remains relatively unchanged during the process. Another interesting characteristic is that the shape can be retained by using special tool geometries, preventing a free flow of the material,

which creates in accordance a high hydrostatic pressure. This hydrostatic pressure is necessary to produce the consequent high strain and, eventually, the grain refinement into the ultra-fine grained regime.

### 3.1.2. Different types of SPD

SPD methodology is based upon the procedure of metal forming by imposing very high strains and relatively low temperatures ( $T \leq 0.4 \cdot T_m$ ) without any significant change in the overall dimension of the sample. Normally, to prevent free flow of material, as it was explained in the previous section, special shape retainers (dies, plungers, etc...) are used.

#### 3.1.2.1. High Pressure Torsion (HPT)

High-pressure torsion (HPT) refers to a SPD technique in which the sample is subjected to a high hydrostatic pressure, while it is being twisted by torsional straining. This technique requires of both characteristic loads, static compression and torsion at the same time. These loads are important to be executed at the same time because, as the initial scientific developer of this technique (Bridgman) stated, the material can be twisted in much greater angles without fracture. (Valiev et al 2013)

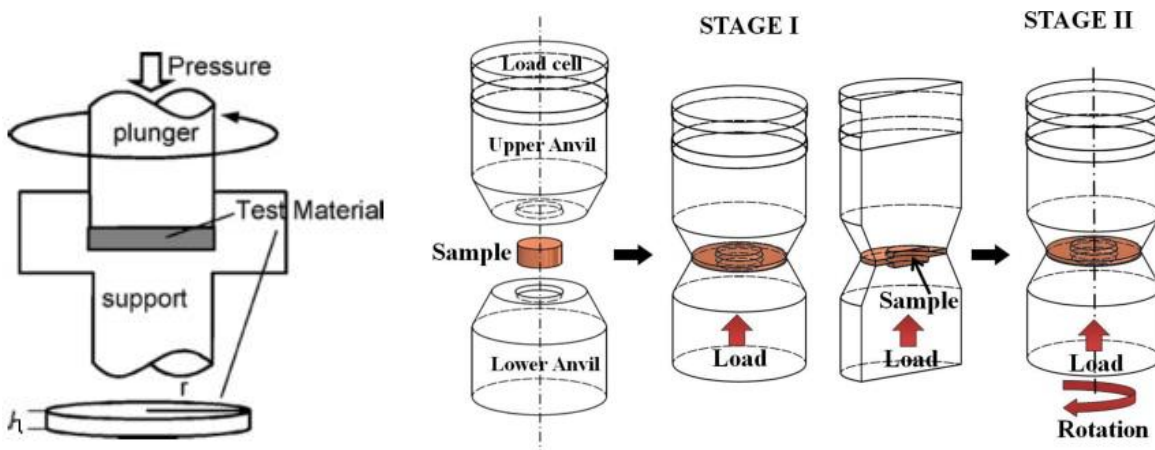


Figure 1. Principle of SPD High-pressure torsion (HPT) method schema (left) and stages (right) (Azushima et al. 2008) and (Stráská et al. 2016) respectively.

The sample, which is normally a thin disk, small cylinder or a ring is subjected under a hydrostatic pressures higher than 1.5 GPa reaching normally 6 GPa. The torsional strain produced over the sample is due to the surface frictional forces, which produce a shear stress and therefore the deformation of the sample. A representation of the process is shown in Figure 1.

One of the main casualties of nowadays SPD processes is that the samples are relatively small due to the necessity of high pressures. If the sample was bigger, the amount of power required by HPT

(for example) would be unachievable. As these small samples have a lack of attractive interest for industry, new studies for bigger bulk materials have been develop as HPTe. (Ivanisenko et al. 2016)

There are two different principles for HPT: unconstrained and constrained. Unconstrained HPT (Figure 2.a) let the material flow outward, which is possible because the two anvils that apply the pressure have no limits for the sample, which produces small backwards pressure.

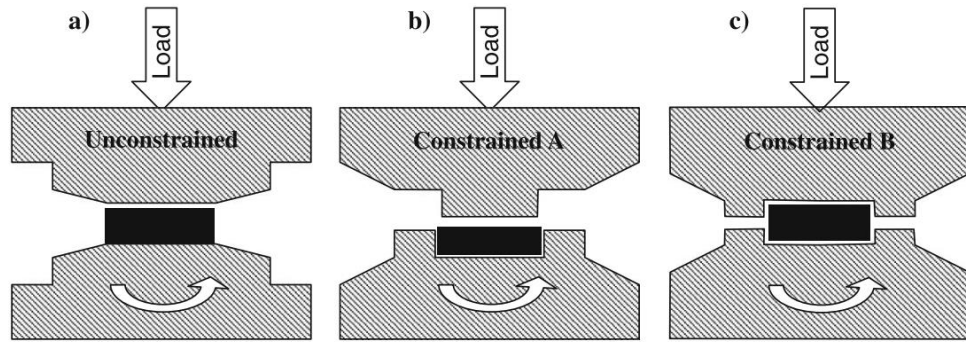


Figure 2. Representation (schematic) of unconstrained (a) and constrained type a (b) and type b (c) HPT process. (Zhilyaev, McNelley, and Langdon 2007)

In constrained HPT (Figure 2.b and Figure 2.c) the sample is prepared in order to suit in the anvil socket and then apply pressure and torsional straining. As the sample is constrained, the presence of an effective back pressure is observed. However, even though the assumption is that the sample is constrained and unable to flow, experiments prove that a limited but still present flow is produced during experimentation due to the difficulty of achieving a perfect seal between anvils and the cavity. (Zhilyaev, McNelley, and Langdon 2007)

In the case of no outward flow of material, the disk thickness remains constant and the true torsional strain ( $\gamma$ ) might be calculated analytically with the following equation (Eq. 3.2):

$$\gamma(r) = \frac{r}{h} \cdot \varphi \quad (\text{Eq. 3.2})$$

where  $r$  is the radius from the disk,  $h$  is its height and  $\varphi$  is the torsional angle.

If an outward flow is assumed (unconstraint case) and a reduction of the sample disk height is assumed, the true equivalent strain ( $\varepsilon$ ) can be calculated using the following relationship (Eq. 3.3):

$$\varepsilon(r) = \frac{1}{a} \cdot \gamma(r) \quad (\text{Eq. 3.3})$$

where  $a$  is equal, in the case of *Tresca* or *Von Mises* assumption, to  $a = \sqrt{3}$  or  $a = 1.65$  for Taylor FCC texture-free metals assumption.

### 3.1.2.2. Multidirectional Forging (MDF)

Multidirectional forging (MDF) refers to a SPD technique in which the sample is subjected to a high pressure free forging operation along different axis through different steps. It can be then unconstrained or constrained, leading then to higher hydrostatic pressures. This technique is used to create ultra-fine grained structures in bulk billets, and occasionally is also carried out at high temperatures promoting classical dynamic recrystallization.

One of the main advantages of MDF is the relatively specific low loads necessary to produce the necessary microstructure, in part due to the temperature interval, set between  $\{0.1 - 0.5\} \cdot T_m$  and the capability of producing relatively large billets with ultra-fine grained, as proven in previous projects of the PROCOMAME group (Torres Maldonado and Cadena Hernández 2017).

A schematic representation of the MDF methodology is described in Figure 3.

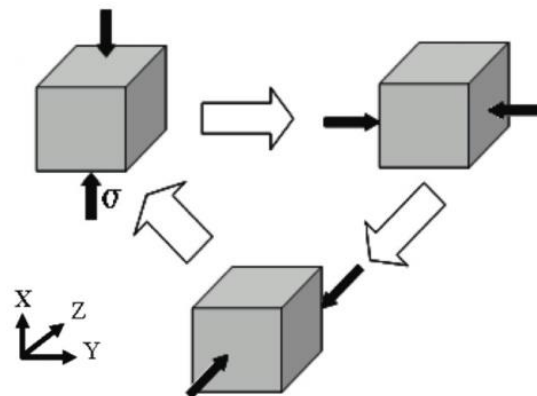


Figure 3. Schematic illustration of the MDF technique. The bold black arrows and  $\sigma$  indicate the forging axes and stress. (Miura, Nakamura, and Kobayashi 2014)

#### 3.1.2.2.1 Other SPD methodologies; ECAP, ARB ...

As it exists not a formal industrial procedure for SPD metal forming, multiple methodologies exist nowadays under research and development aside from High-Pressure Torsion and Multidirectional Forging.

One of the most developed (and early to be studied) is Equal-channel angular pressing (ECAP). The methodology is quite simple to explain: a rod-like sample is introduced into a die with an abrupt angular change, in which the sample, under the pressure from a plunger, much deforms in order to advance. This severe deformation, function of the material, angle of intersection of the equal-channel die, pressure from the plunger, speed... produces an ultra-fine grain material. Through the last decades, the study of this methodology has provided with different variants with advantages and disadvantages in the production of new materials, such as Multi-pass (Xu et al. 2006) or 2-turn (Yousefi Mehr,

Toroghinejad, and Rezaeian 2014), as many others. The following figure (Figure 4) shows a sketch of the basic ECAP process.

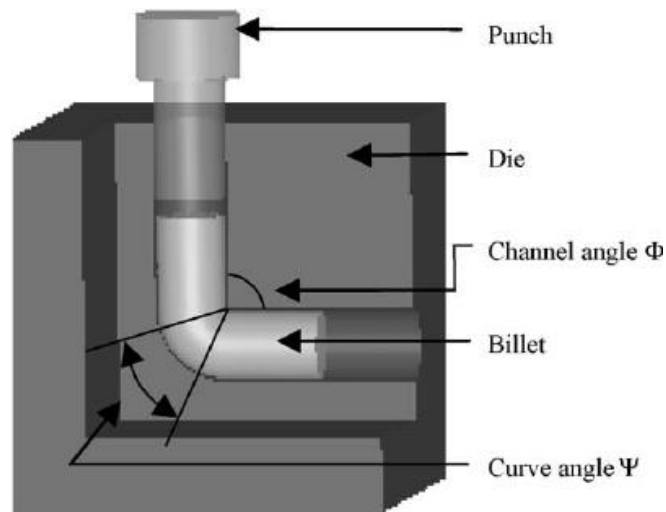


Figure 4. ECAP Schematic process and parts (Xu et al. 2006)

Another well-known SPD method is the Accumulative Roll-Bonding (ARB), in which some metal sheets are roll-bonded together, then divided in two equal sections and bonded again as shown in the Figure 5. The number of cycles (or steps) makes the amount of layers increment in a geometrical way, leading to a huge equivalent strain and therefore an UFG metal.

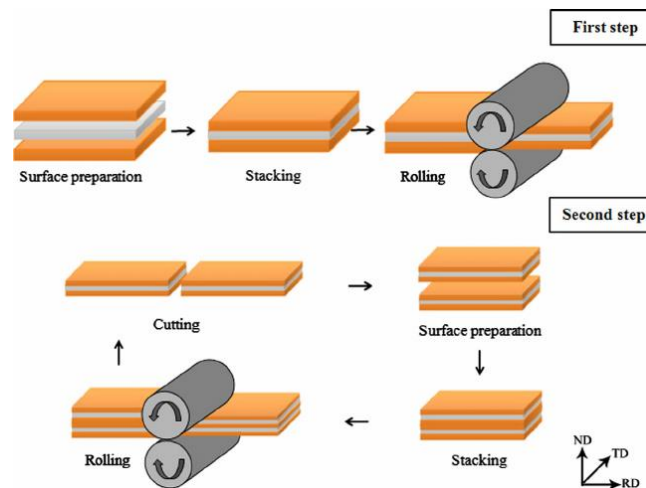


Figure 5. Schematic representation and steps of ARB process. (Yousefi Mehr, Toroghinejad, and Rezaeian 2014)

Still more methodologies under the same SPD principles, even combined processes, have been and are under development today. The lack of industrial production motivates its research to be the most attractive and efficient way to produce ultra-fine grain metals.

### 3.1.3. Properties of SPD UFG Metals

#### 3.1.3.1. Physical Properties

Due to the thin fine and texture that these materials have after undergoing through a SPD processes, important changes on the electrical, magnetic, mechanical, chemical, etc... properties are observed.

For example, there are important changes on the Curie and Debye temperatures, as for the saturation magnetization in function of the materials. Another example is the change of mechanical properties, as, for example, the elastic evolution, which is determined by interatomic interactions. (R. Z. Valiev, Islamgaliev, and Alexandrov 2000)

One of the most important aspects of UFG materials is the enhanced strength compared to conventional materials, which allows to improve already state-of-the-art industrial sectors, as automotive, but with a very important detail as the material is pure and not an alloy.

#### 3.1.4. Applications and industrial interest

Multiple applications have been proposed for high strength and ductile metals, such as bolts, for example, manufactured with titanium alloys by the SPD ECAP technique. These bolts can be used as structural pieces for automobile or aircraft industries.

Other interesting elements are long carbon steel bars or complex shape articles, such as pistons or medical implants, where, for example, pure titanium (which is a biomaterial) and the convenient process that enhances its properties with an ultra-fine grain structure shows itself as a pioneer material for this specific sector.

However, even though all the benefits of these new formed materials, industry is on stand-by for any changes whatsoever. One possible explanation might be the numerous amount of experimental techniques developed during the last decades and the uncertainty of which is the best one to produce industrial batches. On the other hand, the actual available small billet size might be another important issue that must be solved before the SPD techniques reveal themselves as the brand-new metal manufacturing in Industry.



## 3.2. Finite Element Method (FEM)

The description of the physics laws, representing the reality, are described over a space- and time-dependant mathematical problem equations, so-called partial differential equations (PDEs). Most of these equations are not analytically solvable for the specified geometries, assumptions and boundary conditions. Numerical Methods must be applied to solve such equations in order to get results, normally based upon different types of discretization methods.

### 3.2.1. Finite Element Method description

The Finite Element Method, commonly referred as FEM, is reciprocate described as a method based on the discretization of the studied space in finite elements (not to confuse with Finite Difference Method (FDM), based on another type of discretization). (COMSOL 2017)

The space discretisation is function of the dimensional space (i.e. 1<sup>st</sup> dimensional, 2<sup>nd</sup> dimensional or 3<sup>rd</sup> dimensional), for which for every space we have different element description, as shown in Figure 6.

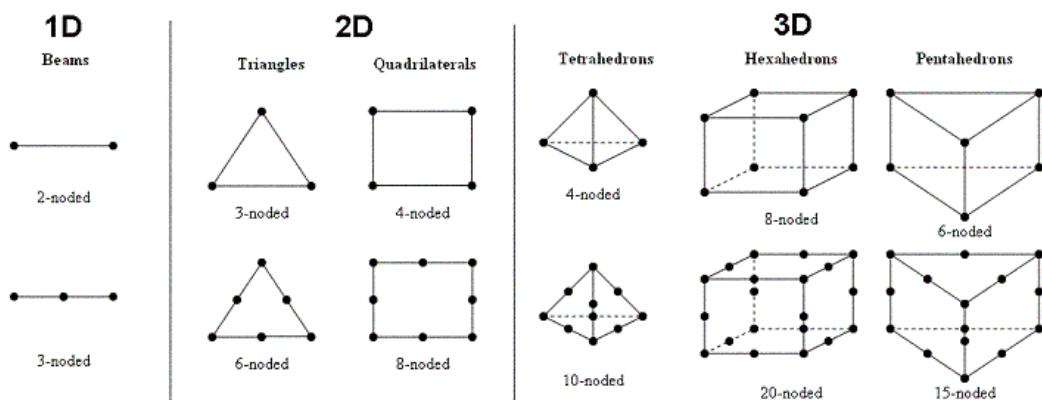


Figure 6. Different Elements in function of the Space Dimension and the amount of nodes (black dots).  
<http://illustrations.marin.ntnu.no/structures/analysis/FEM/theory/index.html>.

These elements assure a discretisation of the continuous medium into a discretised one, in which a discretised version of the PDE equation can be applied and solved for each and every node of the discret space once the boundary conditions are applied.

The solution of the physical laws give very valuable information about how a system is going to behave along time and space in function of the established forces, conditions, material data and boundary conditions. Nonetheless, the given information is as good as the system is modelled and the correct equations under the correct assumptions are applied and a correct interpretation of the results is developed. (Wikipedia 2017b)

### 3.2.2. Software

Nowadays the FEM method is vastly used in the enterprise and research sectors, providing valuable information about different processes and mathematical models. Even though the Finite Element Method is a mathematical based method which can be programmed in each and every programming language, the availability of specific software for different purposes and specific processes facilitates the solution of engineering problems.

#### 3.2.2.1. 3D CAD Software for designing

3D Computer Aided Design Software (CAD) is a suite of programs that facilitates the design of complex geometries. Even though most of the FEM software provides a built-in geometry designer, the complexity of the real geometries forces the use of a specific software in order to achieve a good results simulation.

A huge amount of different software has been developed lately; privative and free, which provides good results, such as CATIA, Solid Works, NX (well-known as Unigraphics) or Creo as the most important ones.

In this project, the software Inventor (from Autodesk distributor) will be used under a student license version. The main reasons for this particular choice are the existence of a license student that covers the whole period of this work and to maintain the continuity of the same software as previous works develop in the same group. (Autodesk 2017)

#### 3.2.2.2. CAE/FEM Software for analysing

Computer Aided Engineering Software (CAE) is a suite of programs that aid on the engineering analysis task. It normally includes different modules within that allows to study different cases such as Finite Element Analysis (FEA), the main study developed in this project, and others, such as Computational Fluid Dynamics (CFD) or Multi body dynamics (MBD). (Wikipedia 2017a)

CAE Software allows the engineers and researchers to analyse a huge variety of magnitudes: stress, stress distribution, deformation, internal and external forces, etc... This values will be quantified and analyse for different processes, mainly the manufacture of multi-axial forging and high pressure torsion over three different materials samples and the study of how this process is developed.

The software to characterize the multi-axial forging and high pressure torsion here used is DEFORM from SFTC (Scientific Forming Technologies Corporation). The main reason is the outstanding performance of this software for characterizing the deformation of metal forming, heat treatment, machining, etc...

### 3.2.3. Advantages and Disadvantages of Computer Aided Software

Even though FEM Software and methodologies are well-appreciated in industry and researchers, there are still a lot of particularities to go through.

The main advantage of the FEM methodology is that it has grown a strong reputation in verification and troubleshooting, as long as a design tool, which provides quite good results reducing the expenses of prototypes or handwork calculations. As well, the facility of producing different laboratory test under different assumptions and boundary conditions allows the designers to expect the reaction of a given design or process.

On the other hand, even though the computer simulations are providing good results to know what to expect and how to proceed, those results are still not enough accurate to omit the physical testing, which is still a must. The accuracy is due to the fact that Finite Element Method is still an analytical numerical solver, which discretise an infinite body in finite parts, performing calculations on approximations. Other element to take in account is the necessity of a powerful computation system and, even though, the computation time is still quite long. Finally, one of the most relevant characteristics is the strongly user-dependency of the FEM simulations: the assumptions, boundary conditions, loads, equation modifications and geometry definition, meshing, type of element, interpolations... make each and every simulation differ significantly, providing different results for the same problem. (de Weck and Kim 2004)

Nevertheless, the use of computer aided technologies has proven to be a must-do in the actual industry, especially in automotive sector where these tools are widely used, reducing time and financial cost as long as improving safety and comfort design, but trying to extend to other sectors, as aerospace, medical, and research areas.

### 3.3. Mechanical background

#### 3.3.1. Coulomb's friction model and Shear friction model

Along the project and after checking different articles and books, some of them are using different friction models in their simulations. In DEFORM v10 exist 3 different types of friction models; shear friction model, coulomb's friction model and the last one is a mix of both, the hybrid method. Following the documentation from DEFORM and literature, the constant shear coefficient model is:

$$\tau = m_s \cdot k \quad (\text{Eq. 3.4})$$

where:

$\tau$  – Shear Stress [Pa]

$m_s$  – Constant Shear Coefficient [–]

$k$  – Shear strength of the slave material (sample) [Pa]

While the coulomb's friction model is established as:

$$\tau = \mu \cdot P_i \quad (\text{Eq. 3.5})$$

where:

$\tau$  – Shear Stress [Pa]

$\mu$  – Coefficient of Friction (Coulomb) [–]

$P_i$  – Normal Pressure at the interface [Pa]

Following the literature, a metal forming process with different finite element model applying the two different models was found (Joun et al. 2009). In this paper it is explained that the Coulomb model describes better the empirical laboratory tests, while the shear coefficient friction is easier to apply due to its simplicity. It is explicit as well that during the compression tests both models follow quite approximately the same curves (as shown in Figure 7), while under shear stress (or under other conditions) the models differ.

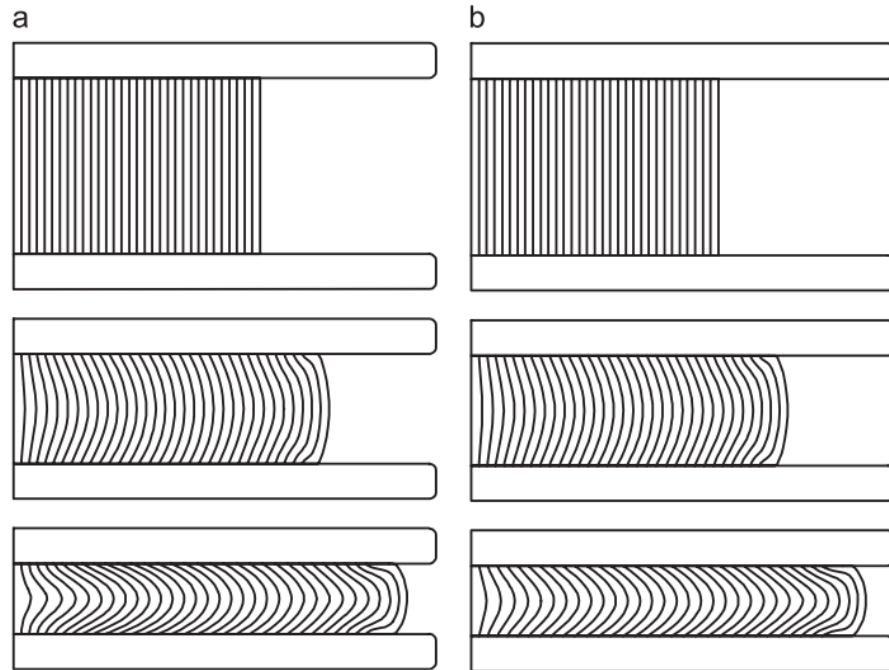


Figure 7. Comparison of metal flow lines formed from compression of the ring with large aspect ratio and large ratio of contact region: (a) Coulomb friction's model and (b) constant shear friction model. (Joun et al. 2009)

Through this study, the Coulomb friction model will be used to obtain real approximate values, while the shear coefficient model will be used for ideal cases due to its simplicity.

### 3.3.2. Buckling

Along this project, new procedures and methodologies were investigated using finite element methods. A set of simulations was requested with a whole new paradigm. The new solicitations were a long and thin metallic rods of a sufficiently long height to produce a buckling. This specification was due to different factor, first the machine that the laboratory has is a screw machine, which produces a revolution every 5 millimetres with no possibility to change so. This specification then obliges to have a 5 millimetre sample height at least for 1 turn, or more if more turns are necessary. The increase of turns increases as well the amount of load that the machine must produce and, obviously, the thickness of the sample. As the load and height are increasing, it is expected to have a critical point, in which buckling effect is produced. To do so, the well-known model of buckling by Euler equation (Eq. 3.6) will be used, along the simulation predicted force and height relationship to obtain the theoretical point, in which buckling is produced.

$$F = \frac{\pi^2 \cdot E \cdot I}{(K \cdot L)^2} \quad (\text{Eq. 3.6})$$

where:

$F$  – Force or Load [N]

$E$  – Young Modulus [Pa]

$I$  – Second momentum of Area (or Momentum of Inertiae) [ $m^4$ ]

$K$  – Constant of buckling model [–]

$L$  – Sample length [mm]

The buckling effect is produced to the impossibility of producing a homogenous distribution of load or a singular mean load applied along an axis, in this case, of a rod. When the relationship between the height of a rod and its diameter is relatively big, this eccentric load produces a bending motion (an elastic instability) over the rod instead of the desired compression. Different parameters and conditions are involved to produce such effect, as for example, the geometry, in which the Length and the second momentum of Inertia have a huge impact, the stiffness of the material has an utmost importance for resisting the bending, and the studied object constraint, as it is not the same to assume that the top and the bottom side of, for example a rod, are constraint, pinned or free. (see Table 1)

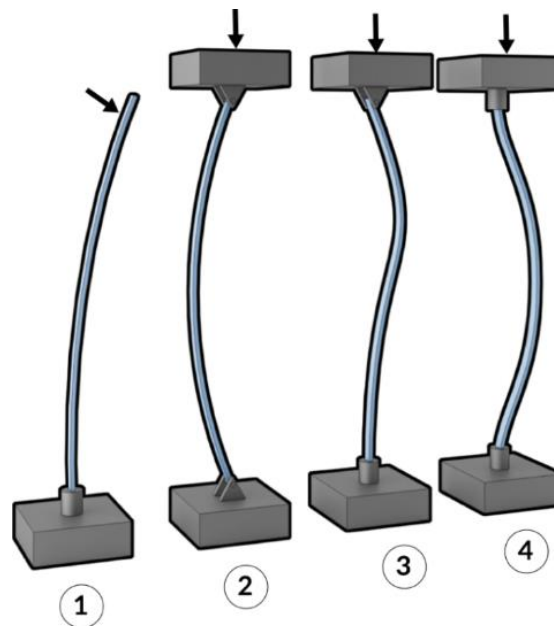


Figure 8. Euler's buckling test samples. (<https://www.manufacturingguide.com/en/eulers-buckling-test>)

Constraint	Both ends pinned	Both ends fixed	One end fixed One end pinned	One end fixed One end free*
$K$	1	$\frac{1}{2}$	$\frac{1}{2} \cdot \sqrt{2}$	2

Table 1. Column Effective Length Factor ( $K$ ) in function of the constraint condition. (\*free to move laterally)

## 4. CAE SOFTWARE: DEFORM

DEFORM is a well-known software for manufacturing and analysing technical process of material deformation. For the purpose of this project, a detailed analysis of the program capabilities, and specially the mesh and re-mesh process, has proven to be of interest due to the huge impact in the final results. The CAE Software is normally separated in 3 different sections or parts, i.e. pre-processor, execution (or experiment run) and post-processor. Each and every section serves in its own way to the production of profitable data.

Pre-processor deals with the geometry definition and position, meshing of the parts, setting up of boundary conditions of the part and between parts, material selection and load conditions. These settings are well-established in the pre-processor, on the other hand, the definition of simulated steps, transient or time-domain simulations and the characteristics of it can be mixed between simulation execution and pre-processor. While the simulation is running, some CAE Software have the capability to re-mesh under certain conditions that trigger such eventuality. The re-mesh is of the utmost importance for the results and its understanding is capital to be able to obtain the expected results.

Finally, the post-processor involves the interpretation, analysis and export of the calculated data.

### 4.1. Pre-processor study

#### 4.1.1. Meshing

The meshing of the work piece geometry has proven to be a challenge with this software due to the lack of options to do so. As explained before in the section Finite Element Method description, it exists different mesh definitions as bricks, tetrahedral, quads and the newest hexahedral discretisation, (Erickson 2012) of which DEFORM only allows tetrahedral to be chosen (bricks option is only allowed for rolling simulations). The incapability to produce a satisfactory meshing only with the automatic mode motivated a preliminary study of the mesh capabilities of the program.

To do so, two theoretical experiments were simulated, the first one a cylindrical block under a uniaxial stress compression of two infinite anvils under two different Coulomb friction coefficient, and the second one two conical anvils were compressing a sample like geometry to check its evolution under two different coulomb friction coefficients as well.

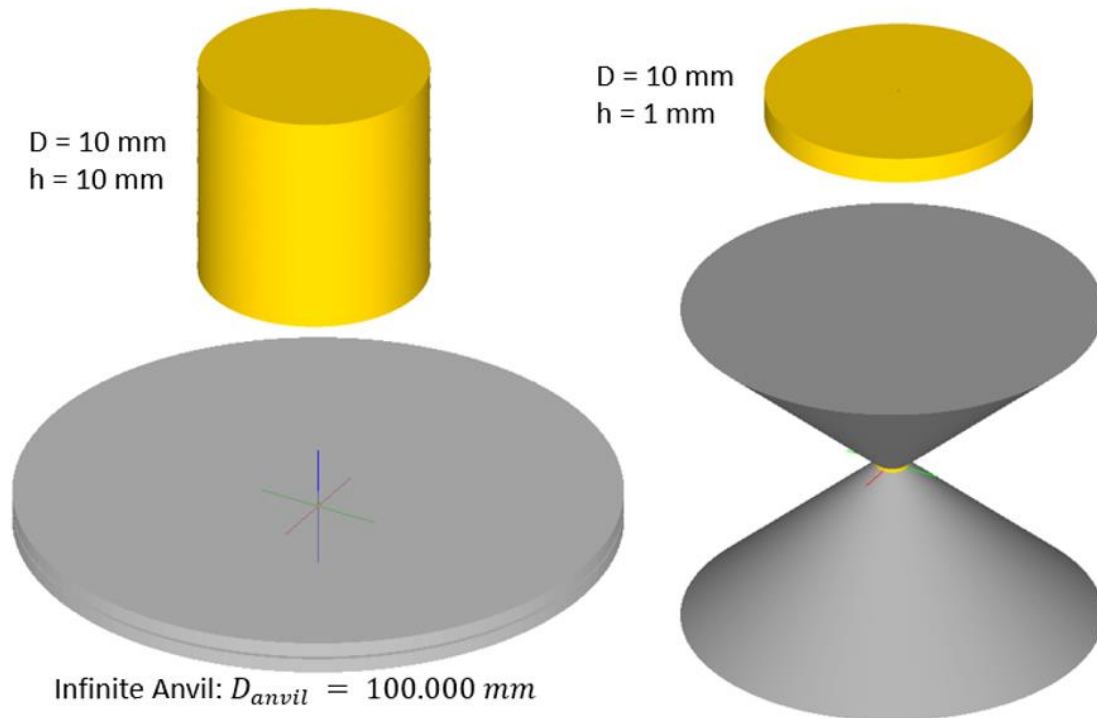


Figure 9. (left) First experiment setup with "infinite-like" anvils and (right) Second Experimental setup with "geometry-like" sample. Units are given in mm.

#### 4.1.1.1. First Experiment: Uniaxial compression of a cylinder within infinite anvils

For the first experiment, once established the geometry as shown in Figure 9 (left), the load condition was set as an hydraulic pressure at 1mm/sec during 1 second (1mm die stroke), the boundary conditions were set as free except the interference between anvils and work piece, which was set as 0 coulomb friction coefficient on first instance, and then at 1. The material was established as Aluminium 1050 from the DEFORM material library. It is expected not to have any effect during the frictionless simulation, but to be relevant when a given friction coefficient.

As the following experiments are following a uniaxial compression and under ideal considerations the true strain equation describes its behaviour quite perfectly, allowing to make a comparison between experimental equations against simulated ones.

$$\varepsilon = \ln\left(\frac{l_0}{l}\right) \quad (\text{Eq. 4.1})$$

With the given parameters, only meshing was left. The integrated 2D3D system manual for DEFORM (Scientific Forming Technologies Corporation (SFTC) 2011) was essential to understand the functions of each and every option and how the software was including the different options. An extended part of this meshing evaluation is presented in the Annex due to its extent. The corollary of the simulations is presented in Table 2.



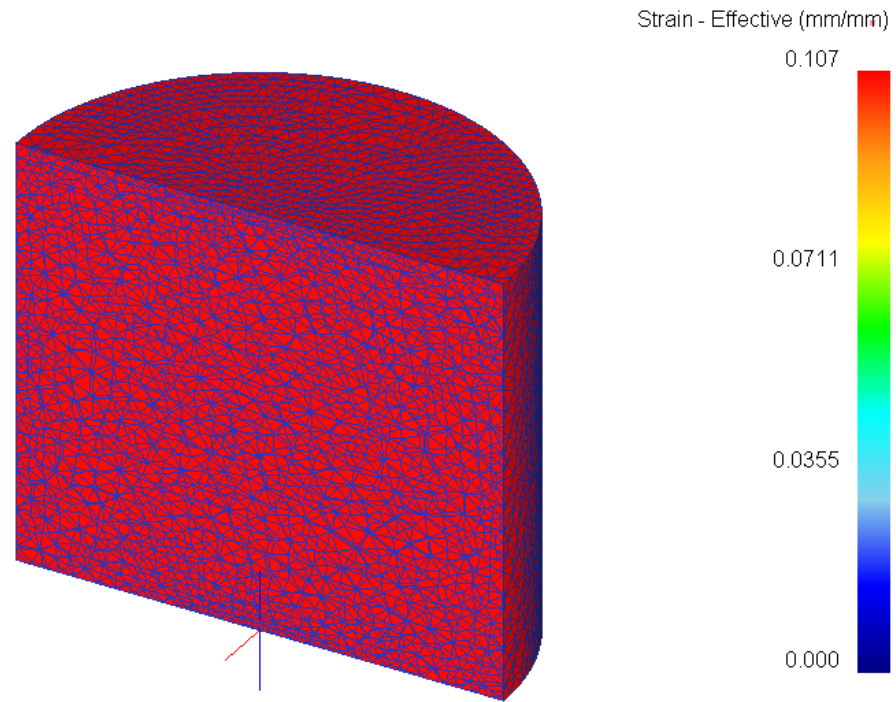


Figure 10. Strain distribution on a cylinder Work piece with Finer Grain Mesh after Ideal (no friction) compression

As it can be seen, the results are in accordance for the case of Coulomb friction 0, which makes total sense due to the fact that the theoretical equation (Eq. 4.1) does not include the friction losses during the uniaxial compression.

**Experiment 1. Coulomb Friction Coefficient set as 0**

	Theoretical True Strain	FEM True Strain	Error
<b>Automatic Mesh</b> without finer internal mesh	0.1054	0.1055	0.13%
<b>Automatic Mesh</b> with finer internal mesh	0.1054	0.1055	0.13%
<b>User defined Surface</b> Mesh with relative element size of 5,4,3 on the top surface, cylinder surface and bottom surface. with finer internal mesh	0.1054	0.1055	0.13%

Table 2. Mesh variances under different cases. Experiment 1: Ideal case.

When the Coulomb friction was set as 1 (which is a high value in order to see the effect of the friction over the simulated sample), the results were completely different. The effect of the flow outwards of the infinite anvils produces a friction between the anvils and the sample, which produces barrelling. This friction (which is held as 0 during the previous simulation) produces a higher strain on the outer ring in contact with the anvil, whereas in the centre, the buckling reduces the strain at zero, as shown in Figure 11.

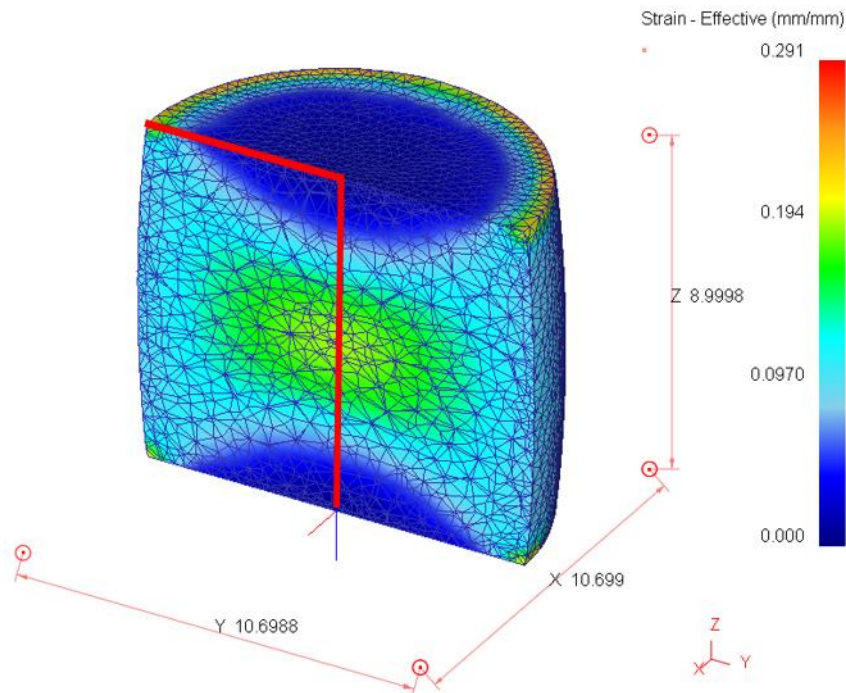


Figure 11. Strain distribution on a cylinder Work piece with Finer Grain Mesh after real compression (establishing Coulomb's friction model between sample and die).

The lack of the true strain homogeneity does not allow to present the data into a table. The results were established exactly as the previous figure for all the simulations, giving the same results with some nuances that were considered as none relevant. What was relevant was the comparison of the mesh with a relative element size of 5, 4, 3 on the top surface, cylinder surface and bottom surface.

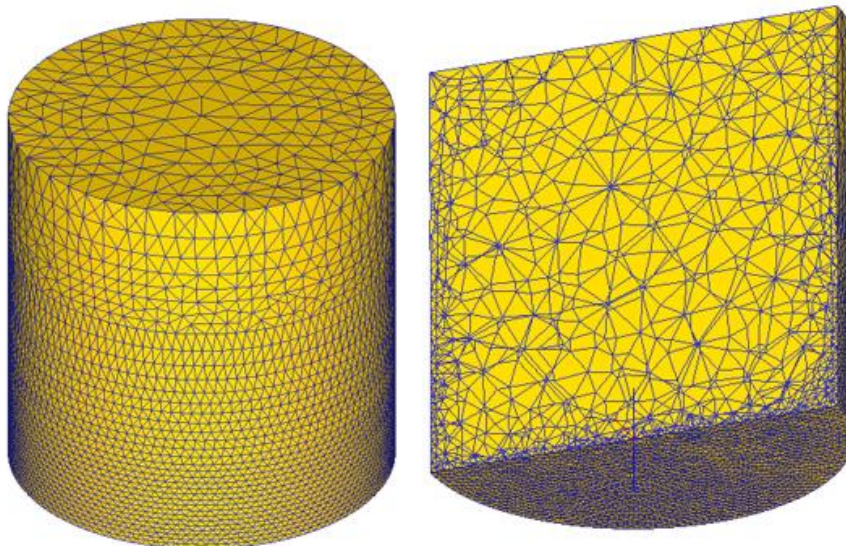


Figure 12. Manual mesh with relative element size of 5,4,3 on the top surface, cylinder surface and bottom surface.

These results are important to mention due to the difference in the outer ring cylinder in contact with the anvils. As shown in Figure 12, the top and bottom element size are completely different and the

results after the simulation (Figure 13) show that the true strain distribution within the sample is qualitatively the same as the one presented before (Figure 11), while the true strain at the border is quantitatively lower. Checking the bottom surface, one can realise that the true strain results are more in accordance with the previous obtained. This is an interesting fact, while it can be observed the dependency of the mesh distribution and the produced results and it will be implemented in further studies.

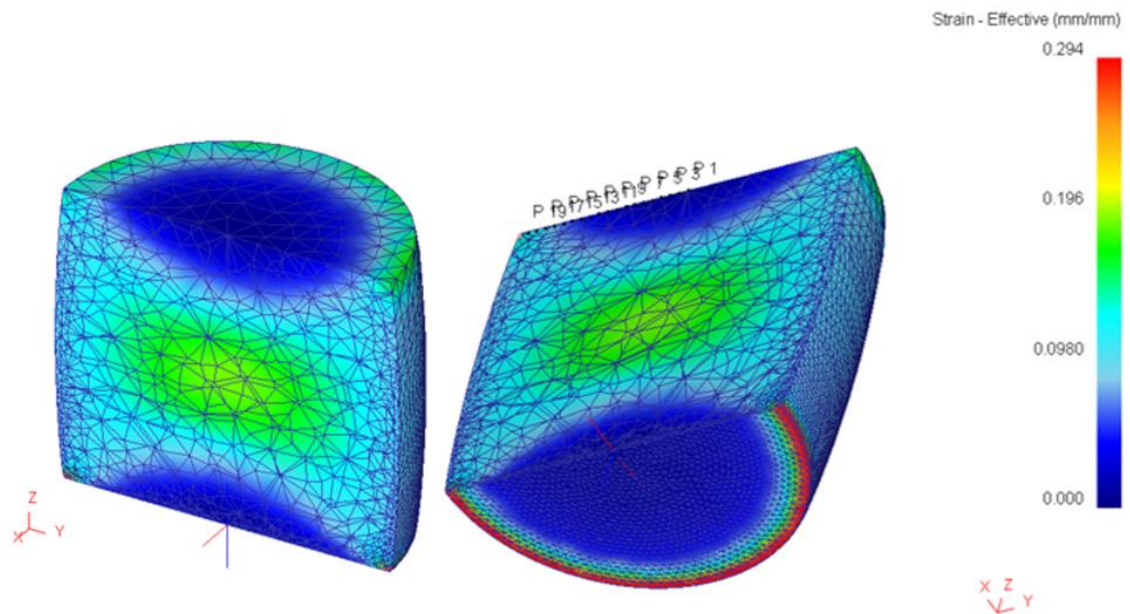


Figure 13. Strain distribution on a manual mesh with relative element size of 5,4,3 on the top surface, cylinder surface and bottom surface.

#### 4.1.1.2. Second Experiment: Two conic anvils over a sample like geometry

Following the first experiment, the established geometry was set as Figure 9 (right), while the load condition was set as an hydraulic pressure at 1mm/sec during 0.1 second (0.1mm die stroke), the boundary conditions were set as free (as the previous case) except the interference between anvils and work piece, which was set as 0 Coulomb friction coefficient on first instance, and then at 1. The material was established as Aluminium 1050 from the DEFORM material library. It is expected not to have any effect during the frictionless simulation, but to be relevant given a non-zero friction coefficient. Given the geometry of the anvils and sample, it is expected to have a free flow out of the anvils, while the load is charging. It was expected as well, given the previous experiment, to obtain the exact same results as the relative length variation is 10/9.

As there is an outflow, it is normal not to have a homogenous distribution at the geometrical border of the anvil as shown in Figure 14. The outer blue-green range is exactly the point where the upper and lower anvil are penetrating the sample, at 5mm radius from the centre.

Experiment 2. Coulomb Friction Coefficient set as 0

	Theoretical True Strain	FEM True Strain	Error
<b>Automatic Mesh</b> without finer internal mesh	0.1054	0.1070	0.14%
<b>Automatic Mesh</b> with finer internal mesh	0.1054	0.1055	0.14%
<b>User defined Surface</b> Mesh with relative element size of 5,4,3 on the top surface, cylinder surface and bottom surface. with finer internal mesh	0.1054	0.1067	0.14%

Table 3. Mesh variances under different cases. Experiment 2: Sample like Geometry

The evolution of the force against time (or stroke) has proven to be dependent on the Coulomb friction coefficient, which is something to take in account during the HPT simulations in terms of pressure and force loads.

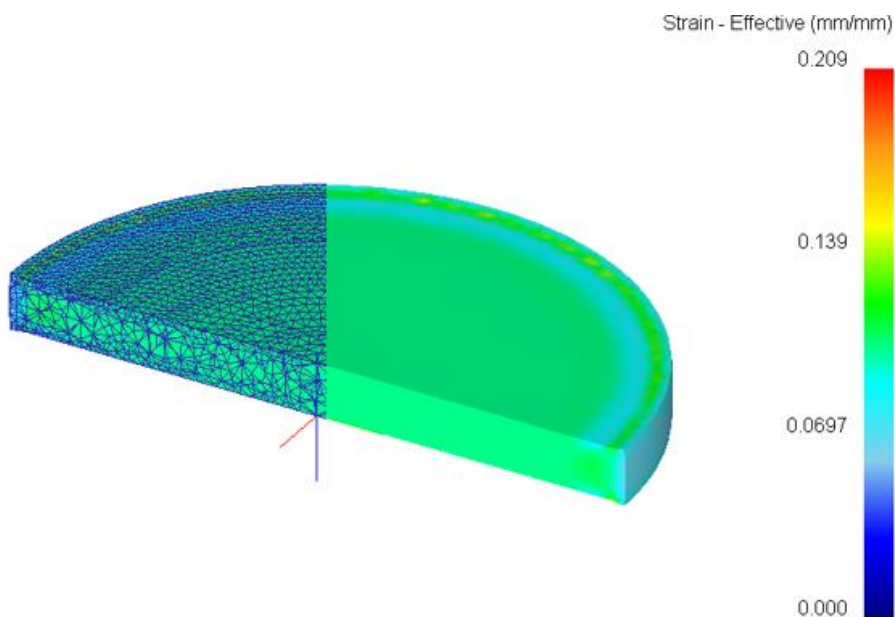


Figure 14. Strain distribution on a disk Work piece with Finer Grain Mesh after Ideal (no friction) compression

#### 4.1.2. Re-meshing

After the meshing study, the automatic re-meshing is an important characteristic of the simulation. The re-mesh will be clearly necessary as the torsion increases and might be necessary for the compression. This can be implied as the elements through the compression will suffer a compression of the element mesh, but it cannot be determined if this relative element transformation will be enough to trigger a re-mesh or not, whereas during the torsion, the outer elements will suffer (if set a torsion at 1RPM during 1 minute) a complete turn along the z-axis. That means that the outer elements

will enlarge more than the relative set-up mesh, proceeding with a re-mesh, which will change the initially set-up mesh.

Along this section, all the possible FEM software options were studied and analysed in order to achieve the best mesh for the simulation. To do so and following the previous section (4.1.1.2), an extreme compression from the two conic anvils over the sample like geometry was studied. The main reasons to proceed from these points are various: first, the sample geometry will give interesting results for further simulations and second, the free outflow with no stress neither strain changes is an interesting case in which the mesh and re-mesh should be not as important as the compressed and torsioned one under the pressure of both anvils.

#### **4.1.2.1. Re-mesh experiment: Two conic anvils compressing a sample like geometry until re-mesh**

Following exactly the same configuration as the previous section, the simulations proceed until the 0.8 mm compression, triggering a re-mesh. After reading the concerning chapter of the DEFORM documentation, a different set of experiments is set-up to check the evolution of the re-mesh.

The first option to take in account is the re-mesh trigger, which has two different options, given an absolute or a relative elemental evaluation. Absolute options are triggered when a given element in the mesh exceeds the absolute set-up value, so if the mesh is set up to be 0.1 mm size maximum and the element exceeds a given 0.7mm maximum, the re-mesh is triggered, whilst the relative one just takes in account the relative interference depth of each and every element compared with the initial mesh one. Other absolute parameters can be defined, as for example a maximum stroke, time or step increment.

The second option is the way that the re-mesh is performed. There are two methods in DEFORM, global and local re-mesh. Global re-mesh performs a whole mesh for all the elements along all the work piece, while local re-mesh performs a new mesh especially in the localised zone where the re-mesh was triggered. Global re-mesh has no further options once selected, while local re-meshing offers the possibility to control the size of the local re-mesh and the scaling factor.

A full set of experiments was performed to check the re-mesh elements evolution and the mesh distribution, especially along the thickness of the work piece. The results are presented in the following table.



	<i>Amount of elements</i>		<i>Relative elements loss</i>
	Before re-mesh	After re-mesh	
			<i>Global Re-meshing</i>
	35.917	11.991	67%
			<i>Local Re-meshing</i>
<i>Average Neighbour</i>	35.917	14.382	60%
<i>Scaling factor 0.8</i>	35.917	11.728	67%
<i>Scaling Factor 1.2</i>	35.917	13.398	63%
<i>Scaling factor 1.5</i>			
<i>+ Avoiding good element shape</i>	35.917	11.827	67%
<i>Scaling Factor 5.0</i>	35.917	11.928	67%
			<i>Manual Re-meshing</i>
	35.917	35.603	01%

Table 4. Element loss under different cases under different re-meshing functions

As the results were not satisfactory, further studies were carried on. The first solution was to proceed with a manual re-mesh stopping the simulation right after the simulation was triggered to re-mesh. The results were satisfactory, giving the capability not to only set up the same amount of elements, but to control as well the distribution. An example can be seen in Figure 15.

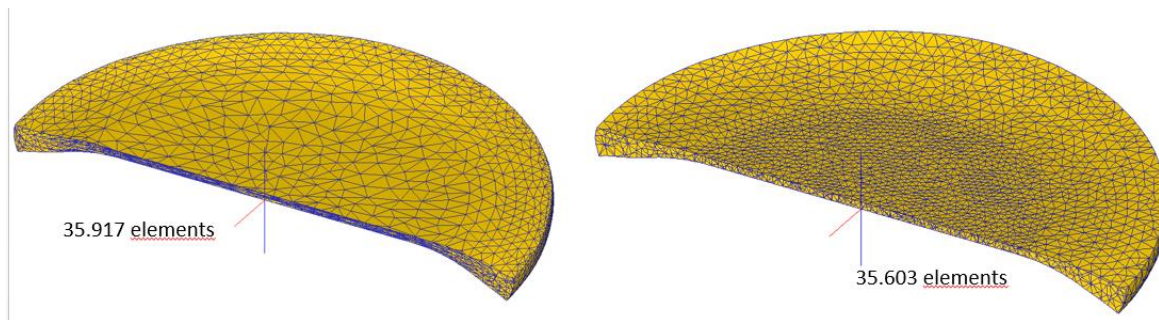


Figure 15. Manual mesh.

It was set-up as well a detailed option of the mesh settings that had no impact in the initial mesh generation, weighting factors, which uses the interpolated data from the simulation (that is the main reason why it has no effect at initial mesh) to perform a better mesh setting up the weight of the factor from 0 to 1. The weighting factors are: Surface Curvature, Temperature Distribution, Strain Distribution, Strain Rate Distribution and Mesh Density Windows. This last factor is the only one to have effects at the initial and not-initial mesh.

Mesh Density Windows allows the user to perform multiple cylindrical, cubic, tor or polygonal volumes, with which the user can define the mesh size in each and every volume container as shown in Figure 16.

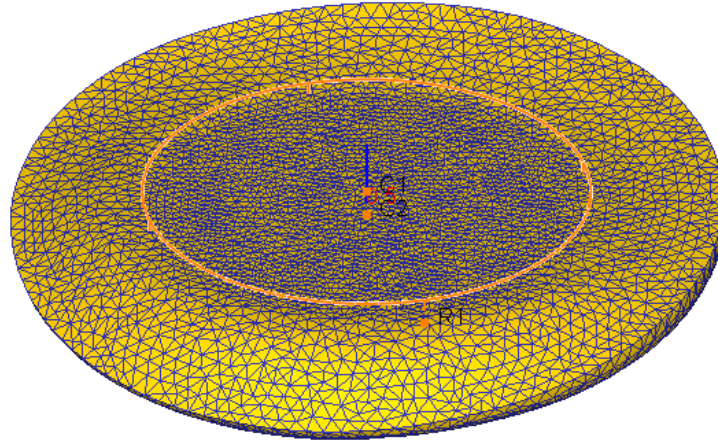


Figure 16. Manual mesh with a cylinder window meshing equiaxial and with 10mm diameter.

This is an extremely resourceful tool, which will allow to set a high density mesh at the outer circle of the tor simulation, where is obvious that the strain is maximum due to the linear speed relation along the angular speed and distance from the centre (Eq. 4.2).

$$v = \omega \cdot r \quad (\text{Eq. 4.2})$$

where:

$v$  – Lineal velocity/speed [ $m \cdot s^{-1}$ ]

$\omega$  – Angular speed [ $rad \cdot s^{-1}$ ]

$r$  – Distance from the center of the disk [m]

## 5. High Pressure Torsion: Prelude

Before starting to do the simulations on purpose, an extensive research about Finite Elements Methods, Constraint, Quasi-constraint, High Pressure Torsion and Severe Plastic Deformation was carried out. Through this research, a very interesting article was found: *Using finite element modelling to examine the flow processes in quasi-constrained high-pressure torsion* from Roberto B. Figueiredo and co-workers. (Figueiredo, Cetlin, and Langdon 2011)

In the article, some Finite Element Method simulations are performed over a HPT Constraint (type B) with the Deform v10. The purpose of the article is to find out the relation between the friction coefficient between the anvils and outflow, evaluating the effective strain, mean stress, velocity and torque. As the simulation is performed with the same software as in the present project, it was interesting to check the validity of the simulations, parameters and mesh conditions with other literature results to verify that the modelling is correct.

Other reason of interest is the use of the shear coefficient instead of the common model, the Coulomb friction model, with which after getting the same results as the paper, can be used to establish a correlation between the shear coefficient and the Coulomb one.

### 5.1. Pre-processor configuration

#### 5.1.1. Work piece geometry, material and meshing

The sample to study is a 10 millimetre disk with a 0.8 mm height. The material that was used by Figueiredo was a pure copper following the flow stress given in the equation (Eq. 5.1).

$$\sigma = 340 \cdot \varepsilon^{0.25} \quad (\text{Eq. 5.1})$$

As the flow stress follows quite approximately the data from the CDA110 Copper 99% of purity registered from the material library, this was established as the model material.

In order to achieve the same results, a ~35.000 elements mesh was established as in the mentioned paper.

#### 5.1.2. Anvils geometry

The anvils are defined as two similar rigid tools with a 10 mm depression at the axial centre of 0.25 depth each. The depression walls are established as inclined from the vertical with a 45°. A 3D model of the upper and lower anvils can be seen at Figure 17.



The 3D model was created with Autodesk Inventor and then exported as a *stl* file. Different casualties that the author considers of interest were found along the import process. The first one was the wrong dimension of the piece. Even though the piece was measured and established in millimetres in the CAD program, DEFORM imported the file as a different unit system, resulting in incongruences with the sample. The second casualty was the definition of the cylindrical anvils. As a cylinder is formed by a succession of infinite planes, the export/import process limits the number of planes during the process, which produces a rough model, not suitable for simulation, especially for the depressions of the anvils.

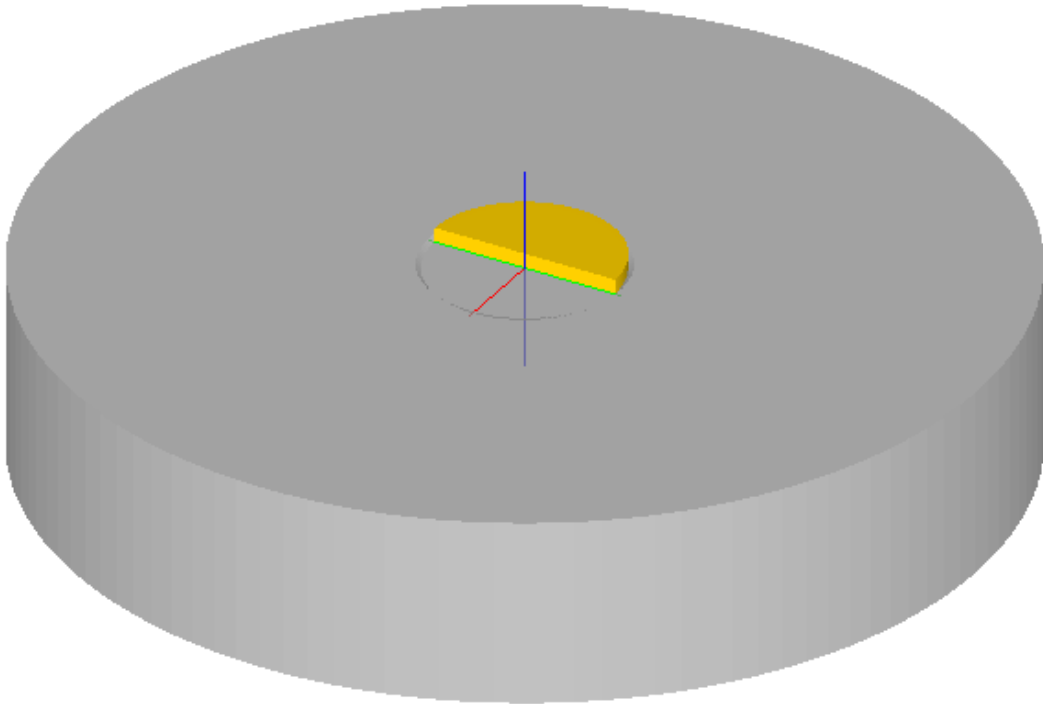


Figure 17. DEFORM Port-view of the sliced sample over the lower anvil depression.

DEFORM has another tool which allows to create geometries from revolutions of sketches. This was a very effective way for modelling the anvils with a huge control of the surfaces, as it includes an option for setting up the amount of external surfaces.

### 5.1.3. Simulation Parameters

Most of the parameters for the simulation were extracted from simulation, as the loads: 39.270 N, 78.540 N and 157.080 N, which are equivalent to 0.5 GPa, 1 GPa and 2.0 GPa. This is clear if we use the simple equation (Eq. 5.2) relating pressure and area, establishing area as the area of a 10 mm diameter circle.

$$P = \frac{F}{A} \quad (\text{Eq. 5.2})$$

The revolutions of the lower anvil is set as a 1 revolution per minute and the amount of turns is set up as a 1.5 total turns (560°).

The last parameters to be shown explicitly in the article are the shear coefficient. As the main aim of the research was to investigate the effect of the outflow friction with the anvil faces, different shear coefficients were established, such as 0, 0.5 and 1.0. Inside the depression, a constant shear coefficient of 2.0 was established, arguing that a rough surface with a huge friction is seek to favour the sticking condition between the anvils and the sample. To do so, a very specific tool called “friction window” inside the friction condition was used. The purpose of this tool is to specify a window (under the geometrical form of a cube, cylinder or tor) in which the friction coefficient at the nodes can be established.

Given all the parameters, there were still some parameters that had to be established by trial and error. The first one was if the sticking condition was established or not. The sticking condition is a very extreme case in which the nodes from the anvils and the samples are established as a rigid boundary. After different simulations, it was established that the sticking condition was indeed applied. The second parameter to be discovered was the friction window size, as it was not explicitly said if the depression walls were included or not, different simulations were performed to discover that they were included. The last setting to be fixed was the compression test. DEFORM has multiple ways to apply a load, varying from imposing the force directly, a mechanical pressing, hydraulic pressing, etc... After different simulations, it was established that the force was directly imposed.

#### 5.1.4. Results

After an extensive set of simulations, the results were obtained in a good accordance with the article by Figueiredo, as it can be appreciated in the strain comparison (Figure 18).

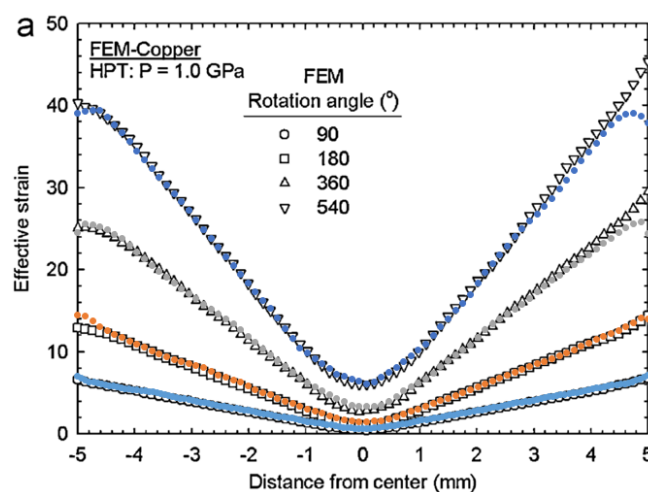


Figure 18. Strain evolution along the distance from the centre based on literature (black and white) and comparison with simulation results (colour)

As it can be seen, the colour lines are the obtained results, and the black and white are the results from the literature. It can be observed that the produced results are following the same pattern as the article simulation (Figure 19, Figure 20). It is shown as well that for lower rotation angles the results are better than for the higher rotation angle.

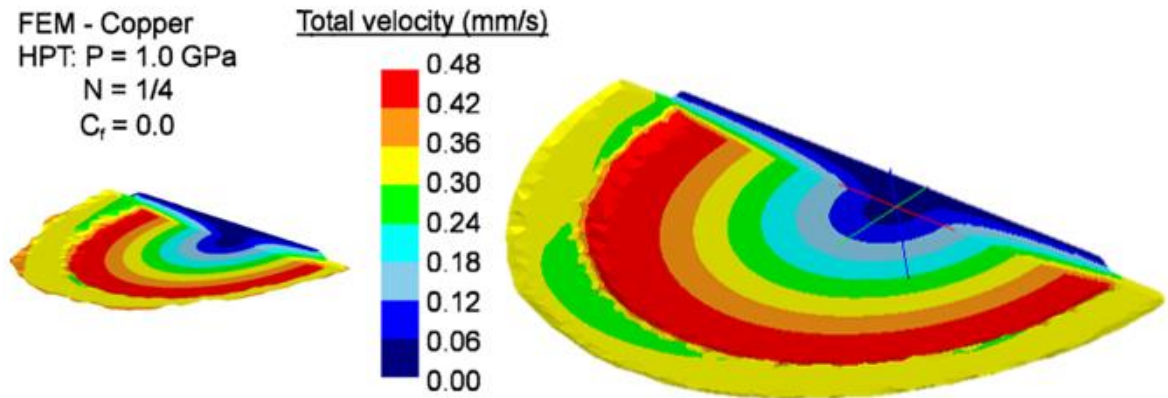


Figure 19. Total velocity comparison between literature (left) and simulation (right).

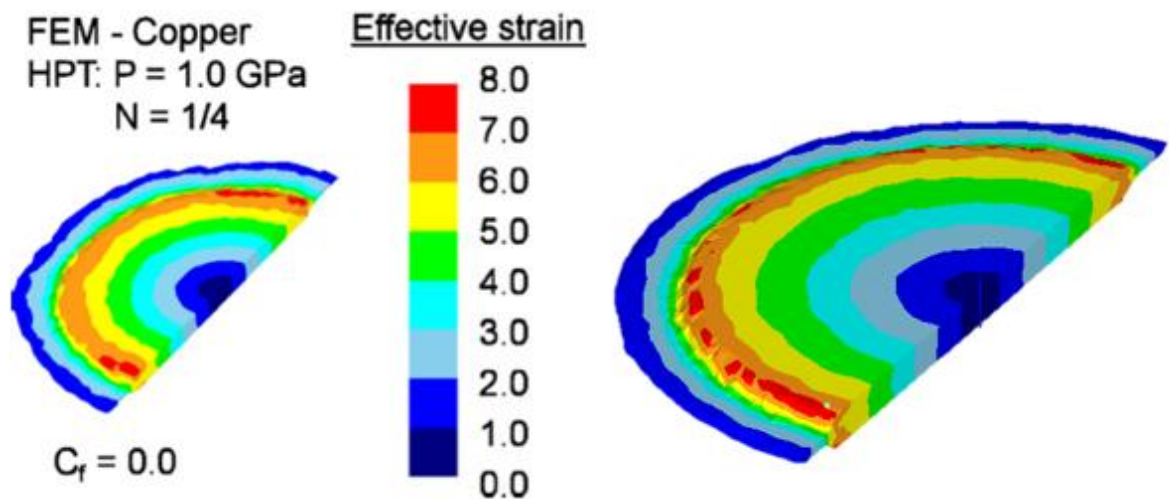


Figure 20. Effective Strain distribution comparison between literature (left) and simulation (right).

It can be assumed that if the mesh is not homogenous, so the results are not homogenous as well. As the article does not say explicitly along which path coordinates of the surface the strain results are obtained, it cannot be exactly reproduced. It can be explained as well that, as the mesh is a software dependant process, governed by the user to have the exact same results, unless exactly same conditions are used.

### 5.1.5. Friction Coefficient Discussion

Once results are similar and once all parameters are well established, it is the moment to change only one in order not to be affected by the other ones. The parameter to study is the friction coefficient, established as a shear coefficient with a value of 2 in the paper. The aim of this section is to establish a relation between the shear coefficient and the Coulomb's friction coefficient. To do so a mathematical bisection-approach will be applied. As it is well known that Coulomb's friction value 0 is established as total slippage and value 1 is established as an almost sticking condition (even though higher than 1 values might exist), a 0.5 value was set as a beginning point. It was assumed that if there was more slippage than the simulation to compare, the coefficient friction was not high enough, and if the value was to be more restrictive than the compared one, then the coefficient was higher than its equivalent one.

After several simulations, it was established that a shear coefficient of 2 is roughly equivalent to a Coulomb's coefficient friction of 0.6 – 0.7 under a 0.5 GPa compression, as shown in Figure 21.

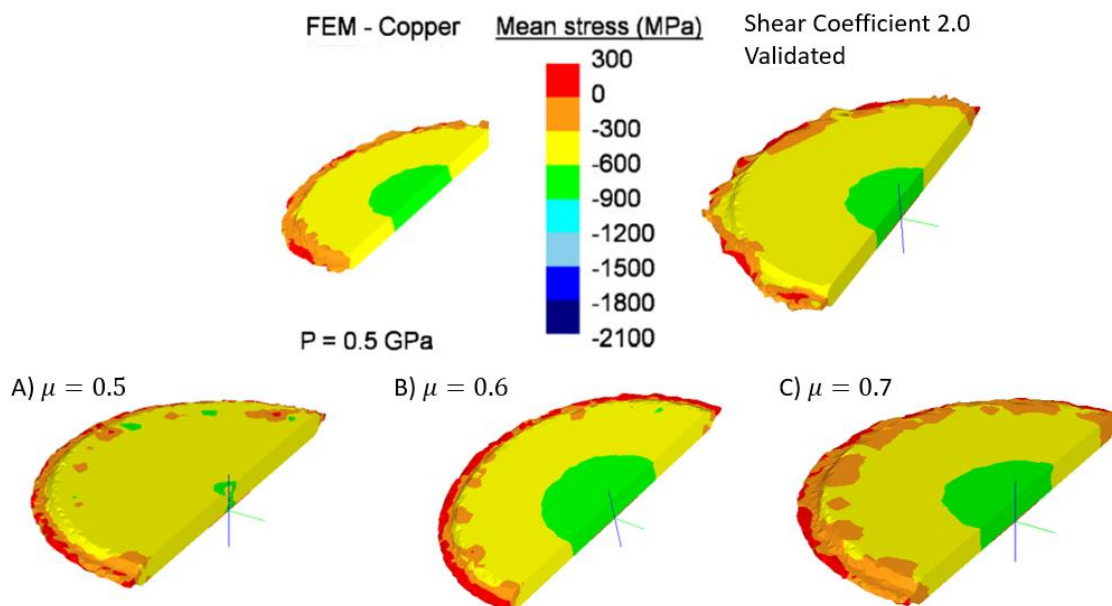


Figure 21. Mean stress distribution of literature model (top left) and obtained simulation with 2.0 shear coefficient model (top right) and comparison with Coulomb's friction model with coefficients 0.5 (A), 0.6 (B) and 0.7 (C).

There was no correlation between the 0.5 GPa, 1.0 GPa and 1.5 GPa simulations after 1/4 turn for any other Coulombs friction. The results were therefore in good accordance with the results obtained in literature presented in section 3.3.1.

## 6. High Pressure Torsion Simulations

### 6.1. HPT Cases Introduction

In the following section the description of the High Pressure Torsion under two main assumptions and two different materials will be presented. The two main assumptions are that the sample is unconstrained and semi-constrained type B (see Different types of SPD), while the two elected materials are Aluminium and Copper.

Early studies proved (R. Z. Valiev, Islamgaliev, and Alexandrov 2000) that the homogeneity of the sample is a function of the pressure and, mainly, of the number of turns under a constant pressure. To characterize the expected microstructure as a function of the number of turns and the amount of torque necessary to produce them, the Finite Element Method is presented as a very resourceful tool.

Due to the amount of variables that laboratory experiments might present and the geometrical evolution that it follows with different combinations, the following discreet variables (Table 5) have been selected due to their importance on the sample stress distribution and hardness as proved in previous studies.

<i>Variable</i>	<i>Value</i>	<i>Magnitude</i>
<i>SAMPLE GEOMETRY (thickness)</i>	{0.8, 1.0}	[mm]
<i>PRESSURE</i>	{0.5, 1.0, 2.0, 6.0}	[GPa]
<i>TURNS</i>	{0.5, 1, 2, 3, 4}	[ REV ]
<i>FRICTION COEFFICIENT MODEL</i>	{Coulomb, Shear}	[]

Table 5. Selected discreet variables, units and values for the following simulations.

The development of the following simulations is expected to illustrate a behaviour pattern that leads then to more simulations with different cases, which might augment the amount of experiments with different parameters.

#### 6.1.1. Description of the method

The constrained HPT process is carried in a screw machine or a mechanical/hydraulic press with a torque engine. Normally, the sample is set between two anvils, the upper one and the lower one. The upper anvil is mobile in its vertical axis and connected with the hydraulic press. The upper anvil is the one that establishes the pressure over the sample. The lower anvil is normally only mobile by its rotation along the vertical axis. It is normally connected to the torque machine and it is the one that produces the torsion over the sample.

There are several distributions for HPT machines; as, for example, the pressure can be applied by either anvils, or just the inferior one, it can be compressed at the same time that it is rotating, etc...

### 6.1.2. Experimental and Theoretical Results

Following previous researches, it is expected to find a homogenous microstructure when the number of turns over the sample is increased, even though it is interesting as well the fact that this homogenous structure is reached faster at lower pressures (Ruslan Z. Valiev, Zhilyaev, and Langdon 2013). The following experimental evidence motivates the study of the evolution of the microstructure in function of the number of turns, which can be interpreted as the amount of applied strain, as well as the applied pressure, understood as well as the amount of applied stress.

It has been also observed that when the microstructure is already homogenous, the increasing number of turns lowers its effect on the microstructure, which will be studied as well with the Finite Element Method and DEFORM software.

It can be interesting to compare the obtained results for the simulation with the one that were obtained in the previous simulation from the section High Pressure Torsion: Prelude.

#### 6.1.2.1. Material and Properties

Following the previous section, the selected materials are Aluminium and Copper and their room temperature mechanical properties are the following ones:

	<i>Young Modulus</i> [GPa]	<i>Poisson's coefficient</i> [-]	<i>Yield strength</i> [MPa]	<i>DEFORM Library</i> <i>id material</i>
<i>Aluminium</i>	68.9	0.33	28	AL1050COLD
<i>Copper</i>	115	0.33	69	CDA110
<i>Steel Tool AISI H13</i>	210	0.30	1650	AISI-H13

Table 6. Material properties for the samples and dies and DEFORM v10 integrated material library equivalent.

The material properties are obtained from the FEM Materials library, which are in good accordance with other handbook publications (Henry et al. 2001; ASM International Handbook 1990), and in which the following materials are well documented and characterized.

For example, the specific handbook, from where the Aluminium 1100 data was extrapolated, was Battelle Technical Report No. 9, Sept. 1981, Review of Flow Stress (ASTM 1050A) by Hoptner H.G., "The Compressive Behaviour of Aluminium Alloys", Dissertation TV Hannover, 1968 for which the composition was established as: Si = 0.92, Cu = 0.01, Mn = 0.026, Mg = 0.033, Zn = 0.01, Fe = 0.23, Al = Balance.

## 6.2. HPT Case 1: Semi-Constrained Type B

The particularity of the semi-constrained type B is that the material outflow is constrained due to the geometrical disposition of the upper and lower anvil, which creates a back stress over the anvils.

### 6.2.1. Case Study

Multiple case studies have been elaborated following the parameter inputs of the Table 5, with which different results have been obtained. These multiple studies were useful to determine the effect of each of the define parameters and its importance over the obtained microstructure and external loads.

The next subsection will reflect the most important effects of those parameter definition and justification, along their results and effects, leading to a better understanding of the process and, finally, their optimization.

#### 6.2.1.1. Geometrical Model

There are 3 given parts with geometrical definition, the upper anvil, the lower anvil and the sample. The sample must follow the specifications that were defined at the beginning of the project, a disk of 10 mm of diameter and an established height of 1 - 0.8 mm. These solicitations are motivated as most of the literature and researchers are using this geometry specifications with good results.

The bottom die and punch had no restrictions in its conception, so different assumptions were established for their development, which are:

- The models must enter dimensionally in the current hydraulic press in the laboratory.
- The models must withstand the maximum load that the hydraulic press can deliver.
- The models must portray their duty within a safe coefficient.
- The models must be optimize for economic and ecologic purposes.

Different models have been developed following the previous solicitations and which produced different results in terms of stress distributions, volume and other mechanical properties.

### 6.2.1.2. Sample Geometry

The sample or work piece to develop has established dimensions required from the research group. It has been established that all the material samples (Aluminium and Copper) must be a primitive round cylinder with a 10mm diameter and 0.8 mm or 1 mm thickness.

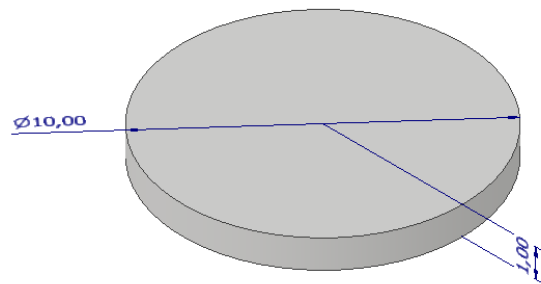


Figure 22. Sample CAD model (Autodesk Inventor) with technical data. Thickness can be 1.00 mm or 0.80 mm

### 6.2.1.3. Upper and Lower Anvil Geometry

The upper and lower anvils are exactly the same model, but mirrored along the z plane so the depressions contain the sample. The geometry of this anvil is based on different papers, which identify this dimension as the optimal for HPT semi-constrained type B for the previous sample dimensions. The depression is characterised as a 0.25 mm depth cylindrical hole with a 10 mm base set coaxial to the die axis and with a depression wall of 45° inclination. This configuration has proven to be optimal for the HPT, because as the sample is being compressed, the material is flowing due to the difference of thickness of the sample against the depth of the depressions. This flow is almost the same as the extra space given by the wall inclinations, creating just a minimal outflow to the dies, which is necessary in order to avoid contact between dies or avoid very high energy situations.

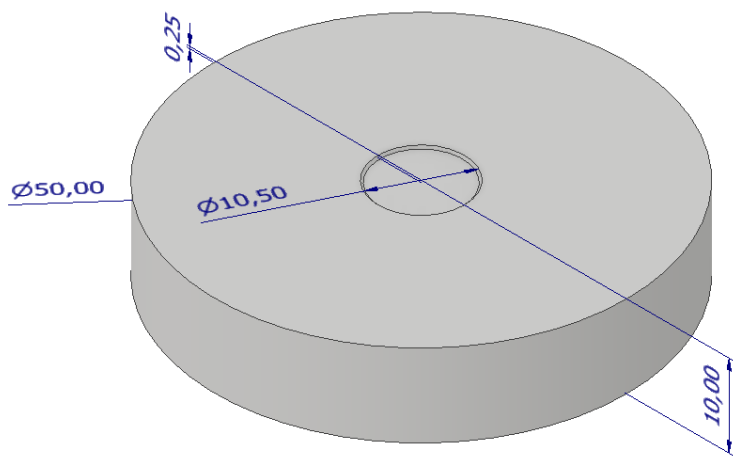


Figure 23. Upper and Lower anvil dies CAD model (Autodesk Inventor) with technical data.



#### 6.2.1.4. Boundary Conditions and Assumptions

In order to perform the simulation, boundary conditions and assumptions must be established and must be as similar as real laboratory conditions. The following assumptions have been considered:

- The temperature is established as room temperature and constant (20°C).
- No thermal activation, diffusion or thermal processes have been considered in the sample.
- There are no energetic losses of any kind (uniaxial and shear stress are applied to the sample)
- No diffusion is considered between the die, punch and sample.
- The elastic deformation of the punch and die are neglected. (Rigid condition)
- The boundary conditions on the sample, punch and die are established just as pure mechanical and time dependant (Time Domain Mechanical Deformation study).
- The Coulomb's Friction Coefficient between anvils and sample are set-up as:
  - 0.61 for Aluminium – Tool Steel
  - 0.58 for Cooper – Tool Steel

No boundary conditions were set up for the sample, letting it flow in each and every direction without any constraints (understanding that the punch and die are geometrical constraints by themselves).

The constitutive equations for flow stress assures that the material maintains a homogenous structure following an elastic-plastic deformation.

$$\bar{\sigma} = \bar{\sigma}(\bar{\epsilon}, \dot{\bar{\epsilon}}, T) \quad (\text{Eq. 6.1})$$

The given function on the given relation established at Eq. 6.1 has proven in other projects to be fully determinant and to show good results. The CAE software has some integrated curves relating the deformation, speed of deformation and temperature, and through interpolations of the constitutive equation it is able to compute the deformation.

On the other hand, for the punch and for the die the rigid boundary conditions, which establish that no elastic nor plastic deformation occurs, were defined. This proves to be an interesting choice thus no mesh must be established for the die or punch, which decreases considerably the amount of DOF (Degrees of Freedom) to solve. The assumption is not far from reality and can be accepted as good due to the relative size of the sample compared to the dies. Even though, a stress distribution and deformation study will be performed over the lower and upper anvil to prove this assumption mathematically, as well as physically if necessary.

In the real case, the friction window was just set-up in the conic base where the sample is positioned and leaving the rest of the anvils free of friction (slipping condition).

### 6.2.1.5. External Loads and Efforts

The external load must be defined to obtain the correct results. As it has been seen under different articles, the high pressure condition is difficult to achieve in DEFORM (Figueiredo, Cetlin, and Langdon 2011) but, even though good results are established for 1.0 and 2.0 GPa, the necessity of establishing a real torque motivates the necessity of obtaining 6.0 GPa (or even more) and more turns.

On a more real case and under further comparison with the semi-constrained type, real anvils and real conditions have been applied. Following the previous simulations, which generated good results, a load of 78.500 N has been applied, which is equivalent to 1.0 GPa.

### 6.2.1.6. Mesh and refinement

As already known, the border is an important area to be meshed. In this particular case and after different case simulations, the mesh was set-up in 2 different ways.

In the ideal case, the first mesh was set at the pressure operation, which was done with a normal automatic mesh. After this operation, the torsion operation was developed under a new generated mesh with a window mesh at the border. This has 2 main advantages, the first one is the increase of elements in the most problematic area and the second advantage is that the amount of elements increases instead of diminish.

Under the real case, the mesh window was set along a cylinder of 10 mm of diameter, in which the mesh size has an absolute value of 0.1 mm. This allows the mesh to be quite fine in the centre of the sample, while the outflow was established as a coarse mesh as it is not important.

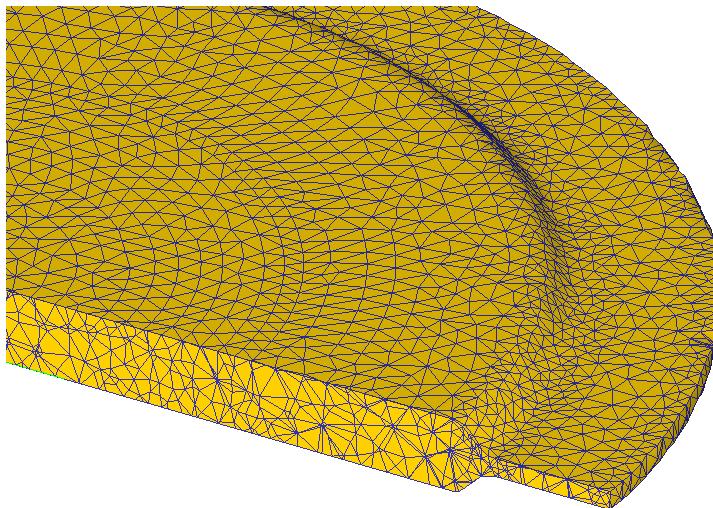


Figure 24. Mesh example at the beginning of the Torsion simulation. The mesh is finer at the borders of the depression with an empty cylindrical mesh window.

#### 6.2.1.7. Friction Coefficient discussion

One of the most problematic situations during the real and finite element experimentations is to assure that the anvils are applying enough strength to the sample in order to micro-fuse the surface contact between the sample and the die and assure that all the torsion is transmitted to the sample, assuring then the massive strain and therefore obtaining the enhanced material properties.

To do so, there are different ways to proceed or even to combine as one can quickly see under the Coulomb's friction model (Eq. 3.5). Following the equation, it can be seen that applying a high pressure the shear stress can be augmented, and so the amount of stress that is transmitted. It can be seen as well that increasing the friction coefficient the same results are obtained.

To increase the friction coefficient in experimentation, coating materials with high friction can be use or another solution might be very rough surfaces over the sample and the dies.

To compare results with a more theoretical (ideal) model, two sets of experiments have been set for the Copper sample; one following the Constant Shear Friction model and establishing the coefficient as 2.0, and another one following the Coulomb's Friction Mode established as 0.58. The results of both simulations will be useful to compare the divergence between an assured "sticking condition" between dies and sample, and another more realistic one which does not guarantee this "sticking condition".

## 6.2.2. Results for Copper sample (Ideal case with shear coefficient 2.0; 1 GPa; 1.5 Turns)

### 6.2.2.1. Stress Distribution

The stress distribution shows the expected pattern in this kind of simulation. As shown in Figure 25, the stress distribution is quite regular along the disk with a more compressed zone in the middle. It can be seen that along the 10 mm diameter sample, the mean stress is negative, this is due to the compressive pressure that the dies are applying. The zone outside the 10mm diameter is the material flow along the essay, which has no compression restriction, as it is flowing.

Stress is normally assumed as constant along the disk experiments following (Eq. 5.2), but the simulations show that the compressive state is larger (between 1.25 and 2.00 GPa) along the sample axis.

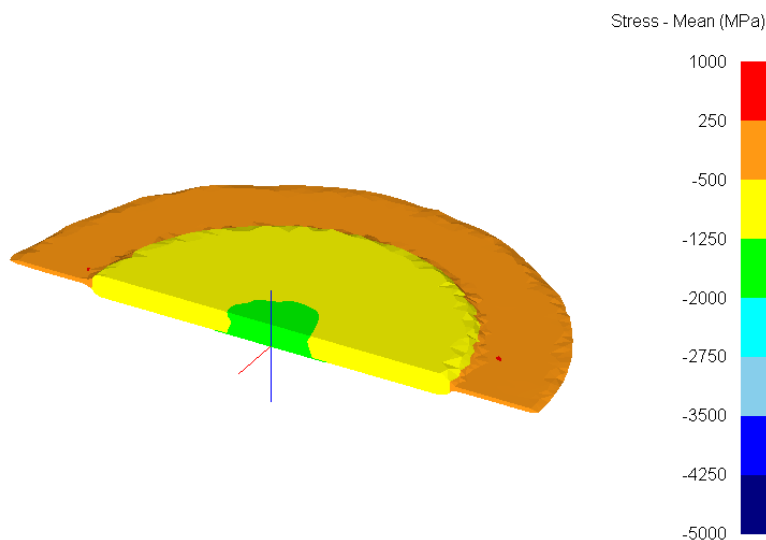


Figure 25. Stress distribution on a Copper sample during an HPT Semi-Constrained Type B experiment with a Shear Coefficient 2.0. 1 Turn at 1 RPM. 1 GPa.

### 6.2.2.2. Effective Strain distribution

As previous experiments, comparing with literature, the strain distribution has proven to be radial, with a larger strain at the edges of the sample, and the lowest at the very centre. Figure 26 shows that the strain distribution is homogenous, with no peaks or higher strain concentration along the sample, and the same strain distribution on both surfaces, the one keeping contact with the upper anvil, which is applying the load, and the lower anvil, which is applying the torsion.

Different simulations applying different pressures were realized having the same results and strain distribution pattern. This can be explained, if the ideal condition is contemplated, assuming that all the shear stress is applied to the sample and therefore producing a full torsion without slippage, so the strain distribution should be equal (following (Eq. 3.3)).

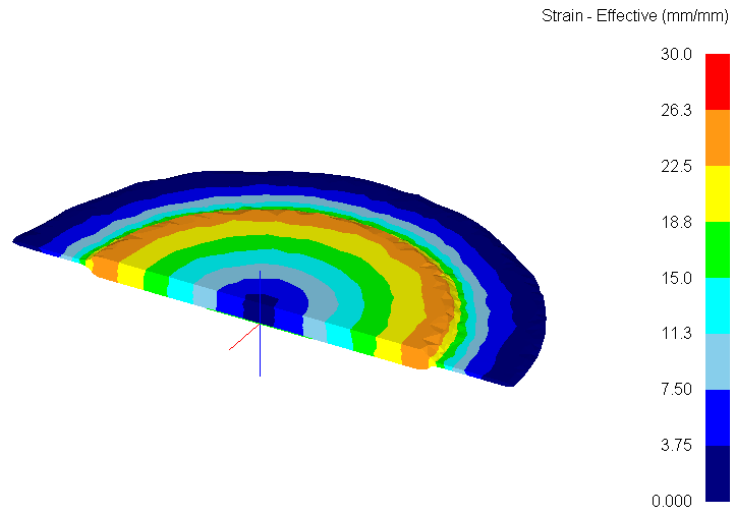


Figure 26. Strain distribution on a Copper sample during an HPT Semi-Constraint Type B experiment with a Shear Coefficient 2.0. 1 Turn at 1 RPM. 1 GPa.

### 6.2.2.3. Torque

Torque evolution is plotted as function of the angle in Figure 27. It can be seen that the Torque evolution is following a logarithmic like plot, with a huge increment of torque at the beginning of the sampling torsion, which makes sense, as the machine must overcome the energy to start with the sample deformation through shear stress.

After this, the torque evolution stabilizes, decreasing the torque increment slowly, as it seem to be eventually a saturation of torque.

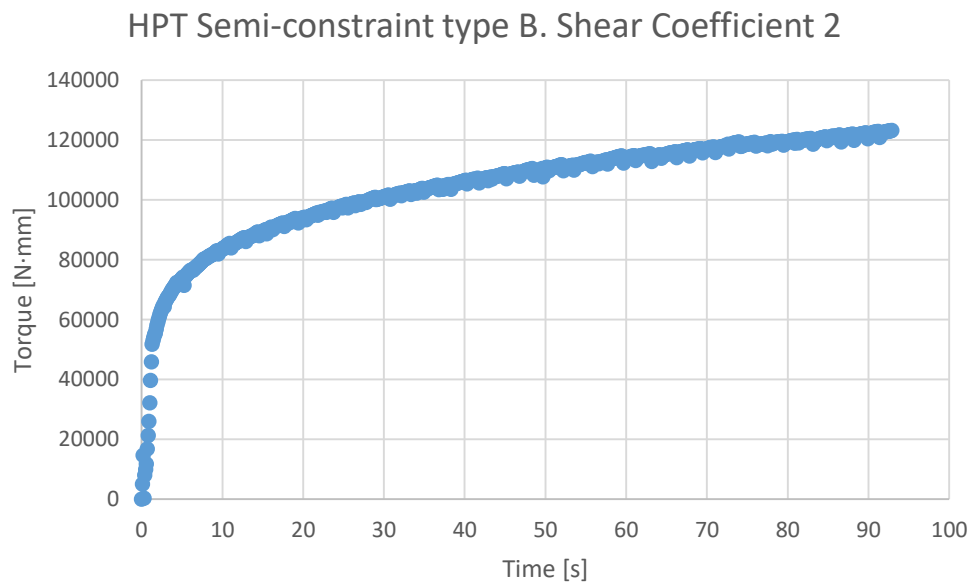


Figure 27. Torque evolution in function of time. Angular speed set at 1RPM.

### 6.2.3. Results for Copper sample

#### 6.2.3.1. Deformation

As it can be seen in the Figure 28, the total displacement inside the depression is very low (2mm), while the outflow is clearly suffering a huge displacement (values over 15mm). The scale is set on 2.0 mm, as it is better to see the deformation inside of the material. It can be seen that the outflow material comes from the centre of the sample. One can observe as well that the lowest displacement is set on the axis of the spin or the dies. That makes sense with theory, as it is known that this is the zone with less displacement during an angular rotation.

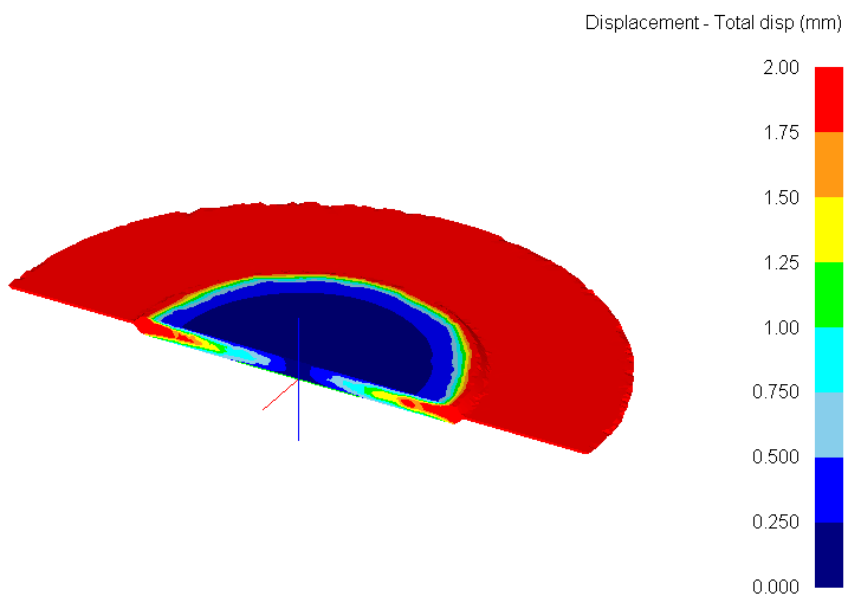


Figure 28. Total displacement (in mm) of the nodes and elements of the HPT semi-constrained type B copper sample simulation.

#### 6.2.3.2. Stress Distribution

Stress distribution plot was shown in the previous section for an ideal case (Figure 25). It was seen that the stress distribution was homogenous with an interesting characteristic: that the axial centre of the sample stress was qualitatively lower respect to the stress at the borders. Following the Coulomb friction model under a much more realistic simulation, it can be seen at Figure 29 that under these circumstances, no stress difference is seen in the borders compared to the centre. This is a more realistic representation of a real semi-constrained compression, in which the main objective is to get a uniform distributed stress state along the sample.

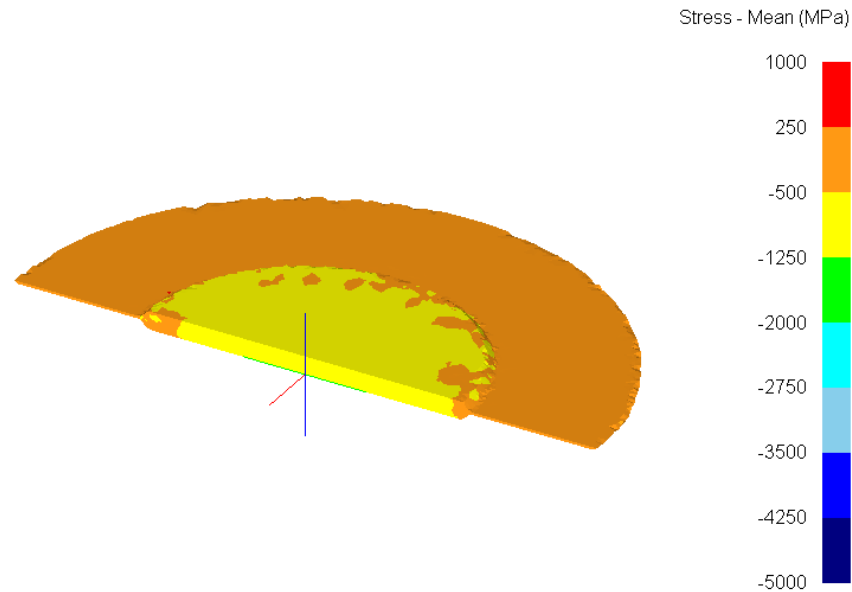


Figure 29. Stress distribution on a Copper sample during an HPT Semi-Constrained Type B experiment with a Frictional Coefficient 0.63. 1 Turn at 1 RPM. 1 GPa.

On the other hand, it is obvious that the material flow would have a positive stress near zero, as it has no boundaries (friction coefficient is set to 0 in this zone) and it is actually pushed out.

### 6.2.3.3. Strain distribution

The strain distribution follows the same pattern as the ideal case and as shown in literature, with an outflow between anvils and the depression zone having the most of the effective strain at the outer radius of the sample (depression walls). It can be seen that after 1 turn at 1 rpm and under 1 GPa, the strain is roughly 30 mm/mm. It is shown as well that from the centre until the approximately 5 mm radius, the strain increments directly proportional to the radius, while from the outer radius till the maximum distance of the outflow, the effective strain diminishes. This can be accepted assuming that the material outflow is not subjected to any kind of torsion, as the friction coefficient set outside the depression anvils is 0, which means that there are no interferences, neither friction between anvil and sample, so the material outflow just flows and spins with no loads.

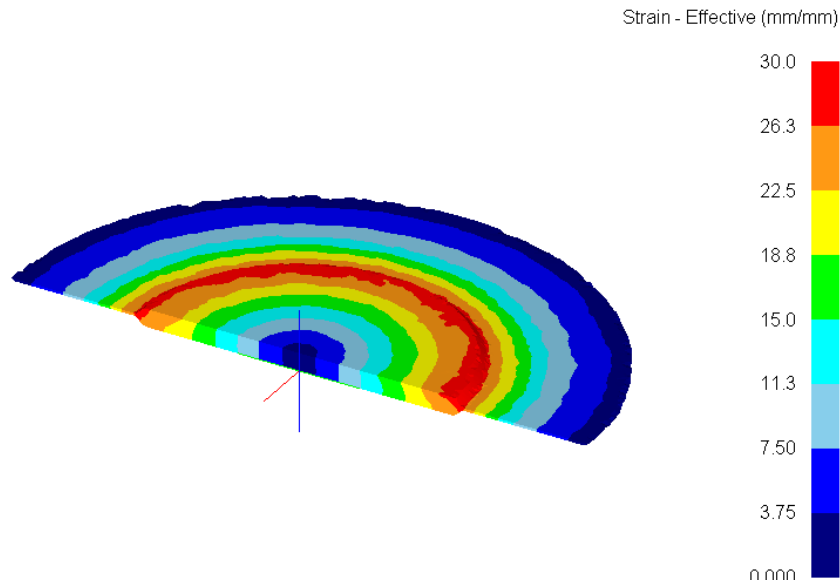


Figure 30. Strain distribution on a Copper sample during an HPT Semi-Constrained Type B experiment with a Frictional Coefficient 0.63. 1 Turn at 1 RPM. 1 GPa.

#### 6.2.3.4. Torque

The torque along the HPT process is actually very interesting, as it has a very similar distribution as the ideal cases that was shown before. It can be seen that for the same number of turns (1 turn at 60 seconds), the amount of torque necessary under the real case is slightly higher than the one necessary for the ideal case.

It is interesting as well to confirm and see that the torque evolution stabilizes in a saturation like evolution along higher turns, as expected.

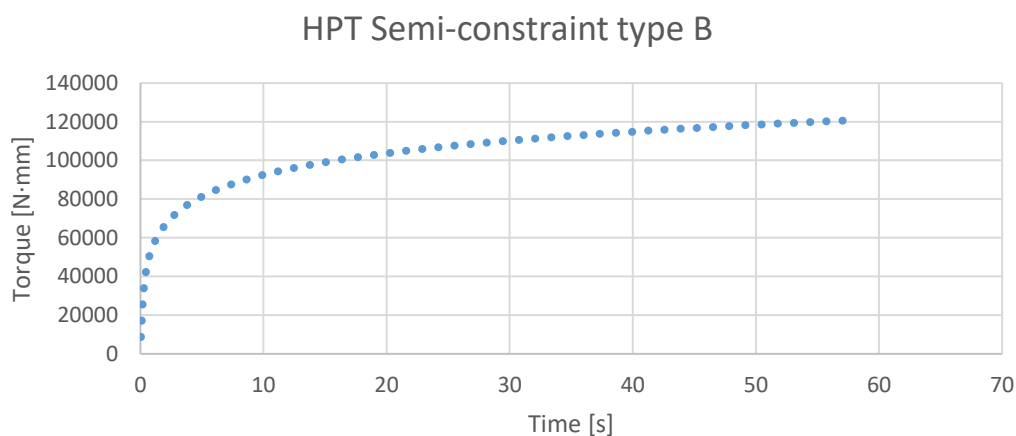


Figure 31. Torque evolution as a function of time along 1 turn.

The saturation value after 1 spin is around 120.00 N·mm, which is an acceptable value for a screw machine or a pressure and torsion machine.



## 6.2.4. Results for Aluminium sample

### 6.2.4.1. Mesh evolution

Following the previous simulations, the actual mesh configuration was the same applied as the other cases, as it has proven to be one of the most practical and efficient. Figure 32 shows the mesh around the sample, where it can be seen that after several re-meshing processes, the meshing window applied at the 2 mm around the 5 mm centre radius of the sample is finer than the rest of the mesh.

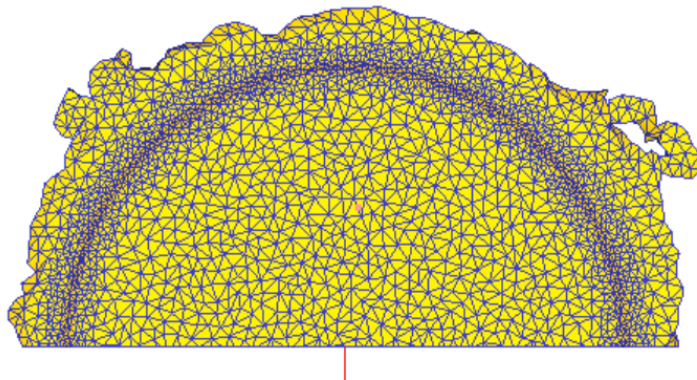


Figure 32. Mesh configuration for the last step of the simulation.

### 6.2.4.2. Deformation

The displacement values are presented in Figure 33 and they show that the lower part of the sample is subjected to higher displacement than the upper one. This is due to the fact that the lower anvil is the one which spins along the axis and therefore is where the material suffers most of the displacement.

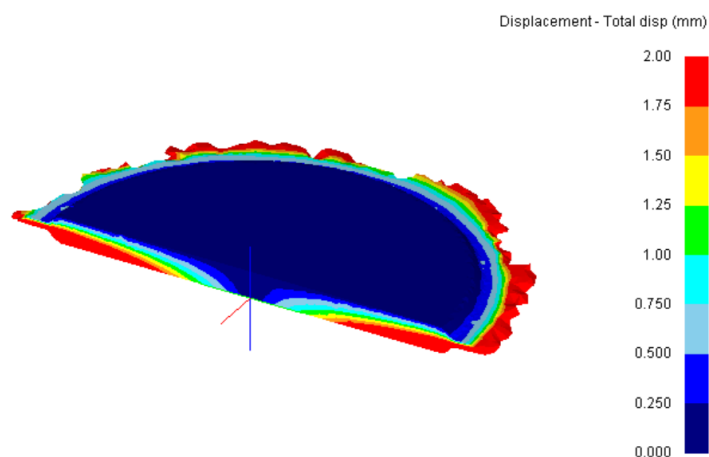


Figure 33. Total nodal displacement of the aluminium semi-constraint sample at 1 turn.

It can be seen as well that the outflow has high levels of displacement, reaching values of 12mm not possible to illustrate with this scale.

### 6.2.4.3. Stress Distribution

The stress distribution presented in Figure 34 shows that most of the sample is under a 1 and 0.5 GPa compression, which is the established pressure by the simulation solicitations. As it can be seen, at the end of the process, the stress is clearly not uniformly distributed, being the maximum at the centre and decreasing along the radius until reaching positive values due to the outflow. The values obtained were expected and normal, as previous simulations and in good accordance with literature.

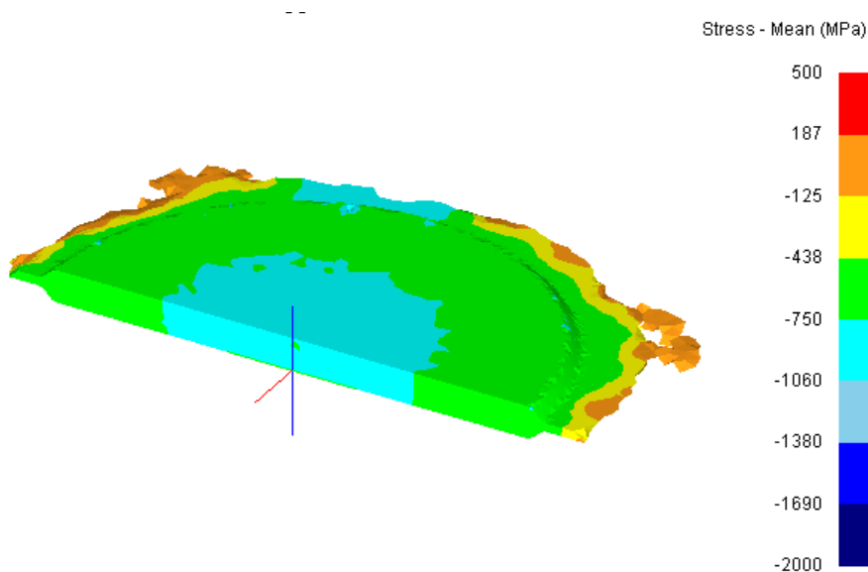


Figure 34. Mean stress after 1 turn of the sample.

### 6.2.4.4. Strain distribution

The strain distribution is uniform and with a maximum value of 30 mm/mm as the copper sample (Figure 30). It can be seen as well that there are huge discrepancies with the outflow that is due to the configuration of the friction between dies and anvils outside the depression. Copper sample was set up with a coefficient of friction zero outside the depression, so the material outflow was not subjected to any stress, while the current simulations are being subjected to the same coefficient factor that it is found in the depression. The main aim is to compare the two different simulations and to show the differences between them.

It is remarkable that the use of a higher friction coefficient between anvils and sample outside of the depression shows a larger area with a higher value of accumulated effective strain, which can be interesting for different applications.

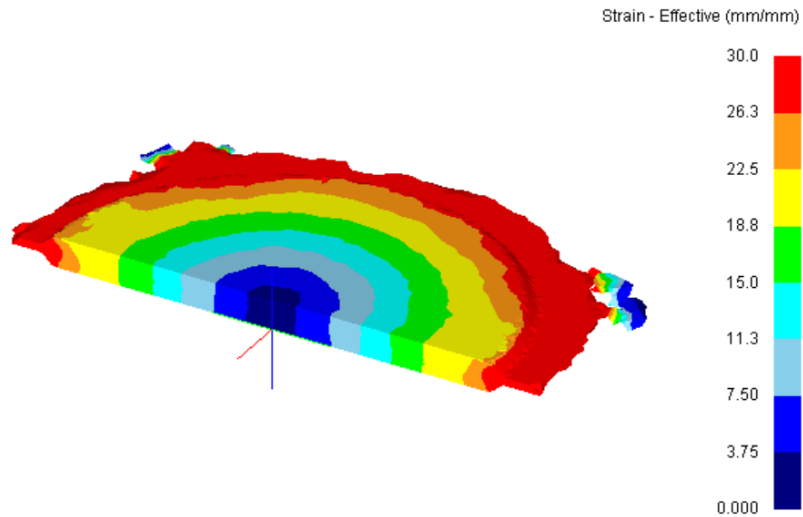


Figure 35. Effective Strain after 1 turn in the Aluminium 1100 sample.

#### 6.2.4.5. Torque

Torque evolution (Figure 36) shows a relevant data, that along the first turn the torque saturates in a constant value of very low slope increasing linear function, as reported in the literature (Figueiredo, Cetlin, and Langdon 2011).

This is interesting, as it shows that once the torsion begins, it needs a huge increment of torque to initiate the torsion strain, but for Aluminium 1100 in less than 1/6 of a turn this force is overcome and the torque is constant.

It is interesting as well, because the value is quite low (50.000 N·mm) compared to such as, for example, Copper. This is strongly related to the stiffness of the materials.

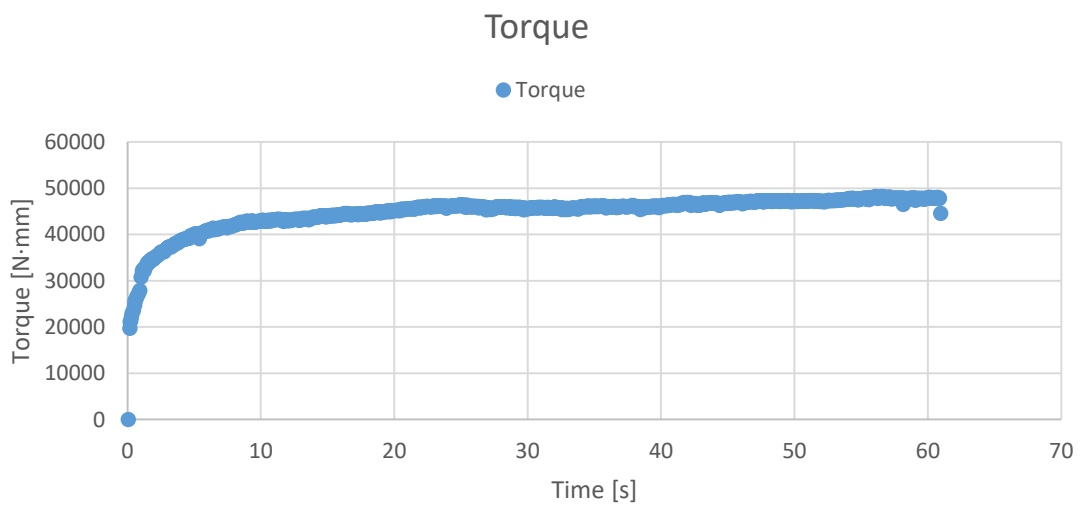


Figure 36. Torque time dependence for the Aluminium 1100 sample under the semi-constrained type B HPT process for 1 turn.

## 6.3. HPT Case 2: Unconstrained

The unconstrained case is one of the most challenging in terms of Finite Element Method simulation. Due to the amount of deformation that the sample experiences and the freedom of deformation due to the unconstrained state, the discretised body's nodes suffer a huge displacement evolution not only under torsion, but under compression as well, which motivates a constant re-mesh and a huge amount of calculations. This is not a comparable behaviour as for a semi-constrained or constrained case, where the impossibility of the body nodes to flow (mostly) simplifies the calculation part of the FEM simulations.

Two different simulation cases have been performed under unconstrained condition, the first one is a compression between 2 infinite anvils in which it can be considered an ideal simulation, and on the other hand, the second simulation is performed under two truncated conic anvils which have a 10mm diameter application base, as based in different researches.

### 6.3.1. Case Study

Multiple case studies have been elaborated following the parameter inputs of Table 5 with which different results have been obtained.

The next subsection will reflect those parameter definition and justification, along its results and effects, leading to a better understanding of the process and, finally, its optimization.

#### 6.3.1.1. Geometrical Model

As geometrical model, the bottom die and punch are contemplated, in which the sample will be the same as specified in the previous case study, so there will be no changes on this element.

The bottom die and punch have two different configurations, one as an ideal case with infinite anvils and another one following a real case. As the ideal case has no implications, no restrictions were imposed in their conception. On the other hand, as no restrictions are imposed under the real case, different assumptions were established for their development, which are:

- The models must enter dimensionally in the current hydraulic press in the laboratory.
- The models must withstand the maximum load that the hydraulic press can deliver.
- The models must portray their duty within a safe coefficient.
- The models sample base must fit exactly with the sample diameter (i.e. 10 mm)

Different models have been developed following the previous solicitations and which produced different results in terms of stress distributions, volume and other mechanical properties.

#### 6.3.1.1.1 Upper and Lower Anvils: Ideal Case

The Upper and Lower Anvils in an Ideal Case have been represented by two “infinite” dies respect the sample. The term infinite defines the impossibility of the sample to outflow outside of the dies, to do so, different sizes have been tested, and the Figure 37 model has been selected due to its identical performance as much bigger diameter anvils. Different simulations have proven that neither the size nor the geometry affect the sample evolution under compression or torsion as the anvils are assumed as rigid.

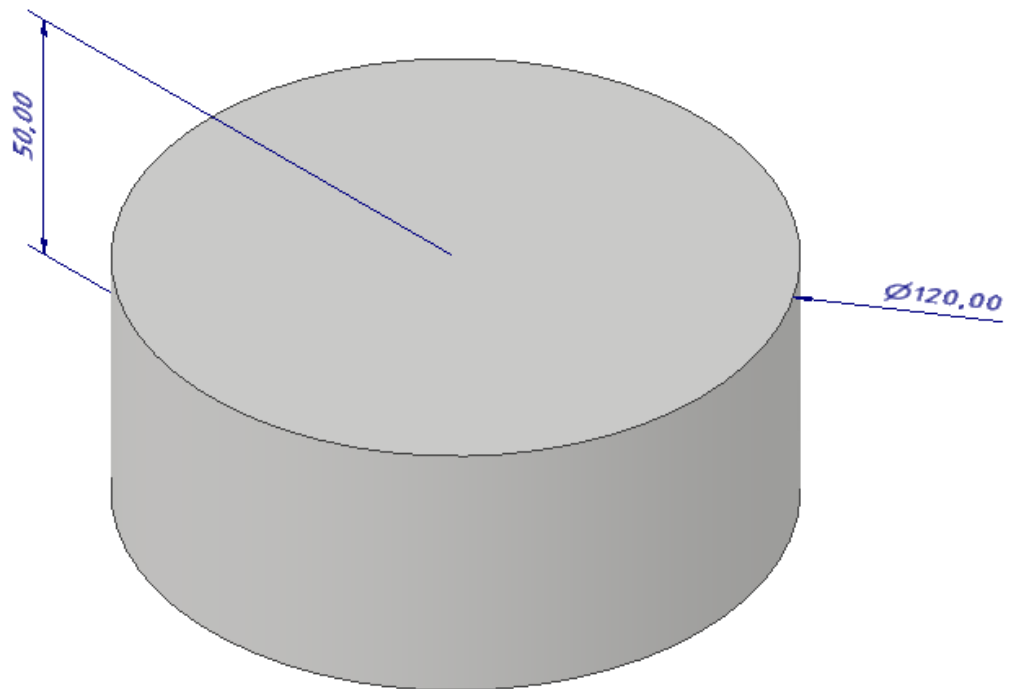


Figure 37. Upper and Lower anvil dies CAD model (Autodesk Inventor) with technical data.

#### 6.3.1.1.2 Upper and Lower Anvils: Real Case

Following the ideal case, a more realistic case has been performed, using this time the upper and lower anvil as the one shown in Figure 38. As it can be seen, the dies are a truncated cone, which small sliced base diameter is the same as the sample and the conic base is variable, in this case set as 120 mm diameter and a height of 49.5 mm. The reason of this particular height and diameter is due to the hydraulic press configuration, in which this die size are enough to place the sample correctly and have a good stability of the die.

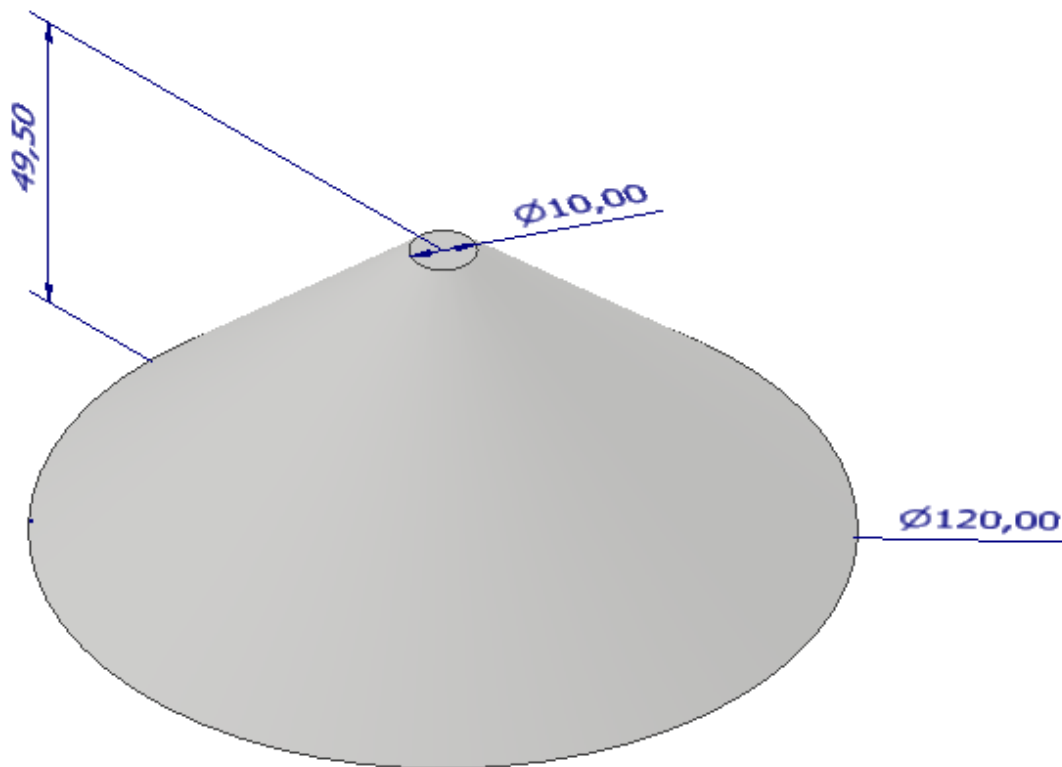


Figure 38. Upper and Lower anvil dies CAD model (Autodesk Inventor) with technical data.

### 6.3.1.2. Boundary Conditions and Assumptions

In order to perform the simulation, boundary conditions and assumptions must be established and must be as similar as real laboratory conditions. The following assumptions have been considered:

- The temperature is established as room temperature and constant (20°C).
- No thermal activation, diffusion or thermal processes have been considered.
- There are no energetic losses of any kind (the tensile and shear stress is applied to the sample)
- No diffusion is considered between the die, punch and sample.
- The elastic deformation of the punch and die are neglected.
- The boundary conditions on the sample, punch and die are established just as pure mechanical (Time Dependant Mechanical Deformation study).
- There will be no interference between dies.
- The dies will be establish as rigid bodies.
- The Coulomb's Friction Coefficient between anvils and sample are set-up as:
  - 0.61 for Aluminium – Tool Steel
  - 0.58 for Cooper – Tool Steel

No boundary conditions were set up for the sample, letting it flow in each and every direction without any constraints (understanding that the punch and die are geometrical constrained by themselves on the vertical direction).

The constitutive equations for flow stress will be again the same as the previous case (Eq. 6.1).

### **6.3.1.3. External Loads and Efforts**

To proceed with a scientific experimentation or, in this case, a Finite Element Method, an external load must be defined to obtain correct results. The purpose of this experiment is to obtain significant data over a HPT process and, to do so, as illustrated in Figure 1, two stages are required: pressure and torsion. The application of pressure provides a high effective strain, which is primordial for the ultra-fine grain generation, but it does not apply as much as necessary. Here is where the shear stress applied through the torsion provides the necessary strain to generate a bulk nanostructured material.

In order this shear stress to be effective, the pressure applications are of the utmost importance. In order to be able to transmit the efforts from the punch and die to the work piece it must be assured that it exists a micro-bonding between the punch, work piece and die, so the work piece it is not only going to spin along the punch, but to shear its metal crystallographic planes. The parameters that assure this condition are the application of a compressive stress, and the existence of a frictional coefficient between the dies and the work piece. The frictional coefficient is obtained from handbook (EngineeringToolBox 2017), while the load to be applied is not completely determined. Following experimental literature, the pressure values of 1.25, 2.5 and 6.0 GPa are presented as the most general ones to proceed with HPT.

Finally, and with the aim of producing this stress, different methods were contemplated. The selected method has been the application of a continuous hydraulic press speed with a force limitation of 471.000 N, which equals to 6.00 GPa due to the punch surface for the ideal simulation, while the force limitation for the real simulation is set as 78.500 N which is equivalent to 1 GPa. This method has been selected by its similitude with the present hydraulic press in the laboratory, which is operated with a continuous speed application.

The application of the torsion has been specified with an initial number of revolutions (i.e. 1,2,4) as presented in literature. As one of the initial aims of this experiment is to characterize the necessary torque to produce an ultra-fine grain material, the analysis of stress distribution at different turns presents itself as an illustrative tool, while the Torque in function of time will illustrate the mechanical requirements to achieve the necessary microstructure.

#### 6.3.1.4. Mesh and refinement

As reflected in the section Meshing and Re-meshing, the configuration that has been proven to be the most effective is an empty cylinder meshing window with a higher number of elements at the exterior of the sample once compressed. That is due to the fact that the elements are more distorted at the outside radius of the sample due to the angular speed being function of the distance of the applied axis.

The configuration has been proven to be effective and to provide with good results.

On the other hand, for the ideal case, a similar configuration has been defined as an empty cylinder meshing window, but in this case with a difference within the inner and outer radius of 3mm, being set at the application of the die (see Figure 38). This has proven to be effective, especially if the inner sample elements are small, the mesh window has the fine elements and the outside radius zone has the biggest elements. The reason for the border and inside elements is exactly the same as the previous paragraph, as for the exterior part the big elements are defined due to the lack of interest of the outflow of material.



### 6.3.2. Results for Aluminium sample (Ideal Case; High Pressure; 0.5 Turn; 0.61 coefficient)

#### 6.3.2.1. Mesh evolution

Along Figure 39, Figure 40 and Figure 41 display the evolution of the set up mesh. It is shown the initial mesh in Figure 39, where it can be seen the outer radius mesh is quite more precise and fine than the interior one as it has been discussed in the previous section. The amount of initial elements is set at ~120.000 elements.

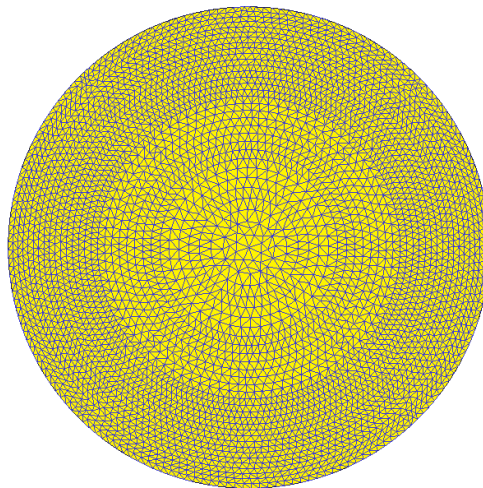


Figure 39. Initial mesh configuration with approximately 120.000 elements with a finer element size at the outside compare to the inside

Following the compression from the upper anvil, there is a significant element loss due to the resize of the sample (diameter increment of ~180%). This can be explained due to the difficulties that the current FEM software has to re-mesh inside the material when the height is very small, as the element size is not fine enough in terms of time and computer render. It has been proven, however, that the amount of elements is enough to show the similarities with theoretical equations.

It can be seen as well that the amount of elements at the inside and outside is roughly the same size and follows the same distribution. That is because, as shown in Meshing and Re-meshing sections, under a compression test the effect of the mesh configuration, if fine enough, does not distort the results.

After the compression, the geometry was then re-mesh manually to obtain the same elements as initially.

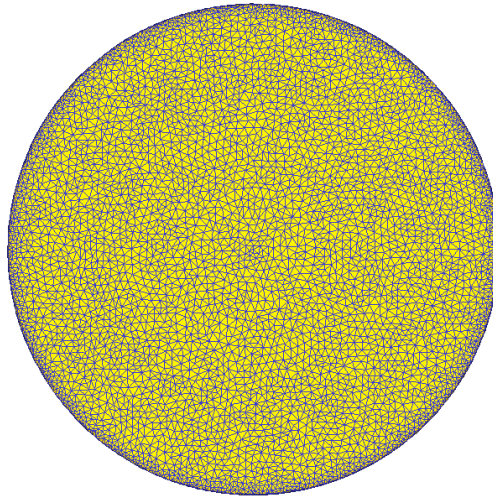


Figure 40. Mesh distribution with approximately 55.000 elements with a constant element size distribution after compression.  
 $h = 0.3214 \text{ mm}$ ;  $d = 17.7157 \text{ mm}$

Following the torsion process after loading at 1 GPa and activating the re-mesh process, after 30 seconds the resulting mesh obtained is shown in Figure 41.

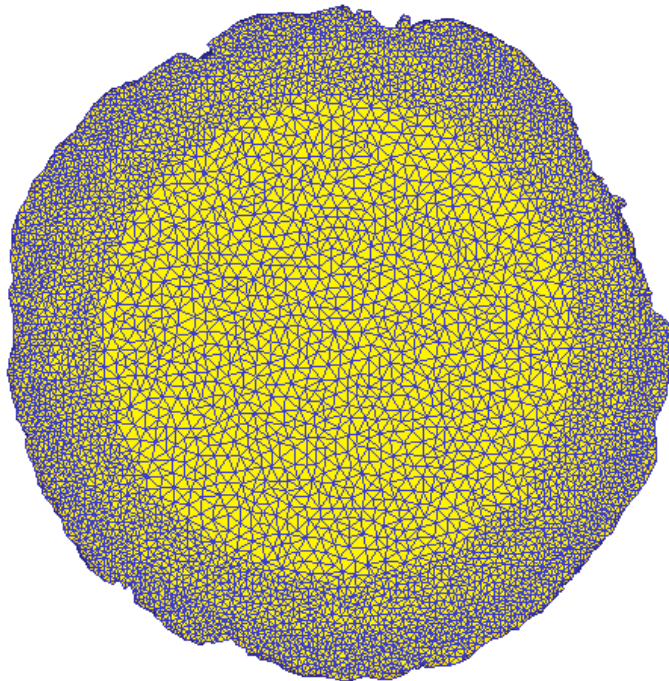


Figure 41. Mesh distribution with approximately 50.000 elements with a finer element size distribution at the outside compare to the inside.

It can be seen that the radius elements is finer that the inside one. It can be seen as well that under high loads, the border starts to distort probably as a result of little mesh discrepancies at the border of the sample.

### 6.3.2.2. Deformation

In terms of deformation, Figure 42 and Figure 43 show the total displacement of the sample after compression and after half turn torsion. Under the pressure of a cylindrical anvil over the sample surface, the material can just flow from the peripheral surface to the exterior, which shows the maximum amount of displacement.

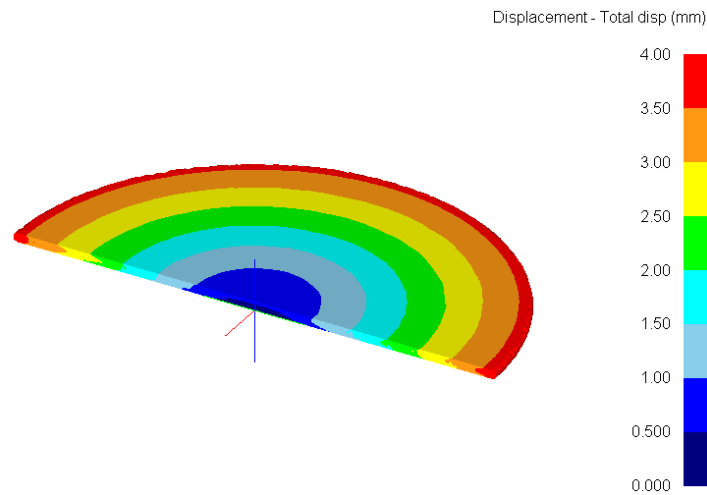


Figure 42. Total element displacement after compression.

In terms of torsion, the displacement is maximum as well at the outer radius.

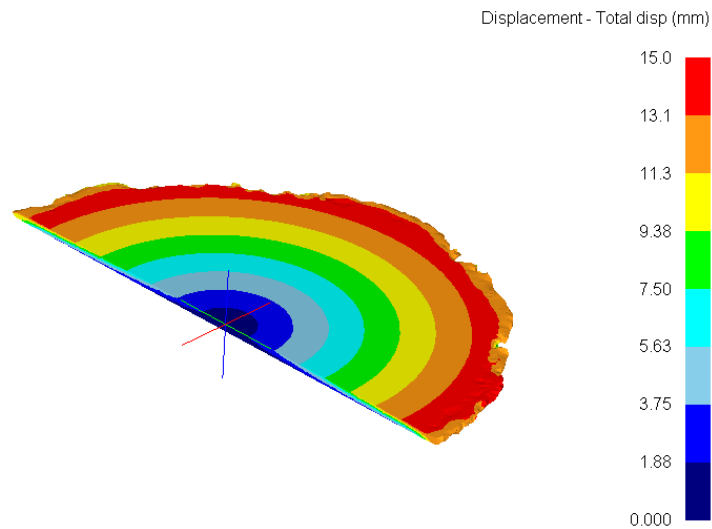


Figure 43. Total element displacement after the torsion rate. Rear part of the sample.

It is interesting to check that there are huge differences in displacement terms between the upper and lower part of the sample in both figures. In Figure 42, it can be slightly appreciated that the displacement is larger in the upper part compared to the lower part that is due to the fact that the upper anvil is compressing, while the material rests lay on the bottom die. On the other hand, Figure

43 shows a great difference between upper and lower part due to the fact that only one of the anvils is spinning (the one with the great displacement) and the other just holds on its position. As there is no movement and in this ideal case the sticking condition with a coefficient friction on 0.67 is set up, to nodes barely move and, therefore, there is no displacement.

### 6.3.2.3. Strain Distribution

The strain distribution under the high pressure step and then the torsion are shown in Figure 44 and Figure 45 respectively. The strain distribution is somehow homogenous along the radius, even though the simulations does not show a homogenous distribution within these areas. This could be, as illustrated in section CAE SOFTWARE, due to the coefficient friction, which has been selected as 0.61 coefficient following the Coulomb's friction model.

The issue is not of the utmost importance, as the strain accumulated is really small compared to those obtained under the torsion step, as shown in Figure 45.

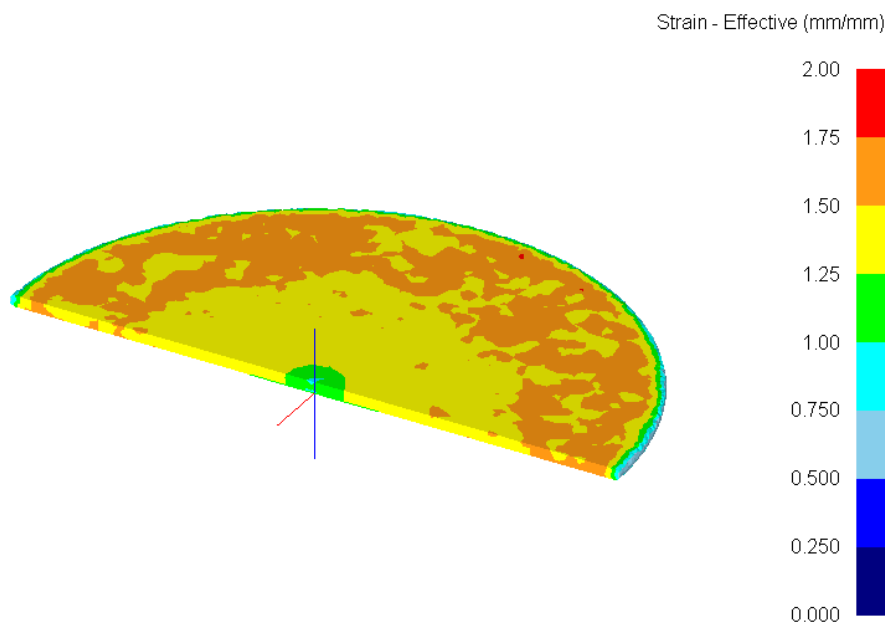


Figure 44. Effective Strain distribution of the sample.

The strain distribution along the torsion process is homogenous and reaches up to 55 mm/mm values, which are in good accordance with the theoretical equations (see Figure 46). The distribution itself is representative of the expected results along literature and validated theoretical models. The plastic deformation at the centre of the sample is zero as there is no deformation along the rotation axis, and the further from the axis in a radial way, the more strain is obtained.

There is only a small discrepancy along the simulation, and that is the border of the sample, which is not constant and, therefore, the obtained values are quite erratic.

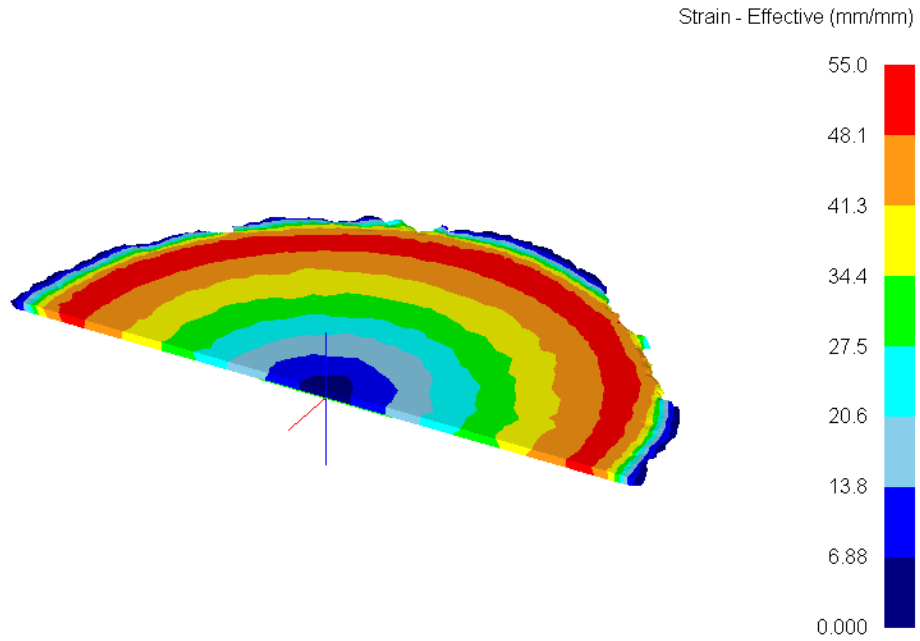


Figure 45. Effective strain distribution of the sample at half turn.

On the other hand, the validation of the strain evolution between the model described in equation (Eq. 3.3) and the obtained by the simulation are shown in Figure 46 and it can be seen that the two models follow exactly the same evolution, which corroborates the fact that the simulation results are correct. This motivates that all the assumptions and solicitations therefore established for the present simulation can be extrapolated to more realistic simulations with the real anvil to use in laboratory.

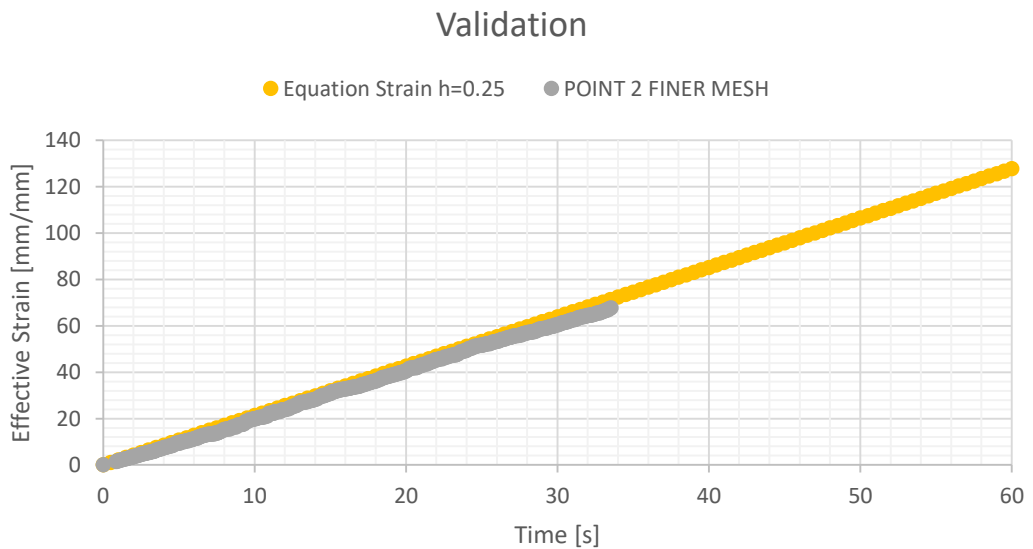


Figure 46. Plot of the Theoretical Model Equation (yellow) against the simulation data obtained (grey) evaluated at the same geometrical point. It shows the evolution of Effective Strain in function of time.

### 6.3.2.4. Stress Distribution

The stress distribution (Figure 47) shows a compression effect along the whole sample except at the outer radius. This is the expected results, as the work piece is under the load of the upper anvil. It can be seen that the centre pressure reaches more than 5 GPa of compression, while at the exterior there is a traction pressure of 0 - 0.2 GPa.

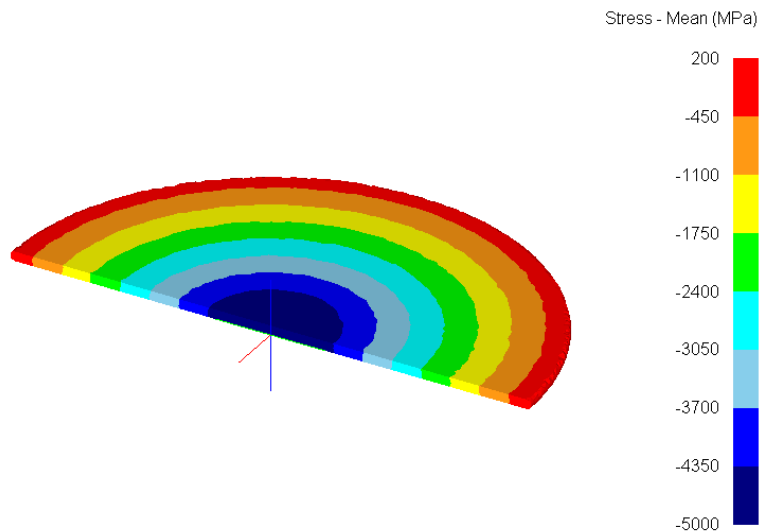


Figure 47. Mean stress distribution of the sample after compression.

As the compression load is not changing during the torsion (Figure 48), no significant changes are observed along the process, it can be seen though a dispersion of the stress loads along the radius, with a slight increment of the pressure loads compared to the just compression step. This can be explained by the fact that the material is flowing.

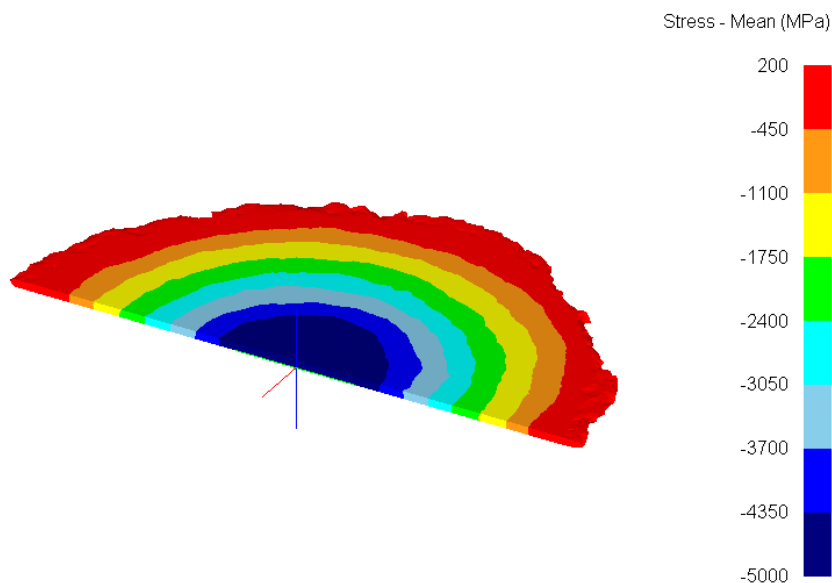


Figure 48. Mean stress distribution of the sample after half turn torsion.

### 6.3.2.5. Torque evolution

As it can be seen in Figure 49, the torque evolution under 6 GPa shows an already saturated curve. The torque evolution shows a huge slope at the beginning, probably due to the initiation of the deformation and the necessity of a huge shear stress, after this slope, the evolution remains constant along time which shows an already saturated curve for the given conditions.

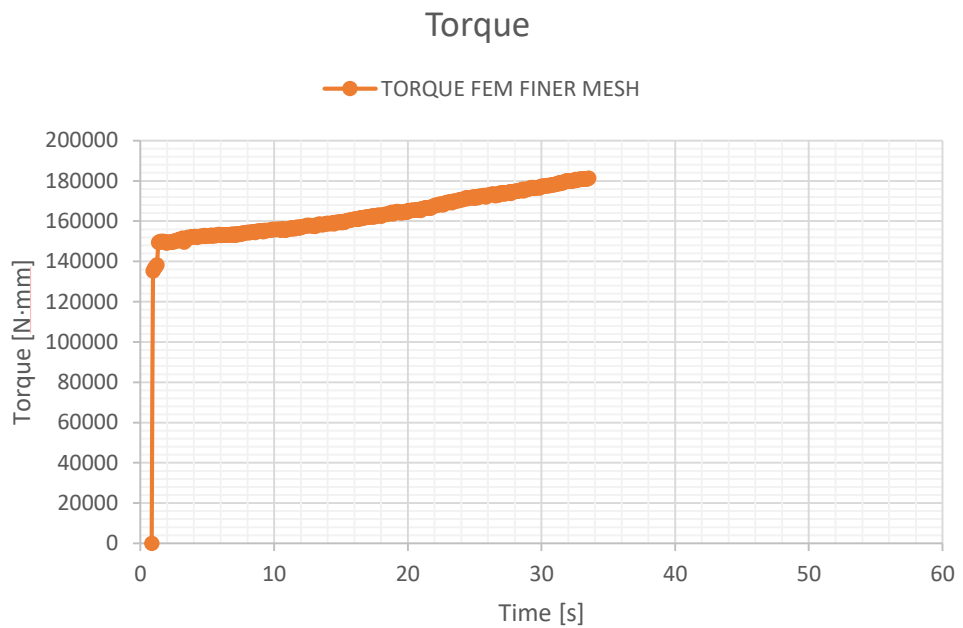


Figure 49. Torque as a function of time



### 6.3.3. Results for Copper sample (Ideal Case; High Pressure; 0.5 Turn; 0.58 coefficient)

#### 6.3.3.1. Mesh evolution

Following the mesh description set-up as established for the aluminium sample, the same mesh distribution and the same amount of element size was performed for the copper case. That's due to the fact that as the discretisation of the medium is based on the same geometry, the same elements are obtained.

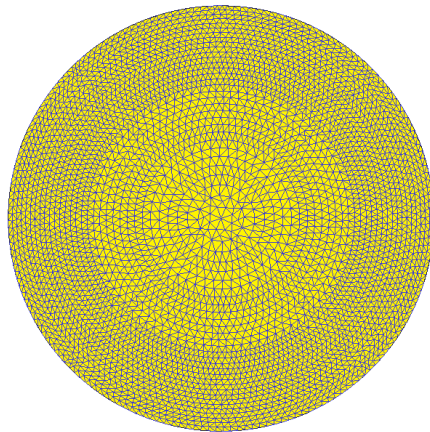


*Figure 50. Initial mesh configuration with approximately 120.000 elements with a finer element size at the outside compare to the inside*

After compression, the new mesh is set up as established before with a finer outer ring as it can be seen in the Figure 51. In this simulation, the outer ring of the re-meshing window was set as infinite, which means that all the sample new material expanding will have very fine elements, which creates a material with a higher and higher amount of elements per re-mesh. As shown in Figure 52, the sample goes from 110.000 elements to 185.000 elements.

This increment of elements has more accuracy and no loss of information as a clear advantage, on the other hand, the amount of elements and the fact that it increases per each and every re-mesh shows an increment of simulation time, power and memory consumption, which leads to very demanding simulations. For example, the time consumption was around 60 non-stop hours for the present simulation.

It was decided to set-up the simulation with these parameters to obtain data with a finer mesh and compare to the previous simulation in order to check if more precise results are obtained, which will be discussed later.



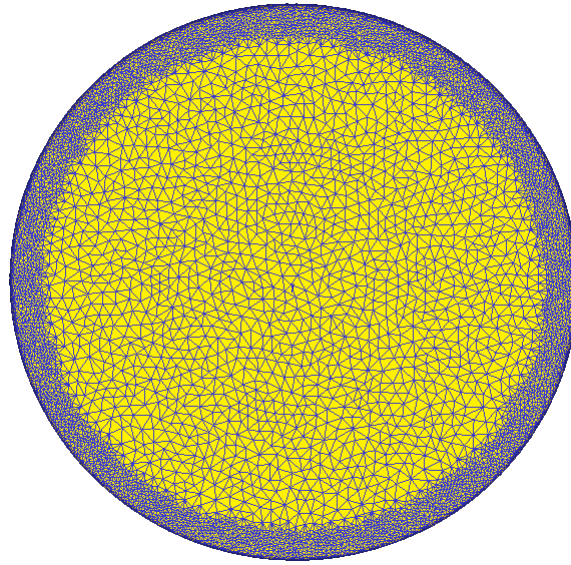


Figure 51. Mesh distribution with approximately 110.000 elements with a finer element size at the outside compare to the inside. Manual re-meshing performed.

Figure 52 shows at the end of the simulation a quite regular mesh at the border, compared to the irregular one shown in the Figure 41, which leads to a smoother border and therefore, more homogenous results in the perimeter.

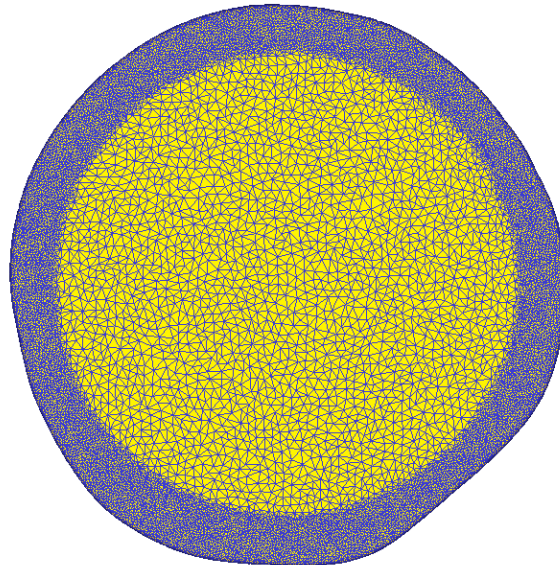


Figure 52. Mesh distribution with approximately 190.000 elements with a finer element size at the outside compare to the inside after half a turn torsion. Automatic re-mesh performed by DEFORM v10 due to Mesh Windows set-up.

### 6.3.3.2. Deformation

The displacement of the nodes (Figure 53, Figure 54) shows the same evolution as the Aluminium sample, which is completely normal and expected. What is remarkable is the quantitative displacement of the nodes. After compressing, the amount of displacement in the copper sample is lower than in the aluminium one (Figure 42). This is due to the ability of the materials to withstand deformation changes under different loads, in this case, compressive loads. As Young moduli of each of the materials reflect, copper is stiffer than aluminium, and therefore, less deformation under the same load is shown.

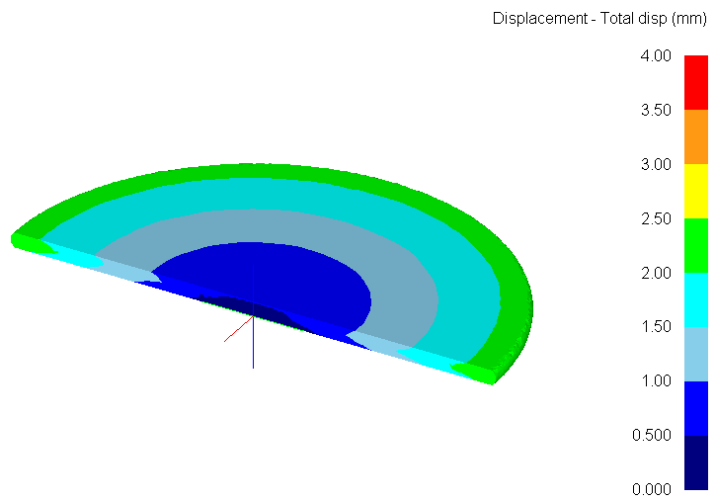


Figure 53. Total element displacement after compression.

Under torsion, material displacement reaches around 13mm displacement as a maximum at the border of the sample. Again, it is interesting to observe the difference between the upper and lower faces of the sample, in which one the displacement is almost zero and the other sustains all the nodal/elemental displacement of material.

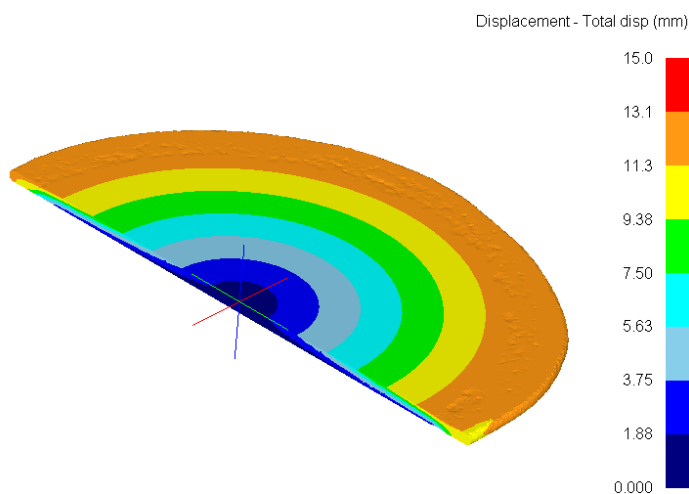


Figure 54. Total element displacement after compression after half turn torsion. Rear part of the sample.

### 6.3.3.3. Strain Distribution

The strain distribution proves to be homogenous again, showing a lower value at the centre and a higher value at the border. It can be seen (Figure 55) that strain values are lower compared to the aluminium ones for the same reason as explained in the previous section.

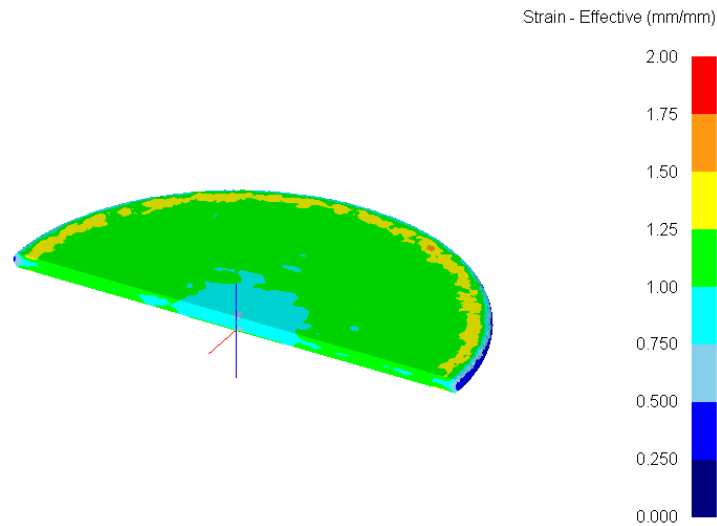


Figure 55. Effective Strain distribution of the sample after compression.

Figure 56 shows the strain distribution after the half turn torsion is applied over the work piece. First of all, it is interesting to see that the strain distribution is not exactly the same around all the work piece (the strain distribution is not completely symmetric), there is a localized zone around 5mm distance from the centre that shows a higher amount of strain (48-55 mm/mm) whereas at the same distance, there is at the same distance another localized area where most of the strain is set at 34.4-41.3 mm/mm (yellow range) whereas this particular region shows a 27.5-34.4 mm/mm strain values.

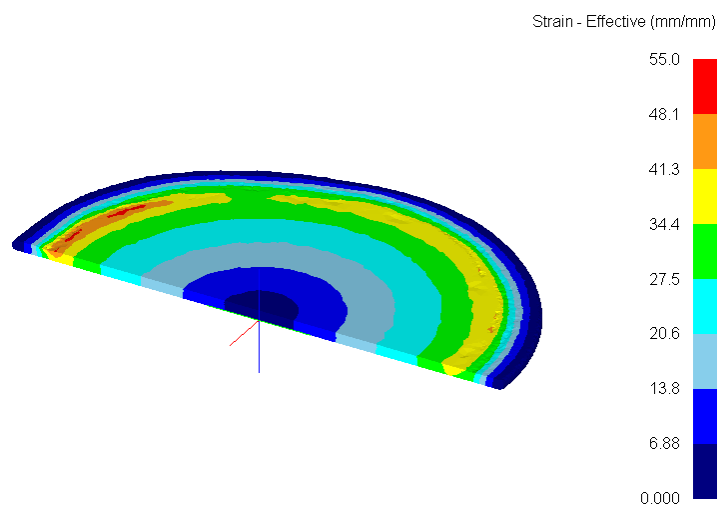


Figure 56. Effective Strain distribution of the sample after half turn Torsion of the sample.

Another particularity is the decreasing value of strain after the already mentioned 5 mm zone, where a decreasing strain area is shown. This is an interesting difference between the aluminium and copper sample that would be interesting to study under laboratory conditions and compare.

On the other hand, plotting the strain evolution at 5 mm along the HPT process time against the equation model, it can be found as well that the simulation results are in good accordance to the equation model as the Aluminium simulation was. It can be seen though a little discrepancy at 0.45 turn, where there is a 4.48 % difference between the theoretical and simulation model which is below 5%.

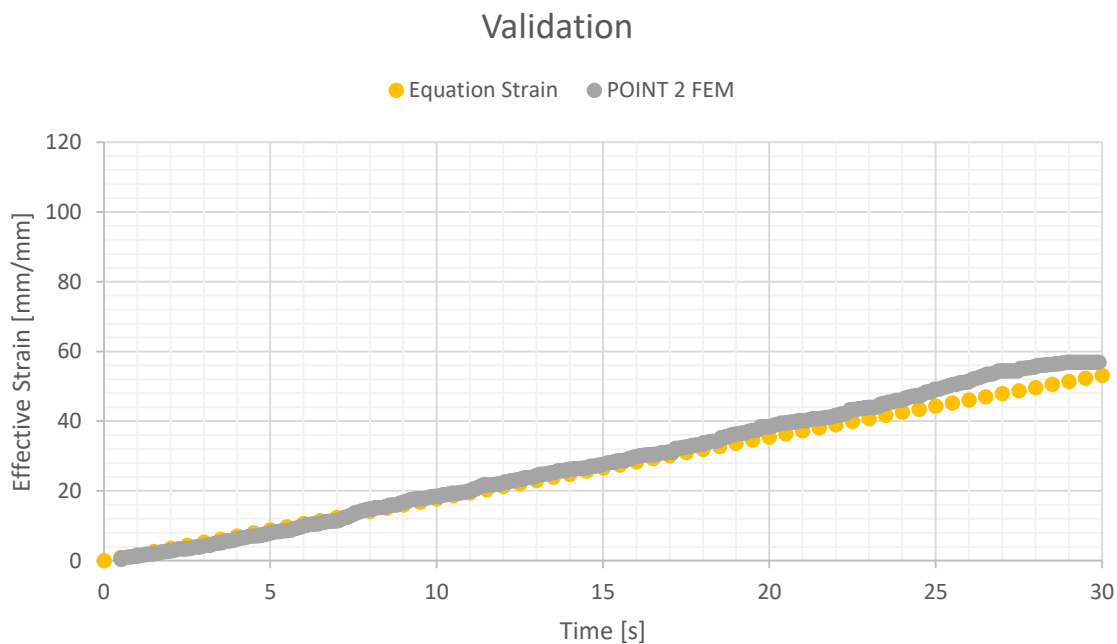


Figure 57. Plot of the Theoretical Model Equation (yellow) against the simulation data obtained (grey) evaluated at the same geometrical point. It shows the evolution of Effective Strain in function of time.

#### 6.3.3.4. Stress Distribution

Stress distribution (Figure 58, Figure 59) shows a higher area of compression than previous simulation (Figure 47). On the other hand, the stress distribution follows exactly the same evolution and the values are at the same range. This can be explained by recalling equation (Eq. 5.2), which shows that the stress is function of the load and the area.

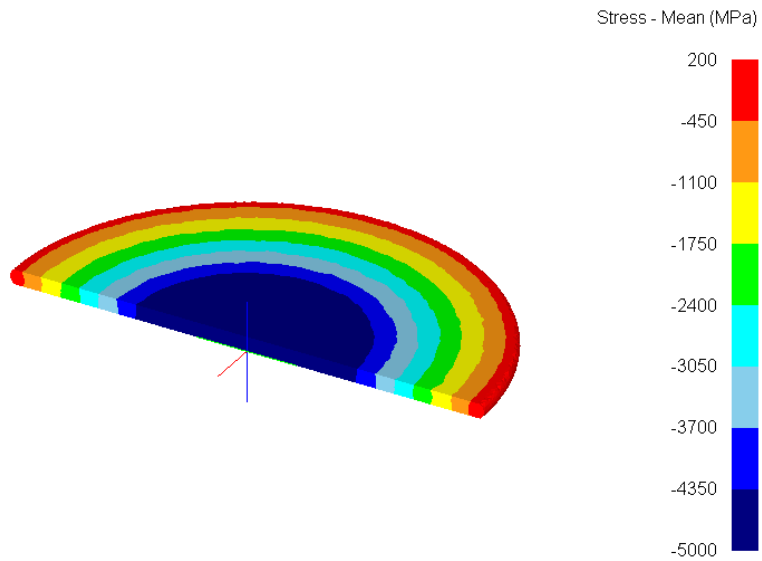


Figure 58. Mean stress distribution after compression.

As the load is exactly the same as the previous simulation, the only difference is the area which is smaller than Aluminium at the same point (after compression and after half turn), therefore, the stress achieved is higher and, as set at the same range of mean stress, a more well-speeded blue area is shown.

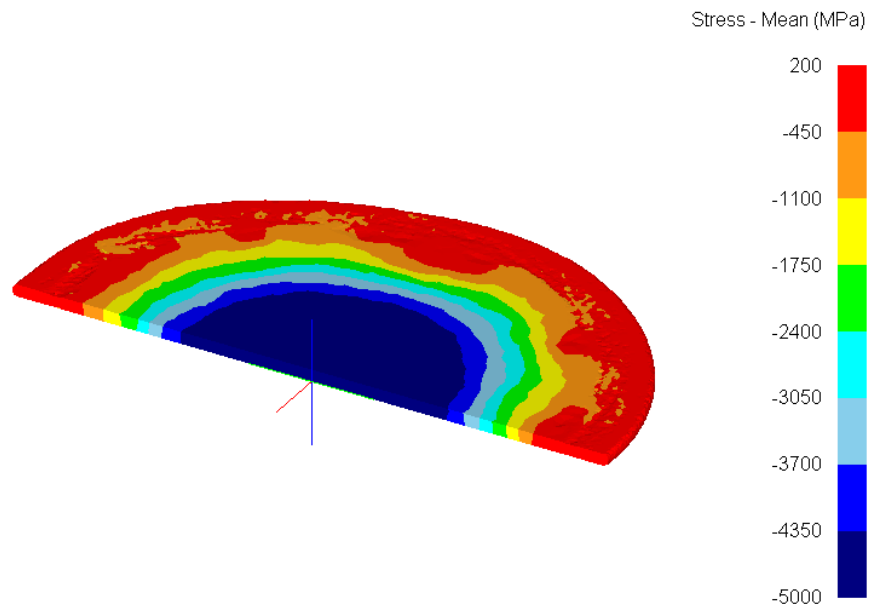


Figure 59. Mean stress distribution after half turn torsion.

The stress distribution at the end of the simulation (Figure 59) shows a little discontinuity of homogeneity at around 5 mm from the centre. This was observed as well in the strain evolution and, as strain and stress are correlated, is an expected result.

### 6.3.3.5. Torque and Load evolution

Torque evolution is shown at Figure 60. It can be seen that the value needed to achieve the torsion under the same load conditions is higher than in the Aluminium sample by a factor of 2. This is significant, as the materials solicitations will define the specifications of the machine. In consequence it is then proved that if the machine is expected to load at around 6 GPa and perform half a turn for a copper sample, it will be needed more than 375.000 N·mm.

The torque evolution along the angular displacement shows a logarithmic like model, and it can be approximated with such function.

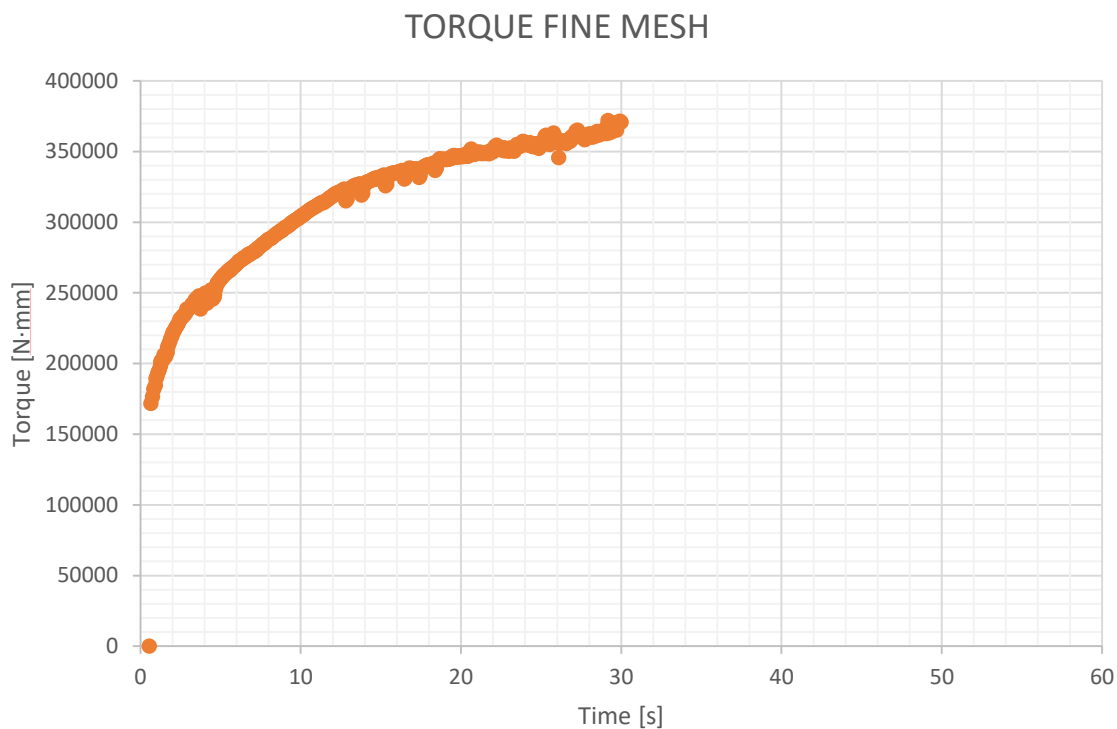


Figure 60. Torque evolution along time estimated by simulation.

It is interesting as well to observe that the torque reaches a saturation along time quite fast, as in half turn the torque stabilizes around 350.000 N·mm – 400.000 N·mm and then is expected to grow in a linear way.

### 6.3.4. Results for Aluminium sample (Real Case; 1 GPa; 4 turns; 0.61 coefficient)

Ideal simulations have proven to give good results and information about the solicitations and mesh necessities to get the simulation effectively. The ideal simulations have proven to follow the HPT theoretical equation. Using this information, new simulations have been performed with a more realistic die applied over the sample in order to get more approximate information of future experimental studies.

#### 6.3.4.1. Mesh evolution and contact points

After different simulations, multiple problems have been encountered along. The first was due to the contact set-up between anvils and the sample and the produced outflow. To define correctly these issues, different simulations were performed till attaining a constant distribution and amount of contact points between sample and dies. Figure 61 displays the strain evolution along the contact point. It can be seen that contact points are not homogeneously distributed along the contact surface, as there are many holes and they do not form a full circle.



Figure 61. (left) Effective strain and (right) Contact points between dies and sample (left). Not full contact is shown in right figure, as the contact points is not well set-up.

To solve this issue, an excessive amount of points has been set-up (as shown in Figure 64 and Figure 65) in order to get a smooth circle, and therefore assure a full contact condition between sample and anvils.

Other issue is the contact between anvils and outflow, which under the current assumptions of 0.67 coefficient anvil-sample and the sticking condition would result in false results. To solve this, a friction window has been set-up to assure that the outflow with the anvil has zero effect.

On the other hand, the mesh has been set up as a constant and fine size along the centre of the work-piece and very coarse at the outflow, as the outflow has no interest in terms of strain nor stress and therefore no precise information is needed.

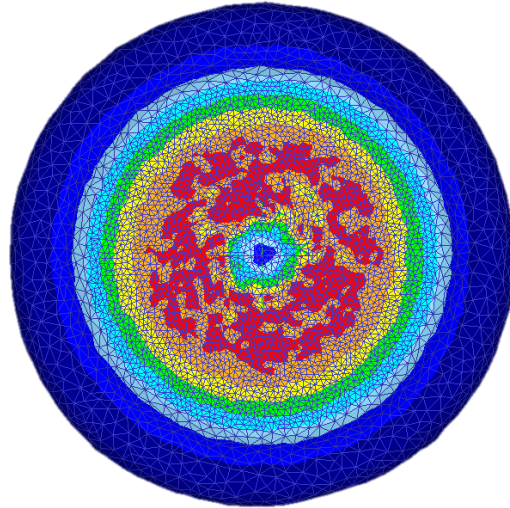


Figure 62. Mesh configuration along the real HPT aluminium 1100 simulation.

Multiple simulations have proven not to have any effect on the mesh size in the outflow, which assures that the results with the given configuration are acceptable and allows increasing the mesh size at the centre of the sample and optimizing the simulation time and resources consumptions.

#### 6.3.4.2. Deformation

Deformation has proven not to be an interesting data to gather so far in these simulations, however, the deformation of the sample outflow is an interesting point to revise.

As shown in Figure 61, the simulation evolution initially shows an outflow evolution with a small deviation to the upper anvil, while in Figure 63 it can be seen that under different loads, the evolution of the sample follows another different solution. On the other hand, this information is not really important in terms of the present simulation, as the objective is to define the evolution of the compressed and torsioned material, therefore, the evolution of the compressed part (the dark circle with green dots of right figure).

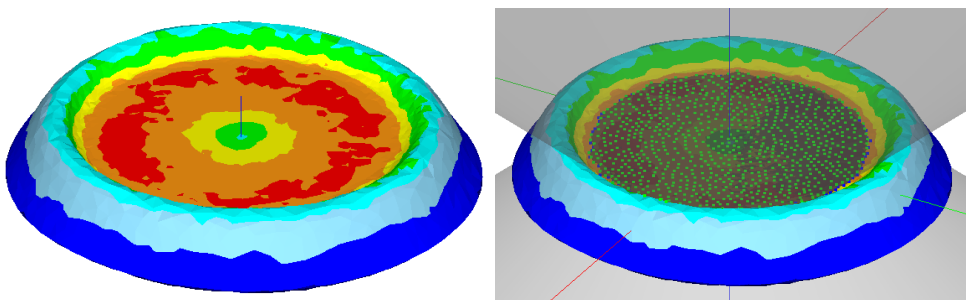


Figure 63. (left) Effective strain and (right) Contact points between dies and sample (left). Not full contact is shown in right figure, as the contact points is not well set-up.

As no information is needed of the outflow, this shows that the deformation of the outflow is obviated.



### 6.3.4.3. Strain Distribution

Under the four turns that have been performed in order to comprehend the strain evolution, figures A to D in Figure 64 show the evolution of the first turn divided in quarters.

As it can be observed, along the first quarter (image A) the strain evolution is not smooth and even though it is homogenous along the radius, is not exactly what it would be expected by literature. Checking the maximum of that image, it can be observed that maximum strain is not generated at the maximum radius of the sample (border of the anvil, 5 mm radius). Along B, C, D it is strongly appreciated a reduction of the maximum strain (red zone) and as well as displacement towards the centre, which again is contradictory with the theoretical HPT equation.

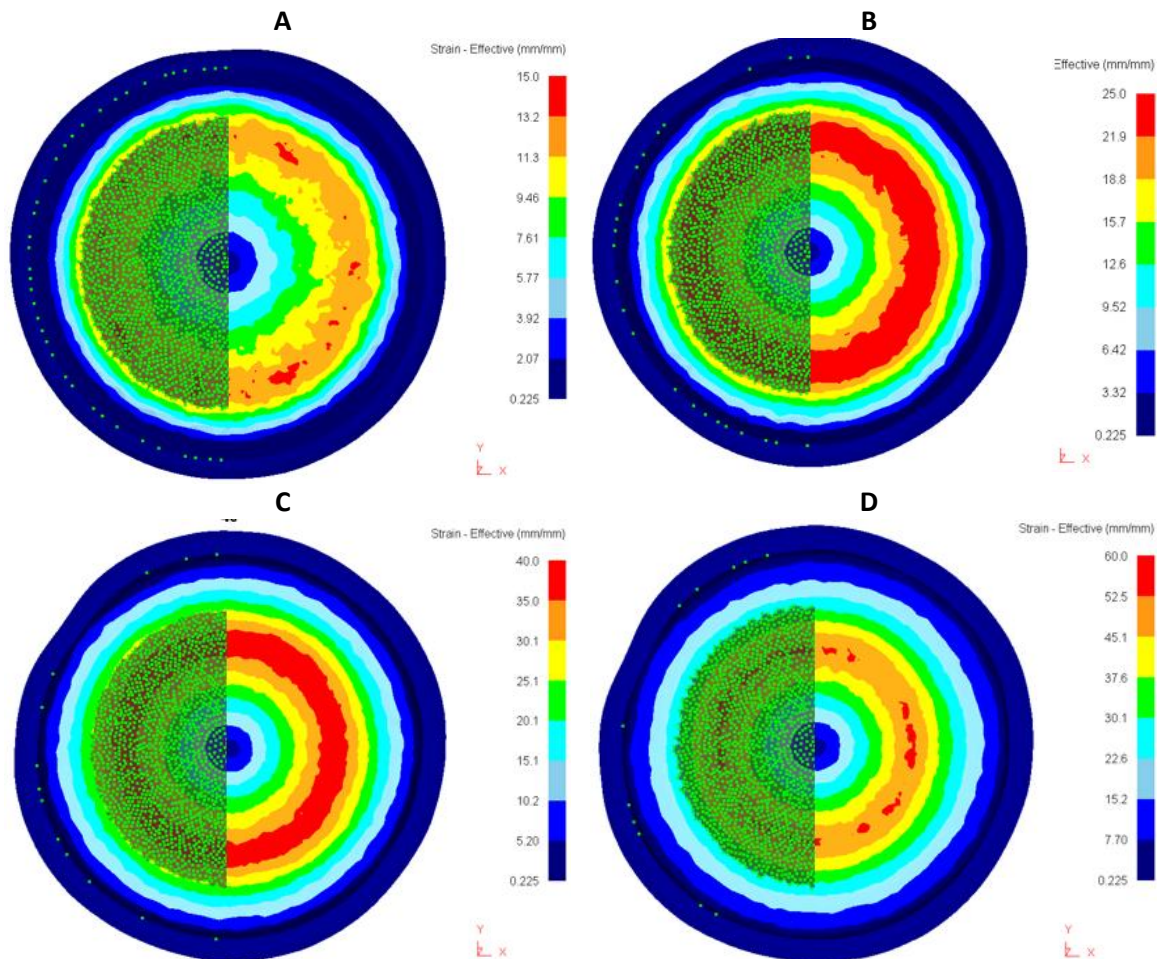


Figure 64. From A to D; evolution of effective strain for a realistic dies and coefficient model on an Aluminium 1100. A shows one quarter turn, B shows two quarters turn, C shows three quarters turn and D shows one turn. Green dots on left parts of the figures show the contact points between sample and the die (from 0 to 5mm constant radius)

To check if this keeps constant along the process, more turns have been performed as shown in Figure 65. As shown in images B, C, D the effect still is present as checking the orange range, but even more unprecedented and contradictory results are obtained, as the maximum strain start to be not uniform and erratic.

No explanations can be initially offered to this result, as the simulations are performed under ideal assumptions with no grain evolution or effect, thermal effects or recrystallization, so under idealistic solicitations the solution should follow theoretical results. The results are obtained assuming that the boundary conditions and material assumptions are correct, as all precedent simulations have given realistic results; therefore the author assumes that a boundary condition might not be correct under this circumstances, the geometry is not interacting correctly with the software or the discretisation is not good enough or even the software mathematical models or processor are not powerful or accurate enough, as the software is designed to perform typical manufacturing simulations and the present project tries to perform state-of-the-art manufacturing techniques, as HPT severe plastic deformation.

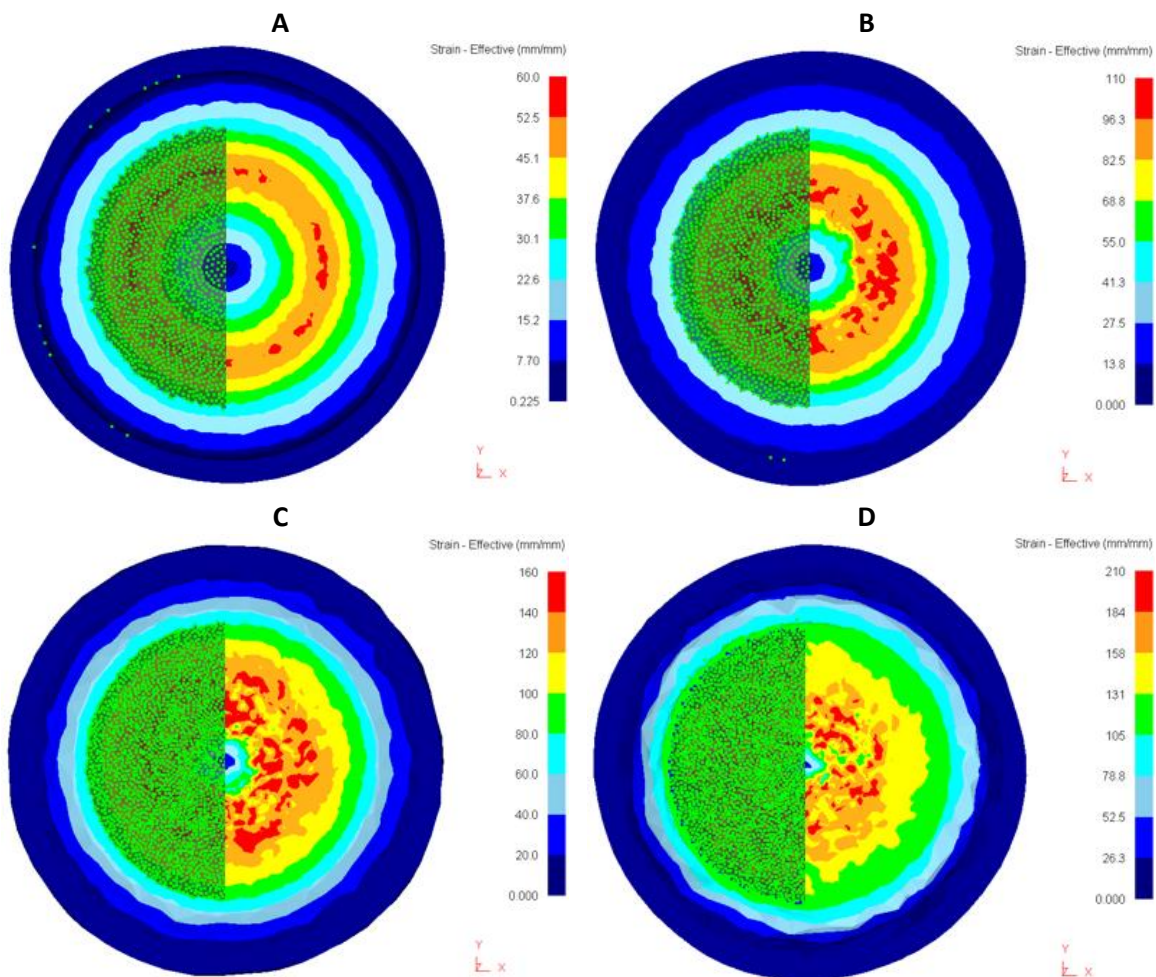


Figure 65. From A to D; evolution of effective strain for a realistic dies and coefficient model on an Aluminium 1100. A shows one turn, B shows two turns, C shows three turns and D shows four turns. Green dots on left parts of the figures show the contact points between sample and the die (from 0 to 5mm constant radius)

In the Figure 66 it can be appreciated the strain evolution along time for different points of the sample. In an attempt to understand the simulation evolution, the theoretical model of the strain under the HPT condition was plotted against the obtained data. It can be seen that the data is diverging and not following the expected pattern, giving not idealistic results.

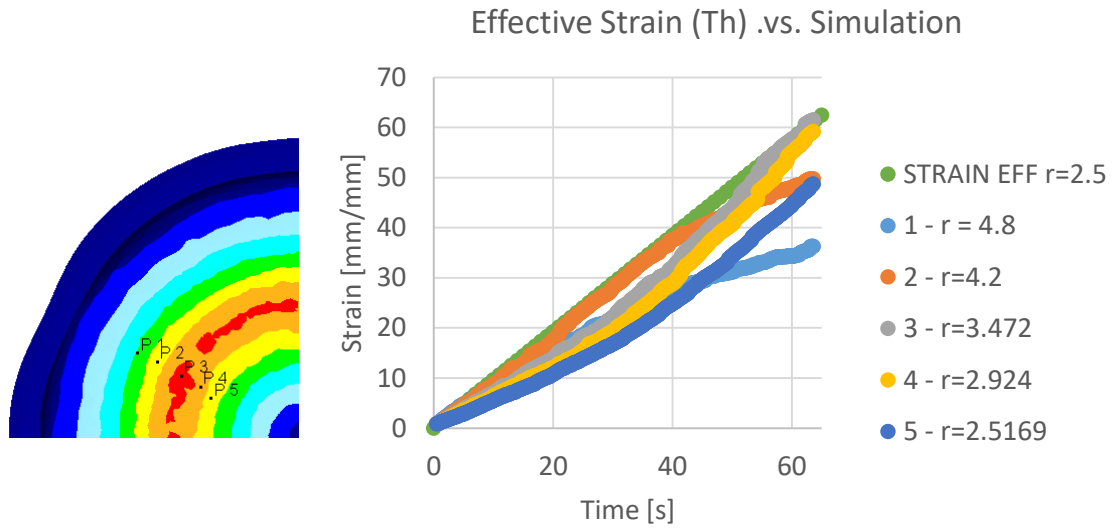


Figure 66. Strain evolution along time of different points of the sample

## 6.4. HPT Case 3: New simulation process

### 6.4.1. Introduction

Following the HPT Simulations for PROCOMAME laboratory and following a parallel project from a partner researcher from Autonomous University of México (UNAM), another case simulation study was analysed in the present report. The main idea following México's partner project is to apply the torsion and pressure at the same time with special dies. Through this simulation it is expected to establish the amount of strain, stress and buckling of different height samples.

The solicitations were established this way due to an already existent machine which movement was established as a screw movement of 5mm per revolution with a 1m length sample limit. As it has been already presented, the HPT is strictly determined by the amount of accumulated torsion due to the dies' revolution, so it is clear that to obtain greater revolutions on the sample, the height must be larger and therefore, there is a limit of height, as if the sample is large enough it can buckle as presented in Buckling section. The sample rod should be a 10 mm diameter cylinder.

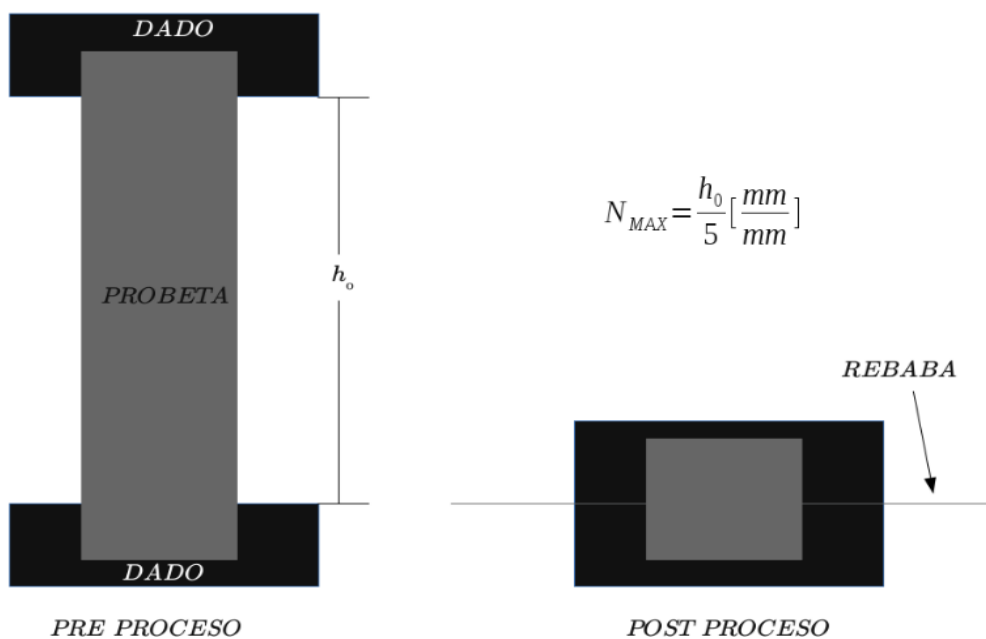


Figure 67. Exemplary sketch received by mail with the specifications for the simulations

The geometrical solicitations in terms of dies were to use their pre-design set, as they are presented in Annex B. Technical Drawings. The dies were designed with Autodesk Inventor following the adjoin construction plans.

The only material established solicitations were to use an Aluminium 1100, exactly the same Aluminium as used in the previous simulations.

### 6.4.1.1. Buckling

First of all, the buckling situations were analytically calculated using the equation (Eq. 3.6). To do so, the following parameters were used:

MAGNITUDE	VALUE	UNITS
E	68.9	[GPa]
K	0.5	[-]
I	490.87	[mm <sup>4</sup> ]

Table 7. Buckling parameters for the HPT case 3 simulation

The Young Modulus was taken from literature as it was used in previous sections (see Table 6). The K parameter is taken by the characteristics of the simulation in which both ends of the sample are theoretically fixed on the dies, and so following the Table 1 given in the Buckling section the K value is set as 1/2.

Finally, the second moment of area (a.k.a. moment of inertia) is established by the section form of the sample, in this case, a cylinder, as shown in the Figure 68.

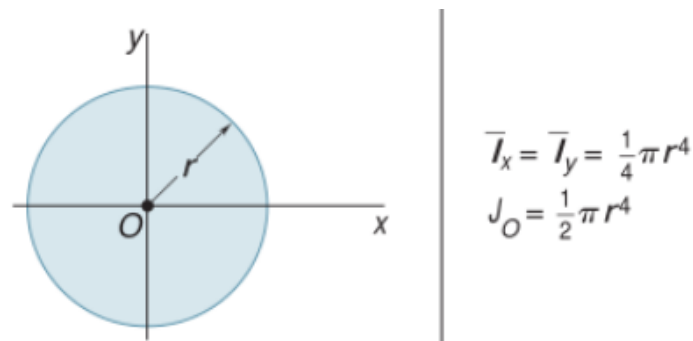


Figure 68. Second Moment of Area of a circle. (Beer and Johnston 1988)

The equation is then set as the following one (Eq. 6.2) and with the diameter set as 10mm, the previous result is obtained.

$$I = \frac{\pi \cdot r^4}{4} \equiv \frac{\pi \cdot d^4}{64} \quad (\text{Eq. 6.2})$$

Following then the Euler Buckling model with the given parameters, the plot of the amount of load needed to buckle the sample in function of its height is given in the following

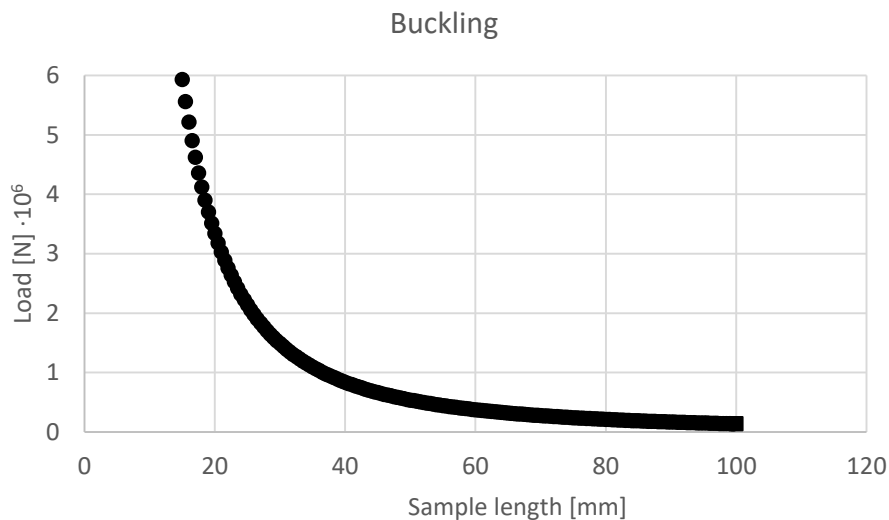


Figure 69. Plot showing the function between the sample length and the amount of load to buckle.

It can be seen that the larger the sample is, the less the load needed to buckle it. Obviously, the opposite is correct, the shorter the sample, the more the load to buckle, growing exponentially until infinity asymptotically at sample height lower than 20 mm. The present curve is plotted until 100mm, even though the machine can be used for 1000mm samples, as it can be assumed that samples larger than 100m will buckle.

#### 6.4.2. Case Study

Multiple cases have been studied under the following solicitations established in the previous section, in which the most important “free” parameter would be the friction model and its parameters. Different results were then obtained due to the amount of simulations performed, the most interesting ones will be presented, in this case varying the length of the sample until the software limitations. There will be presented then 2 set of simulations; the first set with an anvil depression for the sample and the second one with no anvil depression.

The software limitations in this case would be an unexpected buckling simulated by the FEM code. Even though DEFORM v10 presents the idea that buckling models are integrated in the Software core system, under an ideal simulation with a perfect mesh the buckling would be not possible to manifest due to the “idealist” of the simulation. Nevertheless, given the necessity of the re-meshing process along the process, the non-symmetrical mesh would be the opportunity to the sample to bend, even though it would not be a real mechanical buckling, but a meshing triggered one.



### 6.4.2.1. Geometrical Model

There are 3 given parts with geometrical definition, the upper anvil, the lower anvil and the sample. The upper and lower anvil in the first set of simulation is presented in Figure 70 while the upper and lower anvil without any depression was set as a same dimension cylindrical die with no depression.

#### 6.4.2.1.1 Sample

The sample is set by solicitations as an unspecified height cylinder of 10mm diameter. Different simulations with different sample height are performed in order to study its evolution in function of the height.

#### 6.4.2.1.2 Upper and Lower Anvil Geometry

Following the given construction drawings, the upper and lower dies are designed. The depressions have a depth of 4mm with a 10mm diameter surface at the base and 10.7 mm at the surface of the die, with an inclination angle of the depression wall of 5°.

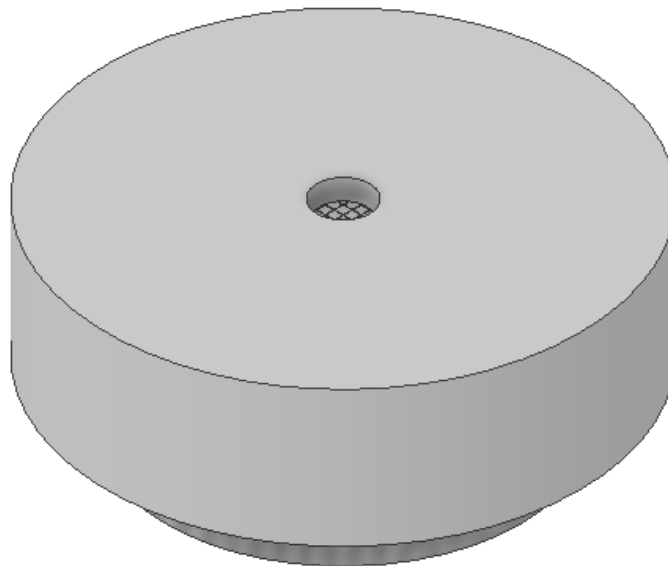


Figure 70. Upper and Lower anvil for the first set of simulations.

One of the considerations to take in account in the depression die is that the sample distance between the die's surfaces is not the same as the length of the sample. As illustrated in the following Figure 71, the depression length ( $L_d$ ) is established as 4mm per demand, while the distance between dies will be 8 mm less than the actual sample height. This is of the utmost importance to consider when evaluating the buckle effect, due to the assumption of both ends fixed, the depression length is assumed to be fixed.

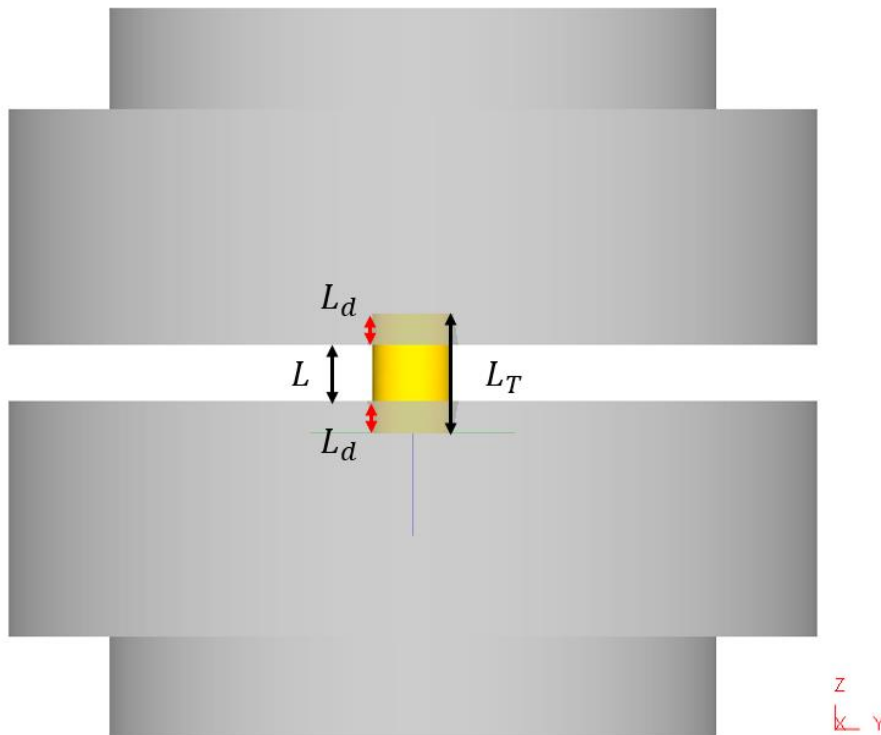


Figure 71. Different lengths in function of the depression length ( $L_d$ ), total length ( $L_t$ ) and distance between die's surfaces ( $L$ )

#### 6.4.2.2. Boundary Conditions, Solicitations and assumptions

In order to perform the simulation, boundary conditions and assumptions must be established and must be as similar as real laboratory conditions. The following assumptions have been considered:

- The temperature is established as room temperature and constant (20°C).
- No thermal activation, diffusion or thermal processes have been considered in the sample.
- There are no energetic losses of any kind (uniaxial and shear stress are applied to the sample)
- No diffusion is considered between the die, punch and sample.
- The elastic deformation of the punch and die are neglected. (Rigid condition)
- The boundary conditions on the sample, punch and die are established just as pure mechanical and time dependant (Time Domain Mechanical Deformation study).
- The Coulomb's Friction Coefficient between anvils and sample are set-up as:
  - Sticking Condition with  $\mu = 0.61$  for Aluminium – Tool Steel

No boundary conditions were set up for the sample, letting it flow in each and every direction without any constraints (understanding that the punch and die are geometrical constraints by themselves).

The 0.61 aluminium coefficient was established as dry contact between aluminium and tool steel and assuming there would be a sticking condition between die and sample.



### 6.4.2.3. External Loads and Stresses; Screw evolution

As the solicitations have no external loads nor limitations, the external loads and torque are the desired results to be obtained in this simulation, as long, of course, as the strain, stress and evolution of deformation of the sample. In this case, the established parameters are the linear displacement of both dies and the revolution of the dies along this linear movement. The screw evolution is set as 1 rotation every 5mm of linear motion of the crosshead.

### 6.4.3. Results for Aluminium 1100 sample with depression anvils

#### 6.4.3.1. Simulation 1: 13 mm sample (5 mm length between dies)

##### 6.4.3.1.1 Deformation evolution

As expected from the beginning, the compression and torsion loads lead to an outflow of material along the z-plane as it can be seen in the Figure 72. The top and bottom parts are exactly the same due to the imposed and expected condition of no deformation due to the rigidity of the dies, which once fulfilled by the sample, remain exactly the same.

It can be seen a 36% of height reduction and a very huge outflow of disk material.

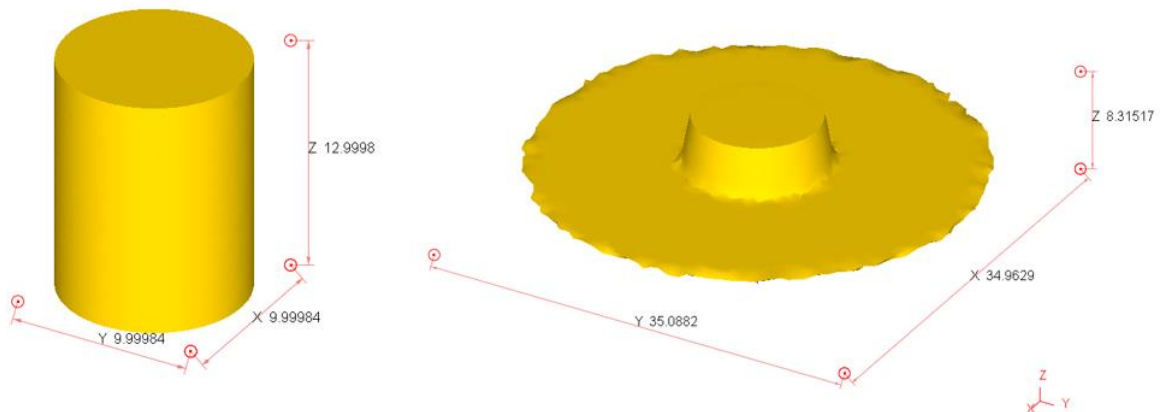


Figure 72. Sample evolution for a 13mm length sample

##### 6.4.3.1.2 Strain distribution

The strain distribution shows an interesting result not expected at the beginning. It was expected that the strain distribution would show higher strain at the centre of the sample, but as it can be seen, simulations show that the highest strain is actually at the outflow of the material near the sample location, as the highest amount of strain is as well at the outflow.

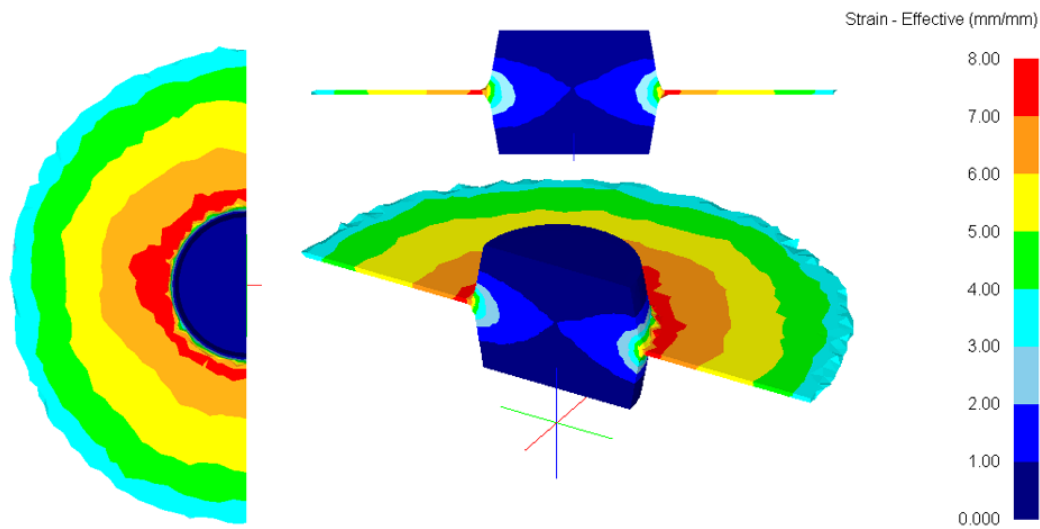


Figure 73. Strain distribution at the end of the process for a 13 mm length sample.

This is a very interesting fact, as it shows that the actual interesting part to keep would be the external outflow part of the sample rod, but not the rod itself *a priori*.

#### 6.4.3.1.3 Stress distribution

The stress distributions add actually more information to the strain distribution, as it can be seen, the highest stress is found at the outflow and at the centre of the sample and it slightly differs from where the highest strain can be found. The maximum pressure is around 2.5 GPa of compression.

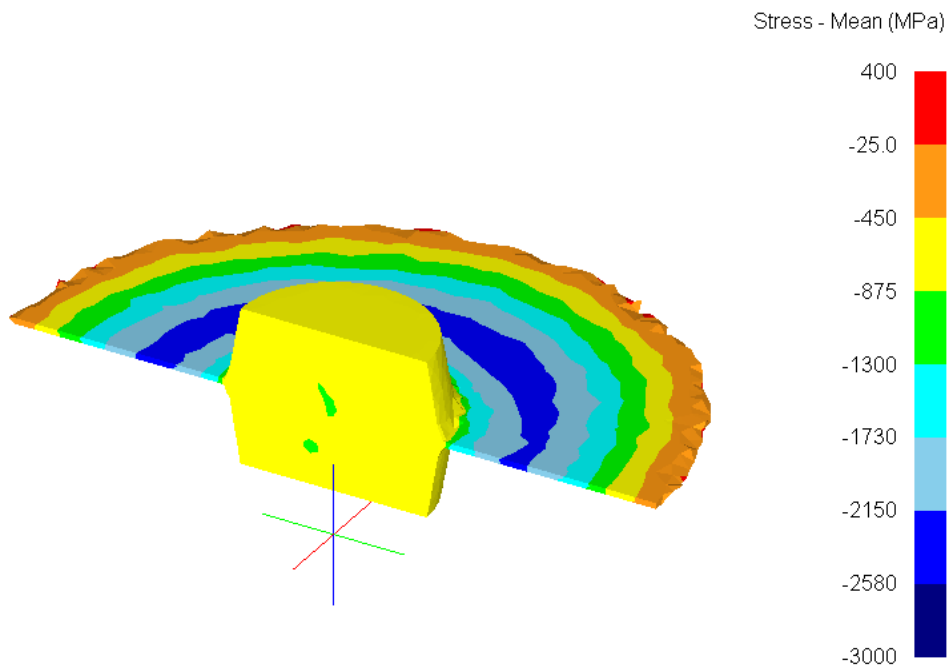


Figure 74. Strain distribution at the end of the process for a 13 mm length sample.

## 6.4.3.1.4 Torque and Load evolution

The load evolution in function of the sample length shows that the closer the dies are together, the higher the load is. It can be seen as well that the following curve fits an exponential form, reaching top loads of  $10^6$  N.

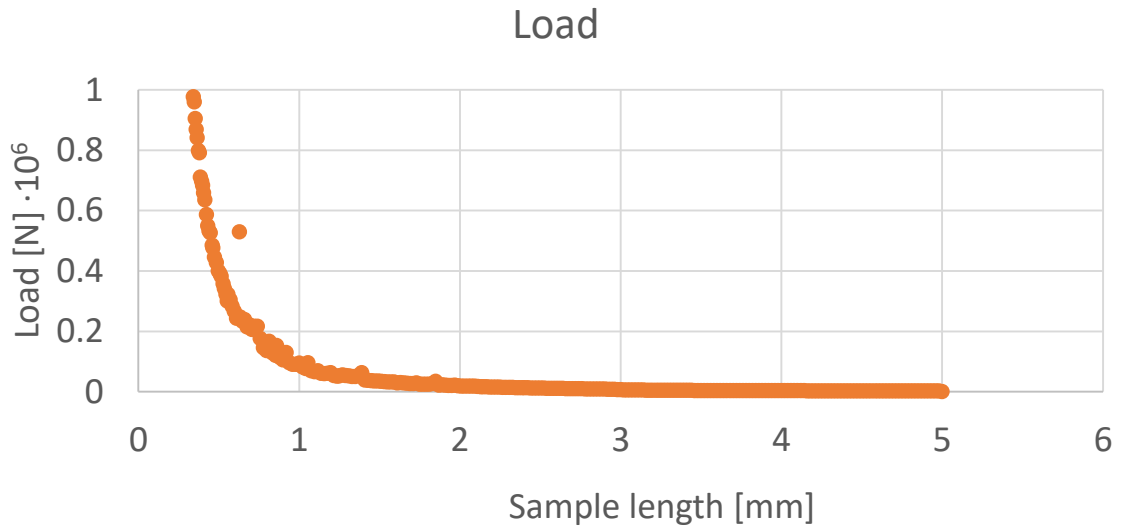


Figure 75. Load as a function of the sample length (for sample length within dies of 5mm)

The torque evolution shows an exponential growth parallel to the load evolution, with a top value of approximately 900 N·m. No saturation is shown as for example in HPT constrained or semi-constrained type B, which makes sense, as the new configuration applies a continuous stress and torsion, not allowing the system to stabilize.

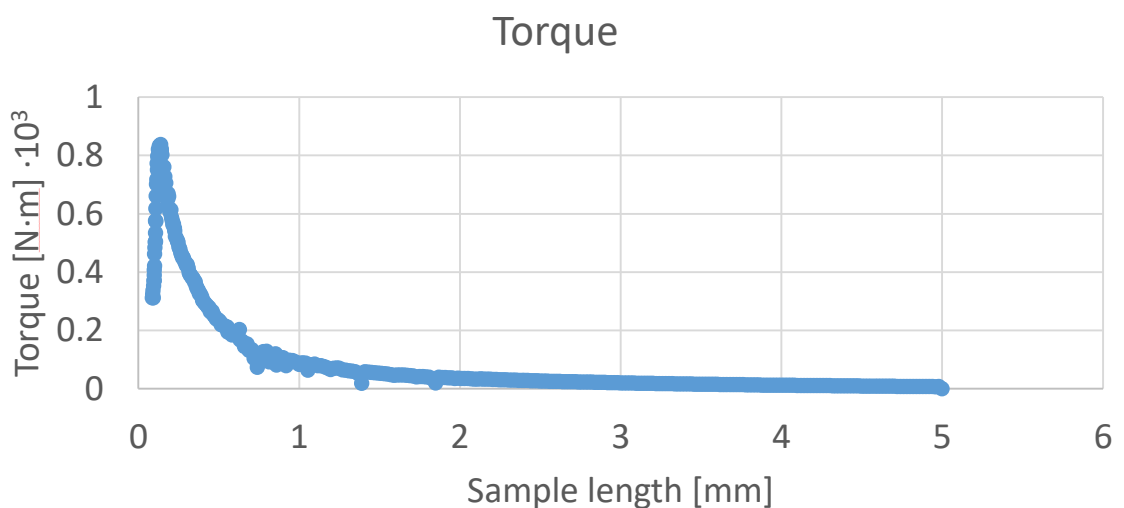


Figure 76. Torque evolution as a function of the sample length (length within dies of 5mm)

### 6.4.3.2. Simulation 2: 48 mm sample (40 mm length between dies)

#### 6.4.3.2.1 Deformation evolution

Continuing with the simulations, the deformation follows the same pattern as previous simulations with a huge amount of outflow with a bigger radius. As it can be seen, the total height is 8.87 mm, which leaves the outflow then as 0.87 mm height. The inner radius is still 5mm, while the outflow radius total is ~62 mm. This is an actual improvement in severe plastic deformation through HPT process if the data is contrasted under empirical tests, as normal HPT are done under 5mm radius samples and with this method there would be an enhancement of factor 12 of enlargement.

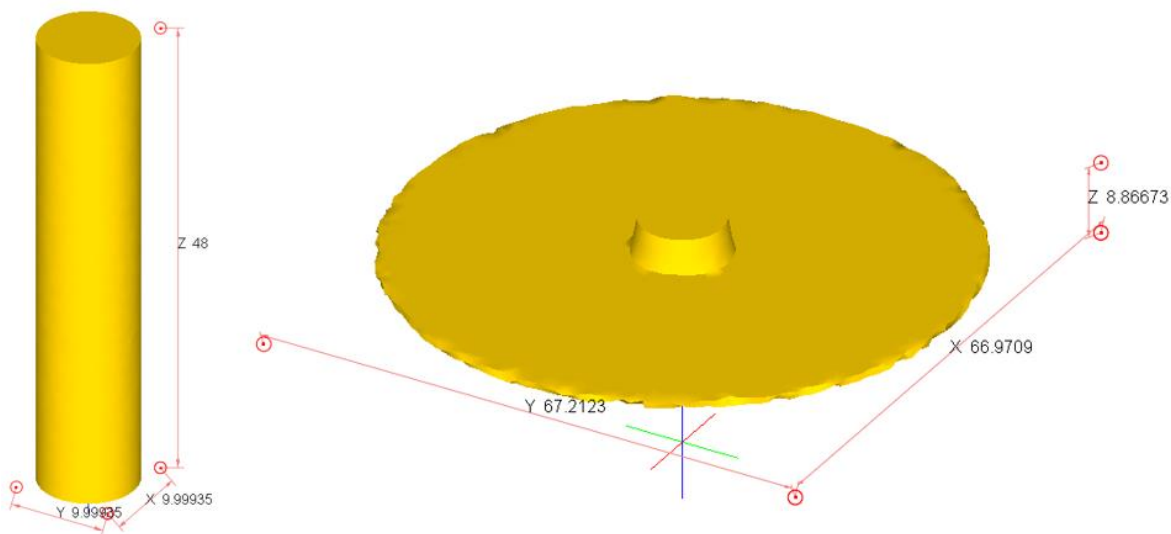


Figure 77. Sample evolution for a 48mm length sample

#### 6.4.3.2.2 Strain distribution

The effective strain reveals a huge amount of deformation around the sample rod, precisely in the outflow. The amount of strain is enough to assure a severe plastic deformation and, therefore, a bulk nanostructured material, if the simulations are assumed as correct. Comparing with Simulation 1: 13 mm sample (5 mm length between dies) section, it can be seen that the strain accumulation is actually twice as much as the 13 mm length.

It is interesting as well to check how the strain evolution along the radius is constant and homogenous, which obeys the theoretical equation.

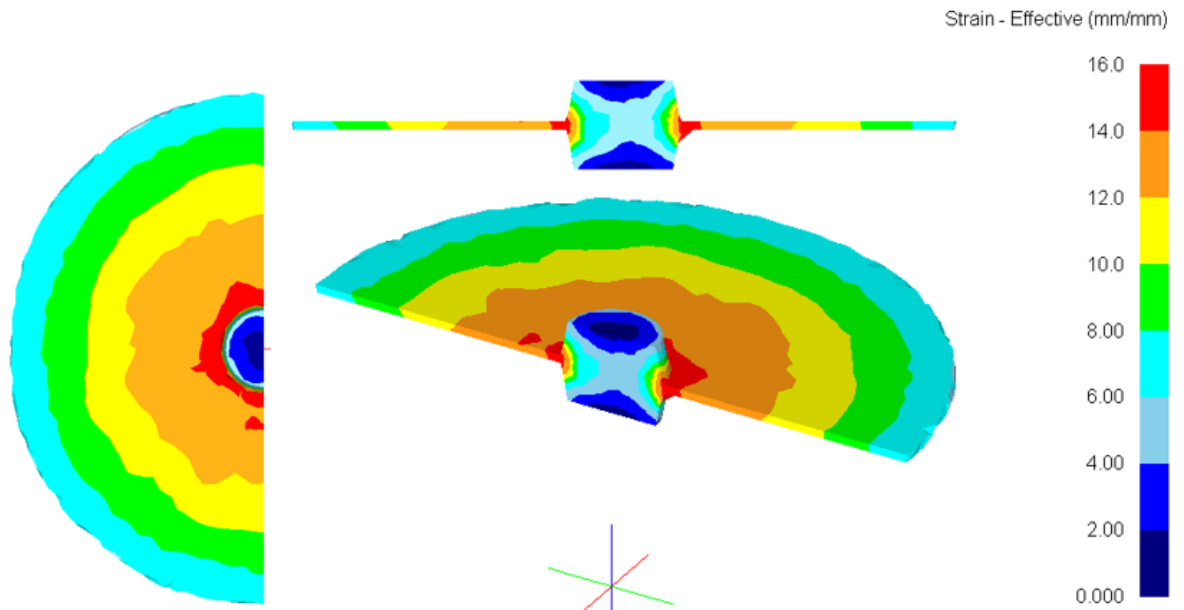


Figure 78. Strain distribution for a 48mm length rod with the new HPT method.

#### 6.4.3.2.3 Stress distribution

The stress distribution follows the same pattern as the previous one in terms of distribution and in terms of values. This is due to the fact that the sample outflow has the same thickness, therefore the necessary pressure is the same for the unchanged material.

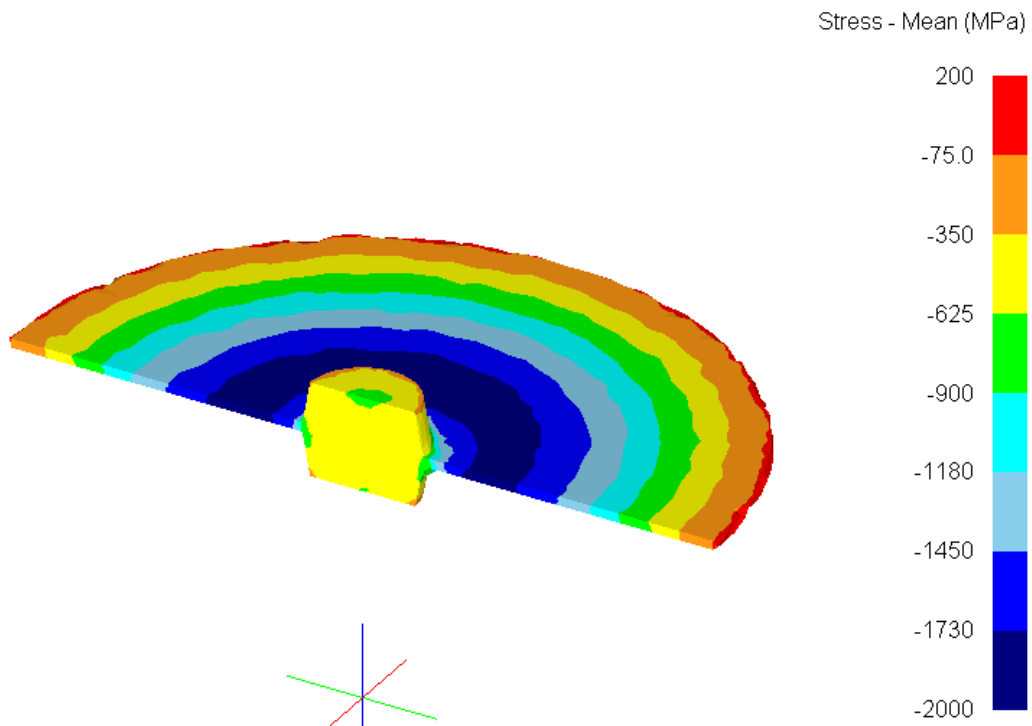


Figure 79. Strain distribution at the end of the process for the 48 mm length sample.

#### 6.4.3.2.4 Torque and Load evolution

Load and torque evolution follow exactly the same pattern as shown in the previous section for the 13mm length simulation.

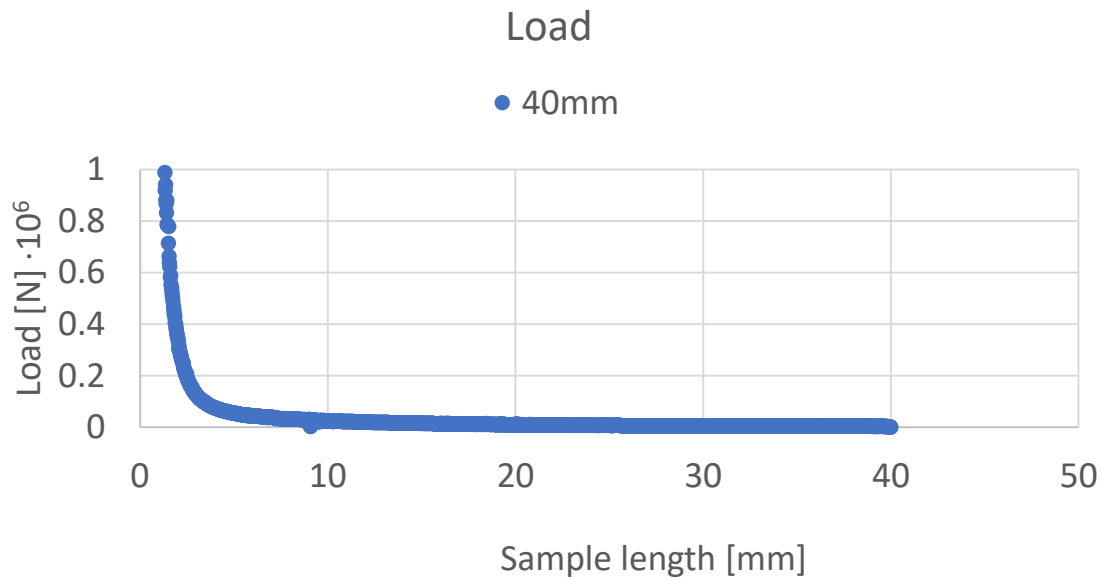


Figure 80. Load vs time evolution for the sample length of 48 mm sample (40 mm between dies)

The load follows a hyperbola, growing toward the infinite as the sample length approaches to zero, as the external forces required to deform the material become unattainable.

As shown in Figure 81, the torque evolutions grows as well.

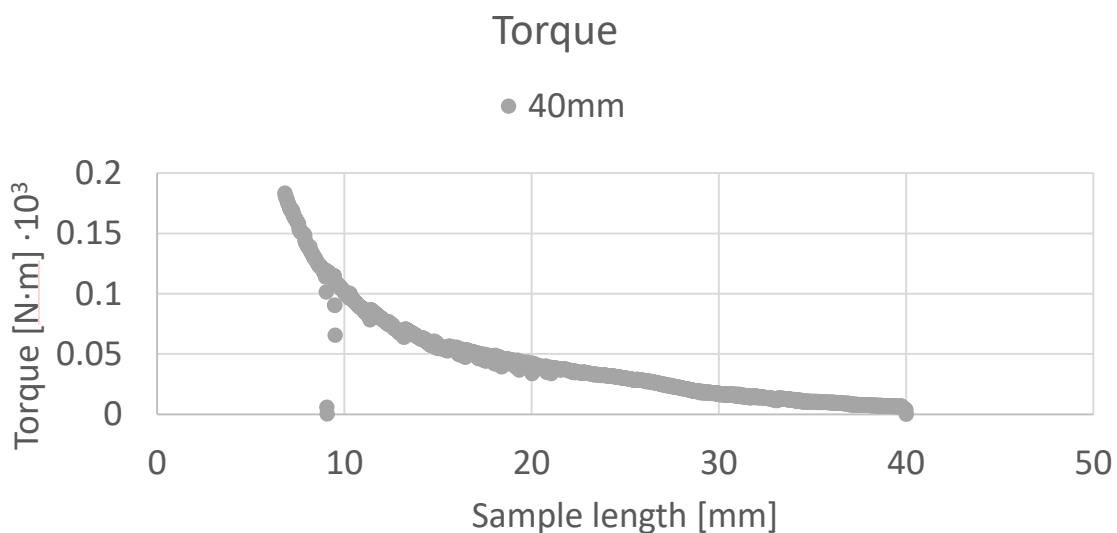


Figure 81. Torque evolution of in function of the sample length for a 48 mm sample (40 mm between dies)

### 6.4.3.3. Simulation 3: 78 mm sample (70 mm length between dies)

#### 6.4.3.3.1 Deformation evolution (buckling)

When the 78mm length sample was simulated, an unexpected event was obtained. Even though, due to the loads obtained in previous simulations it was expected to have a buckling effect around this sample length, it was not expected to be simulated due to the nature of the finite element method.

The method is based under idealistic situations, where there are no eccentric loads which motivates the buckle, nor uniform pressures over the sample surface, not only there are no discrepancies between those phenomena, but the discretisation of the model should be completely uniform due to the axial symmetry along the simulation.

To find the buckle effect is then not a realistic simulation of what would happen in reality, but a simulation limit, over which larger sample simulations would inevitable buckle, giving not useful data.

A possible explanation might be the non-uniformity mesh distribution due to the mesh and re-mesh system as explained in previous sections and after multiple attempts with different mesh configurations, no better results were obtained.

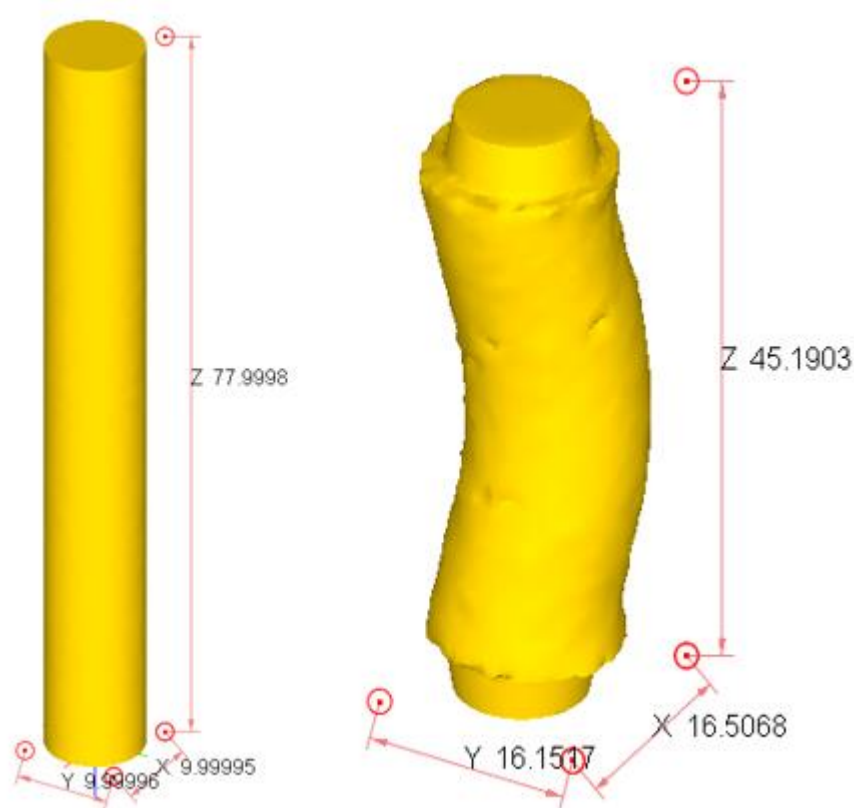


Figure 82. Buckling effect due to meshing effects in the 78 mm sample

#### 6.4.4. Results for Aluminium 1100 sample without depression anvils

Further simulations have been performed by solicitation from México in order to have comparable data. Following the Figure 83 schematic, the new simulation is done without any depression to observe the evolution of the sample and stress, strain distribution.

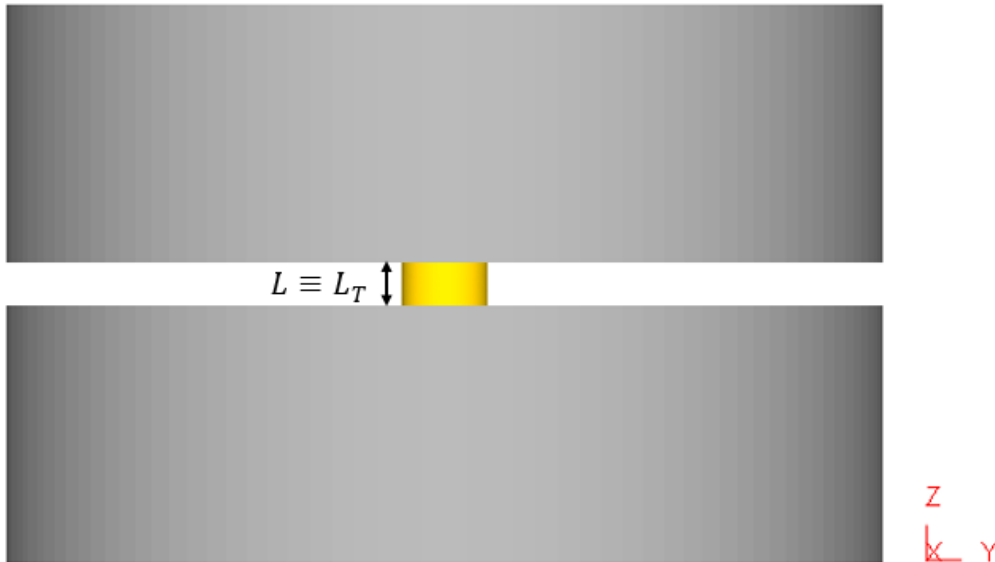


Figure 83. Total length ( $L_T$ ) and distance between die's surfaces ( $L$ ) are equal under this new simulation set with no depression.

##### 6.4.4.1. Simulation 1: 5 mm sample

###### 6.4.4.1.1 Deformation evolution

The deformation along the new set of simulations with no depression shows a plain deformation compared to the previous simulation with depression. This is due to the absence of the depression which maintains the sample rigidly. The sample proves to be similar to the studied in the HPT Case 2: Unconstraint section due to the similarities of the simulation, even though here it is important to remember that the pressure and torsion are applied at the same time.

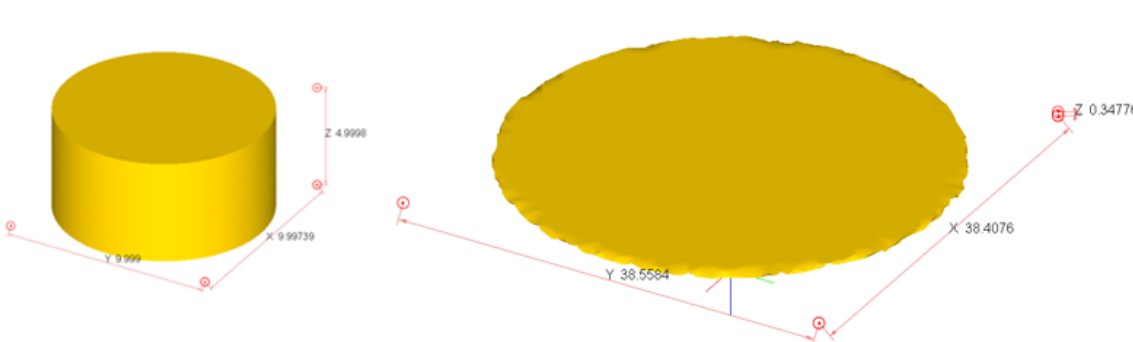


Figure 84. Deformation evolution at the beginning and at the end of the Aluminium 1100.



#### 6.4.4.1.2 Strain distribution

The strain distribution proves to be not fully homogenous, as for example in Figure 85 the green region (strain between 6 – 7.5 mm/mm) does not show a smooth contour. It is interesting as well to observe that the strain evolution along the radius follows an increment until a maximum, and then it decreases slowly, finding this maximum strain around the 5-10 mm radius.

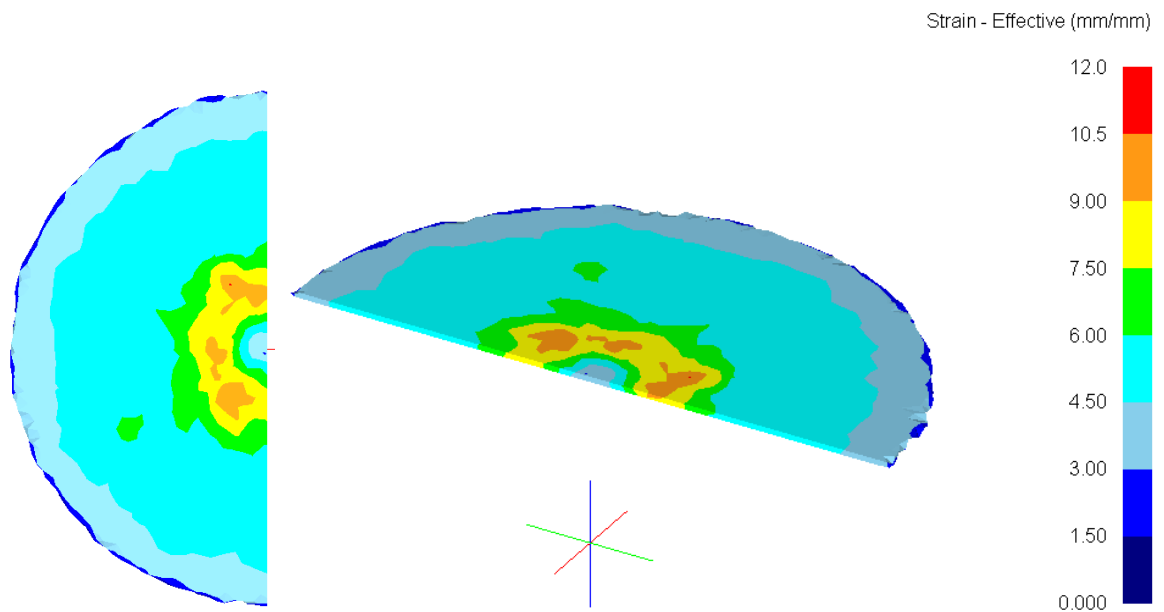


Figure 85. Strain distribution of the sample

The amount of effective accumulated strain is enough to consider a severe plastic deformation along the sample and the results prove to be interesting to perform an empirical experiment.

#### 6.4.4.1.3 Stress distribution

The stress distribution (shown in Figure 86) shows an enormous value for the present simulation. As it can be seen in the centre of the sample, to deform the work piece a 30 GPa load is required, which is an almost impossible value to reach. This is due to the simulation parameters, as the simulation is performed from the initial sample until this very thin disk, there is a stress evolution along this process.

As the disk is so deformed and thin, very high pressure must be achieved, especially along the last steps. The load evolution (as shown in Figure 87) reflects exactly this effect, which will be explained in the next section.

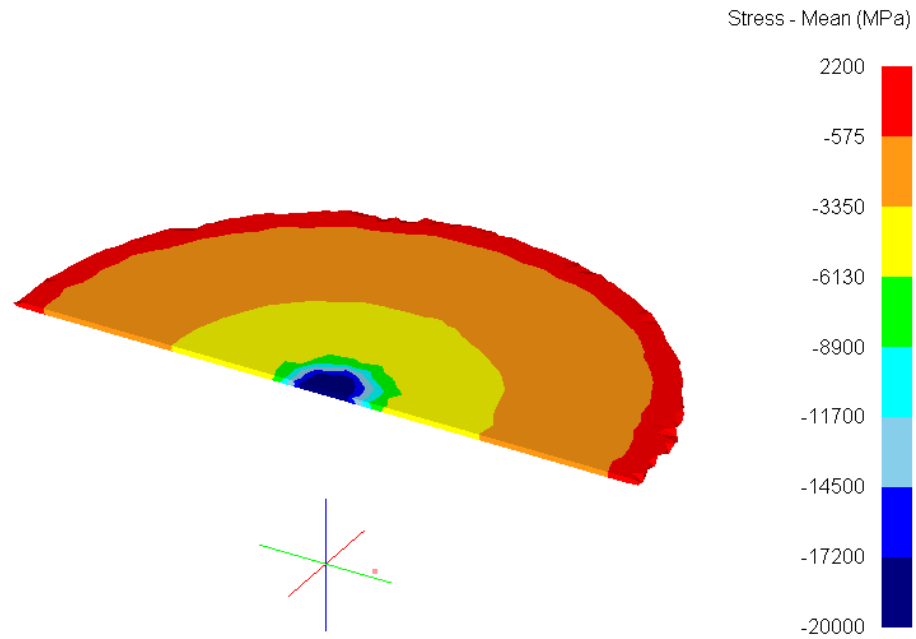


Figure 86. Stress distribution of the sample

#### 6.4.4.1.4 Torque and Load evolution

Figure 87 shows the load evolution along the sample height, it can be seen that average load values are of the range  $10^3 - 10^4 N$  and then a peak of  $10^7 N$  is achieved under 1 mm length. This extreme value is due to the enormous forces required to diminish the sample thickness from under 0.5 mm, which is an extreme case.

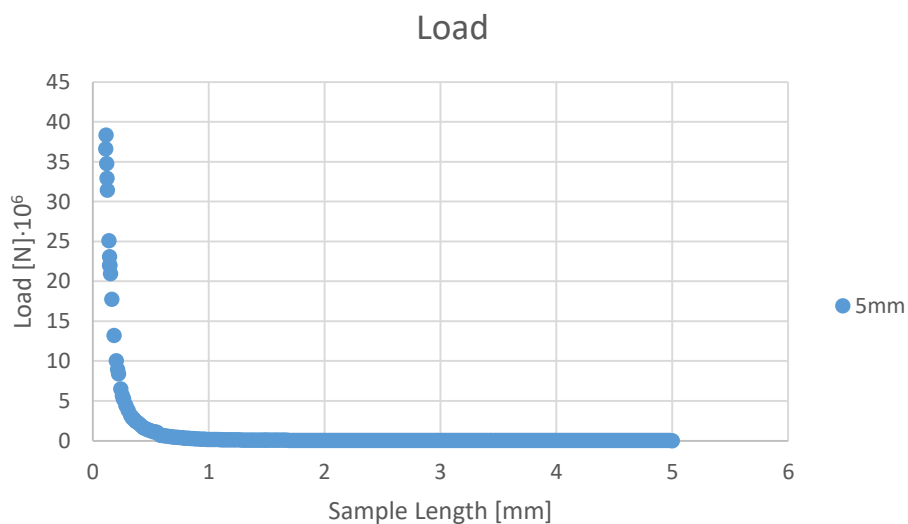


Figure 87. Load evolution as function of time.

Following the torque, the same situation as the load is found. The average torque is between  $10^1$  –  $10^2 N \cdot m$  while the maximum achieved value is  $10^3 N \cdot m$ . Again, the torque necessary to shear the material under 0.5 mm becomes almost unattainable for such a small thickness.

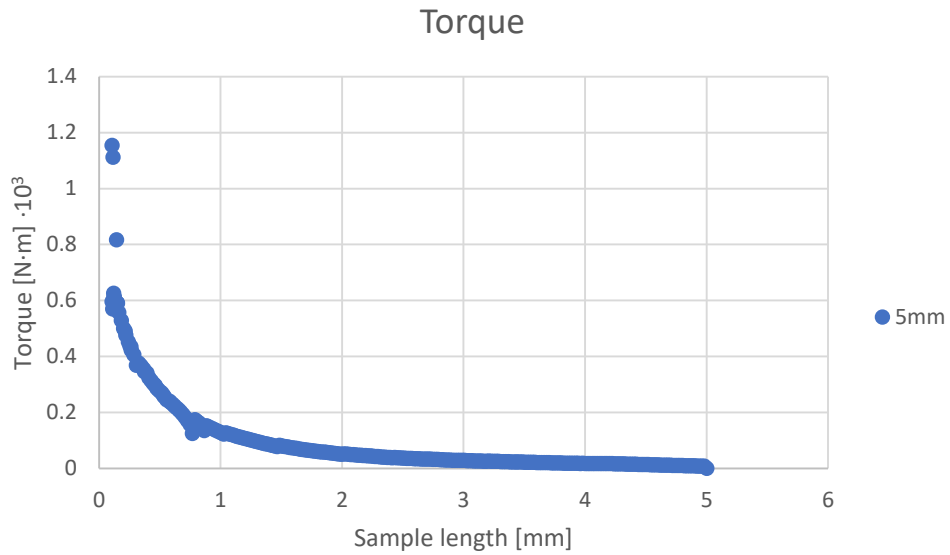


Figure 88. Torque evolution as function of time.

#### 6.4.4.2. Simulation 2: 25 mm sample

##### 6.4.4.2.1 Deformation evolution

The deformation follows the same pattern as established in the section Simulation 1: 5 mm sample, with no huge differences.

The important differences are shown in stress and strain distribution.

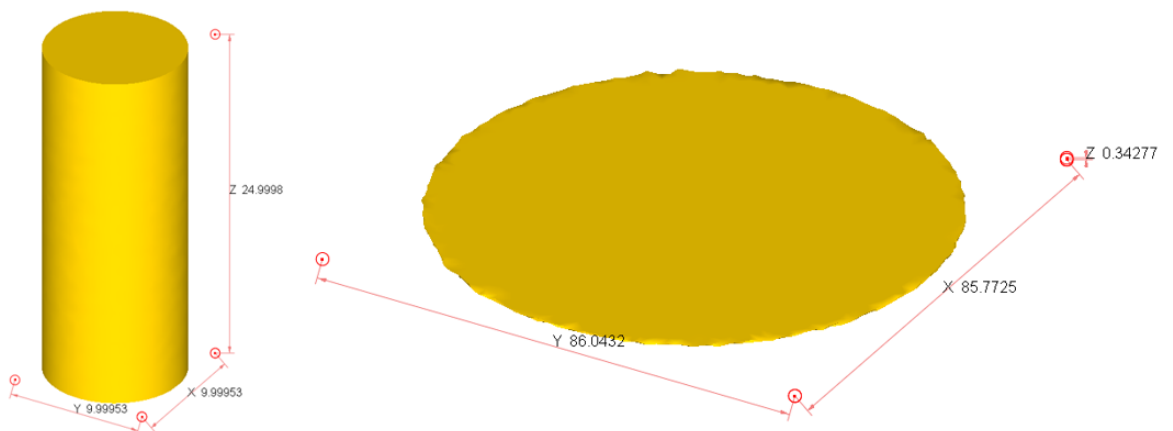


Figure 89. Deformation evolution at the beginning and at the end of the Aluminium 1100.

#### 6.4.4.2.2 Strain distribution

Strain distribution shows a very inhomogeneous evolution along the sample, with an average strain ranging between 6.25 to 8.75 mm/mm. The strain distribution is very different from the previous simulated one under 5mm sample, where there are located punctual areas where the strain is higher than the presented under this simulation, whereas the average strain is way lower to the 25mm sample.

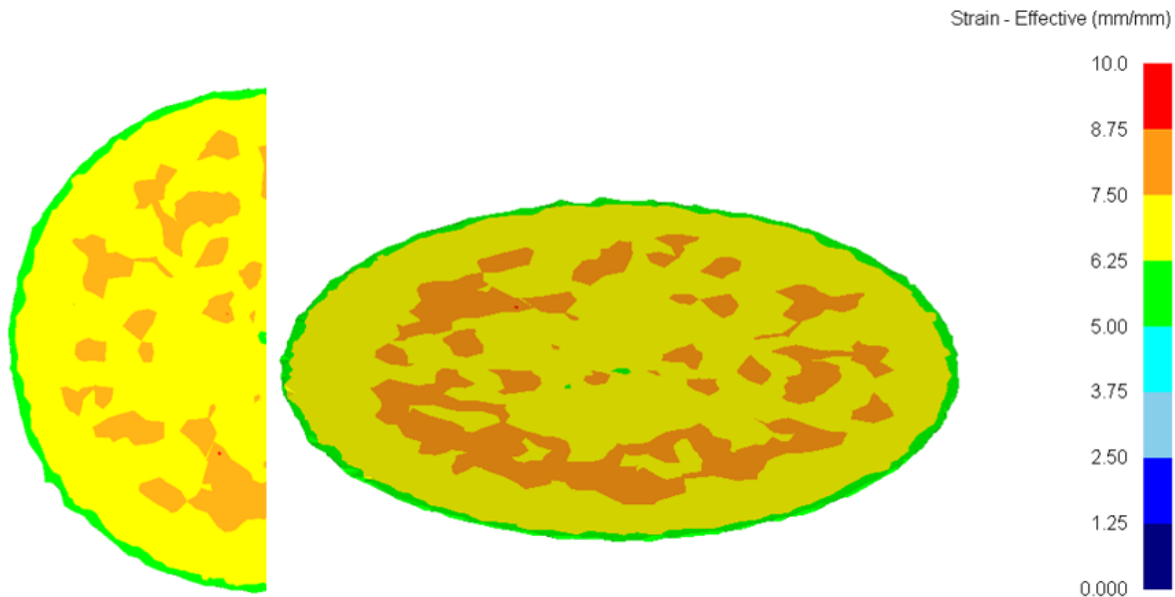


Figure 90. Strain distribution of the sample at the end of the process

It is clear that the advantage of using a higher sample is that it will result in a larger work piece with a more homogenous strain.

#### 6.4.4.2.3 Stress distribution

In terms of stress, the Figure 91 shows that the stress distribution follows the same pattern as the previous simulation with a more well distributed stress along the radius.

It is interesting as well to notice the outstanding compressive value required to reach such deformation (20 GPa), which is very high.

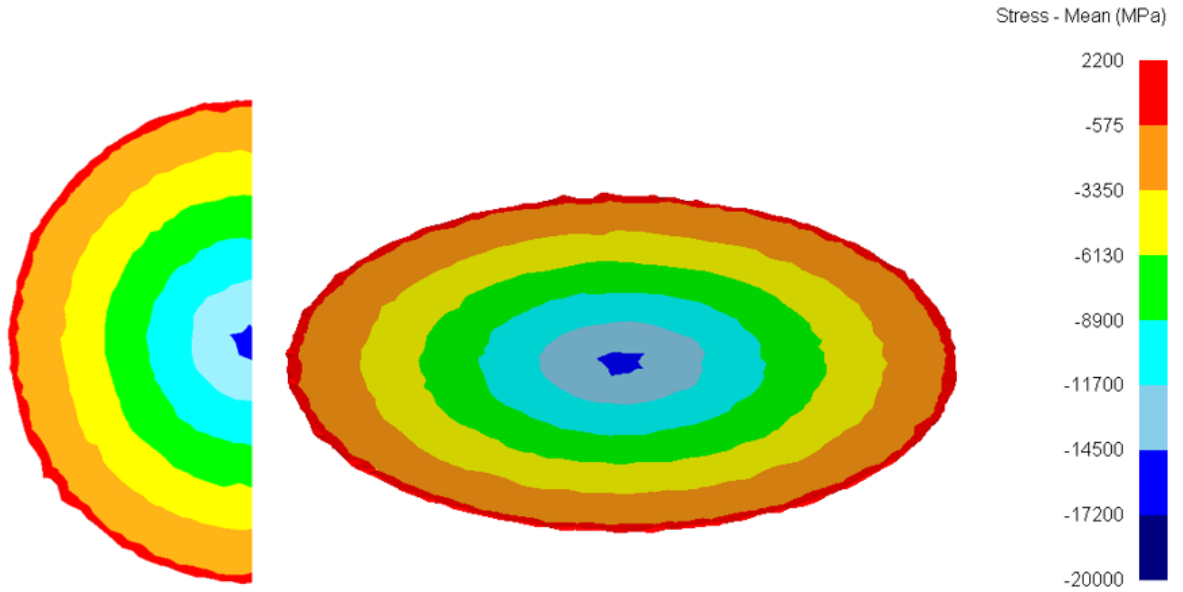


Figure 91. Stress state of the sample after the HPT case 3 process

#### 6.4.4.2.4 Torque and Load evolution

Load evolution follows an exponential evolution along the compression. It can be seen that under very low thickness values of the sample, the load required to deform the materials escalates very quickly to unattainable required forces. This is due to the fact that no force limitations have been set-up under the simulation, and the software tries to estimate the required forces to deform the material under very low height.

It is interesting to see how most of the deformation is done under the  $10^2 - 10^3 N$  range, while under 1 mm, the maximum reaches around  $10^7 N$  values.

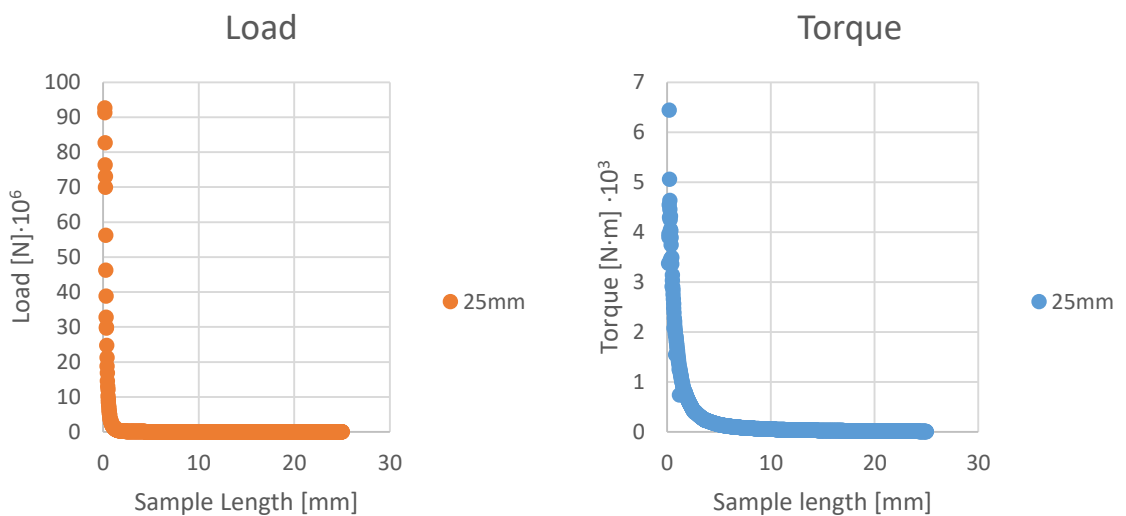


Figure 92. Load and torque evolution as function of time.

### 6.4.4.3. Simulation 3: 40 mm sample

#### 6.4.4.3.1 Deformation evolution

The simulation under no depression shows an earlier buckling comparing to the previous simulations. As it is shown in Figure 93, the samples axis is no longer following the pressure axis, which will eventually create shear stress distribution along the sample and eventually break it, without reaching the expected results.

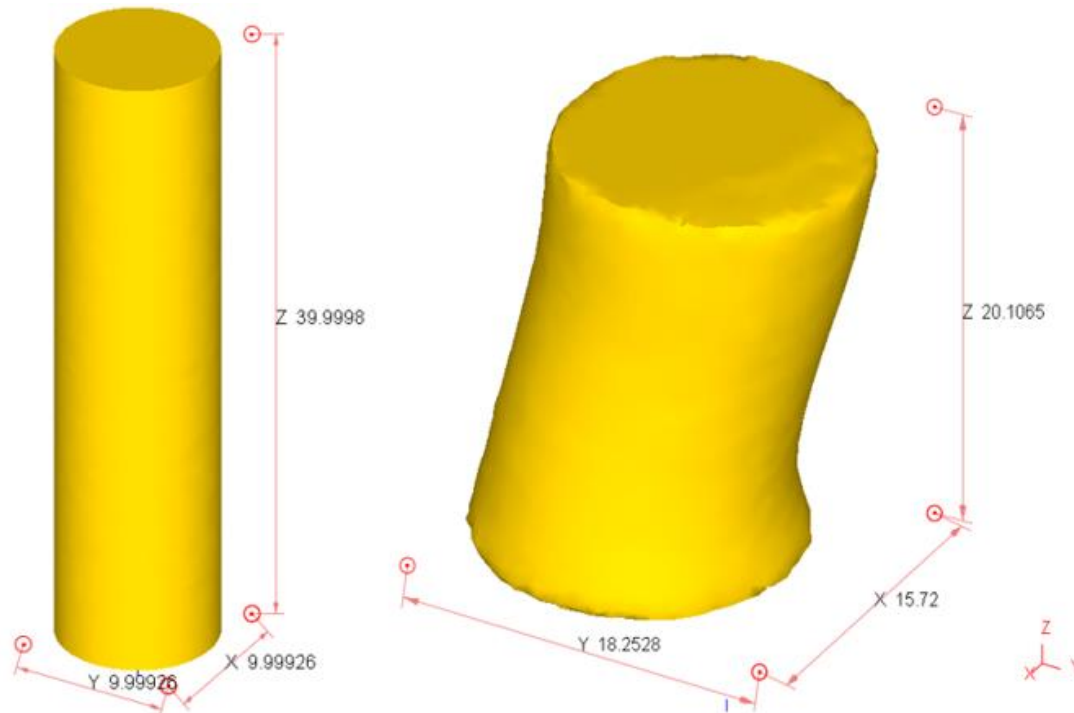


Figure 93. Deformation of the sample (Buckling)

Under these circumstances, the software (DEFORM v10) cannot simulate the deformation evolution due to the highest results and the low tolerance established, and therefore the simulation just stops.

## 6.5. Comparison between different cases and literature

### 6.5.1. Comparison of strain evolution

#### 6.5.1.1. Aluminium

In the set of images in Figure 94 it can be seen the different HPT case simulation illustrated along the project, semi-constraint type B, unconstraint and the HPT Case 3: New simulation process. As it is shown, the strain values and distributions are different for each and every case.

It can be observed that along the HPT semi-constraint type B and the HPT Unconstraint under the Ideal Case simulation the distribution pattern is the same, even though the values are different. This is due to different case solicitations that have been performed along the simulations. HPT semi-constraint was done under a 1.25 GPa and after 1 full turn, whereas the Unconstrained Ideal case was developed under approximately 6 GPa and only half turn. The difference of the strain is due to the applied pressure, which creates a bigger deformation and the fact that the disk radius is way larger due to no constraint limitations allows, as following the equation (Eq. 3.3), to have a higher strain.

The Real Case (image C) is a little bit aside from the other simulations, as the results do not follow the expected pattern. The values are approximately the same as the Unconstraint Ideal Case under 1 turn and under 1.25 GPa, what contradicts with the information given before, as the radius is limited to 5mm due to the anvils configuration. Another incoherence is the fact that the maximum strain is not at the periphery of the anvil, as it should, following the equation (Eq. 3.3).

Image D and E shows the new HPT method to study under a machine that applies pressure and torsion at the same time. The strain distribution is completely different from the HPT Unconstrained and semi-constraint type B as it is clearly seen in the figure. The strain values are as well way lower comparing to the previous ones, even though the sample size is way larger than other methodologies.

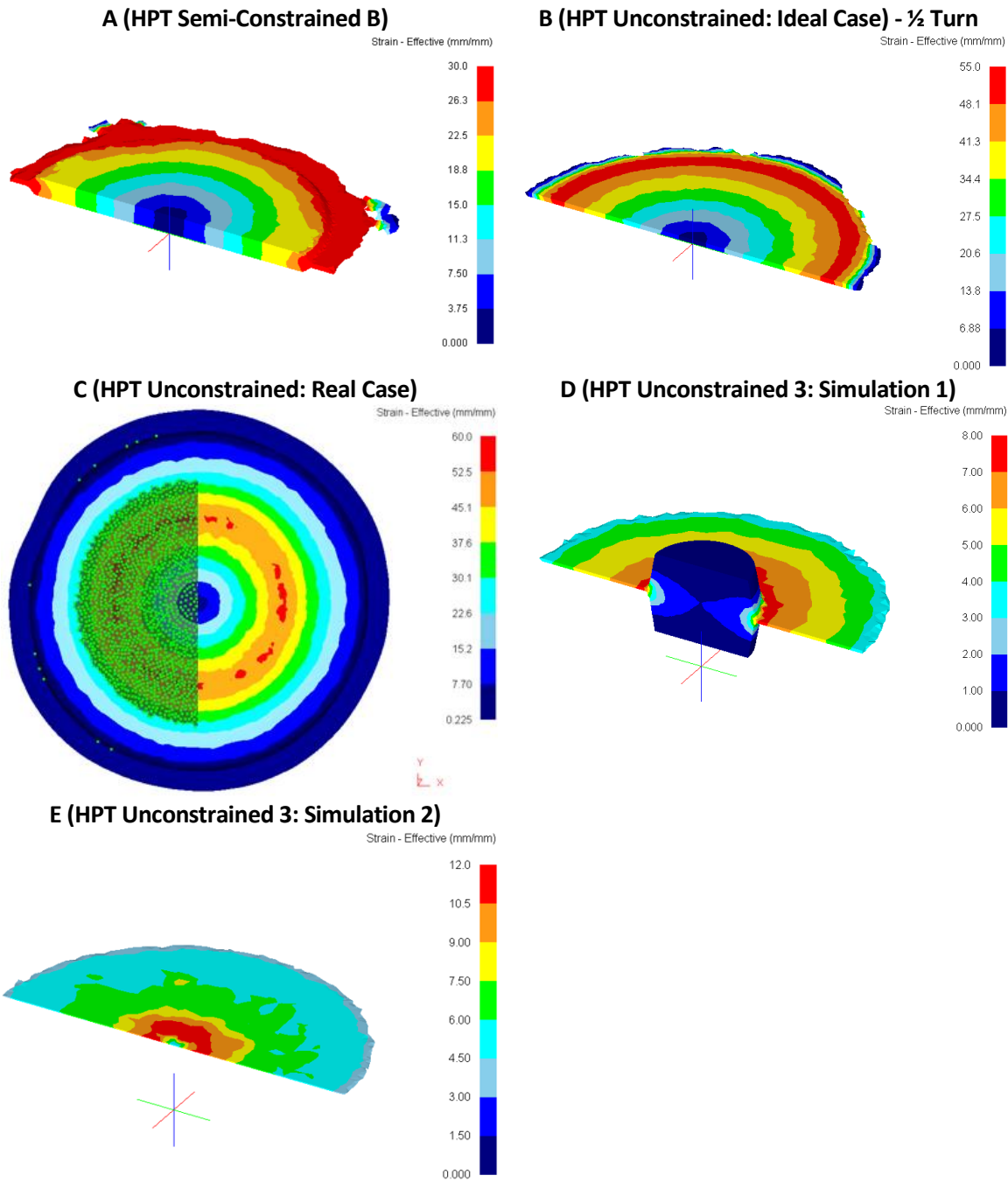


Figure 94. Strain distribution of Aluminium samples under different simulations at the end of the process. A illustrates the HPT semi-constrained type B simulation under ideal solicitations, B illustrates the HPT unconstrained simulation under ideal solicitations, C illustrates the HPT unconstrained simulation under real solicitations, D and E illustrates the HPT unconstrained simulation under case 3 simulation set; pressure and torsion applied at the same time.



### 6.5.1.2. Copper

Following with Copper samples in the Figure 95, the same situation as the Aluminium case is found. It is interesting to observe the images A and B as they are following two different friction models. The image A, following the shear friction model under a coefficient value of 2 shows a little bit less of strain reaching up to a maximum of 26.3 mm/mm, whereas the image B shows a maximum of 30 mm/mm. The real case is performed under the coulomb's friction model with a friction coefficient between Aluminium and Steel of 0.61 as shown in literature. Another interesting difference between these two simulations is the material outflow, which proves to be higher under the Real case (image B).

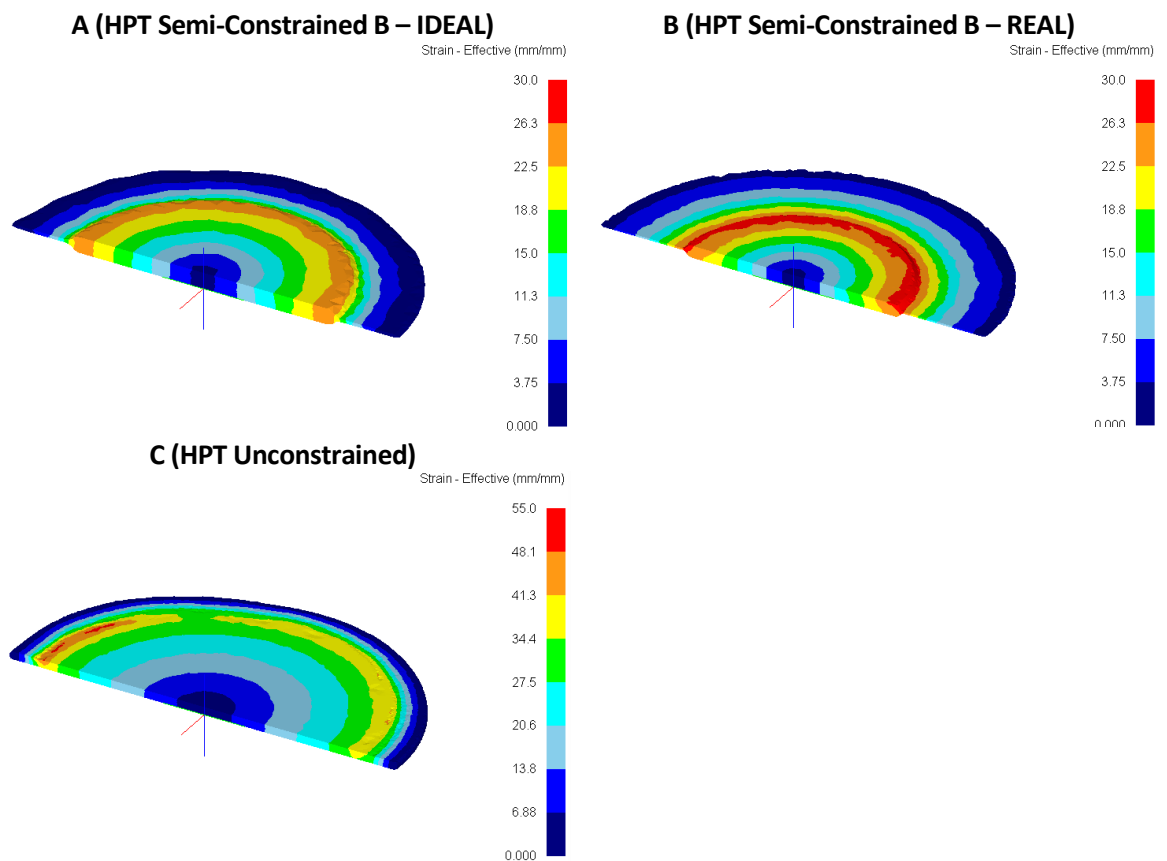


Figure 95. Strain distribution of Copper samples under different simulations at the end of the process. A illustrates the HPT semi-constrained type B simulation under ideal solicitations, B illustrates the HPT semi-constrained type B simulation under real solicitations and C illustrates the HPT unconstrained simulations results.

## 6.5.2. Comparison of stress evolution

### 6.5.2.1. Aluminium

In terms of stress Figure 96 shows that the load imposed to obtain the aimed pressure is correct, showing values of around 1.25 GPa in image A, around 6 GPa in image B, 6 GPa image C, 3 GPa for image D and 30 GPa for image E (which is a very large value unattainable in most of the cases).

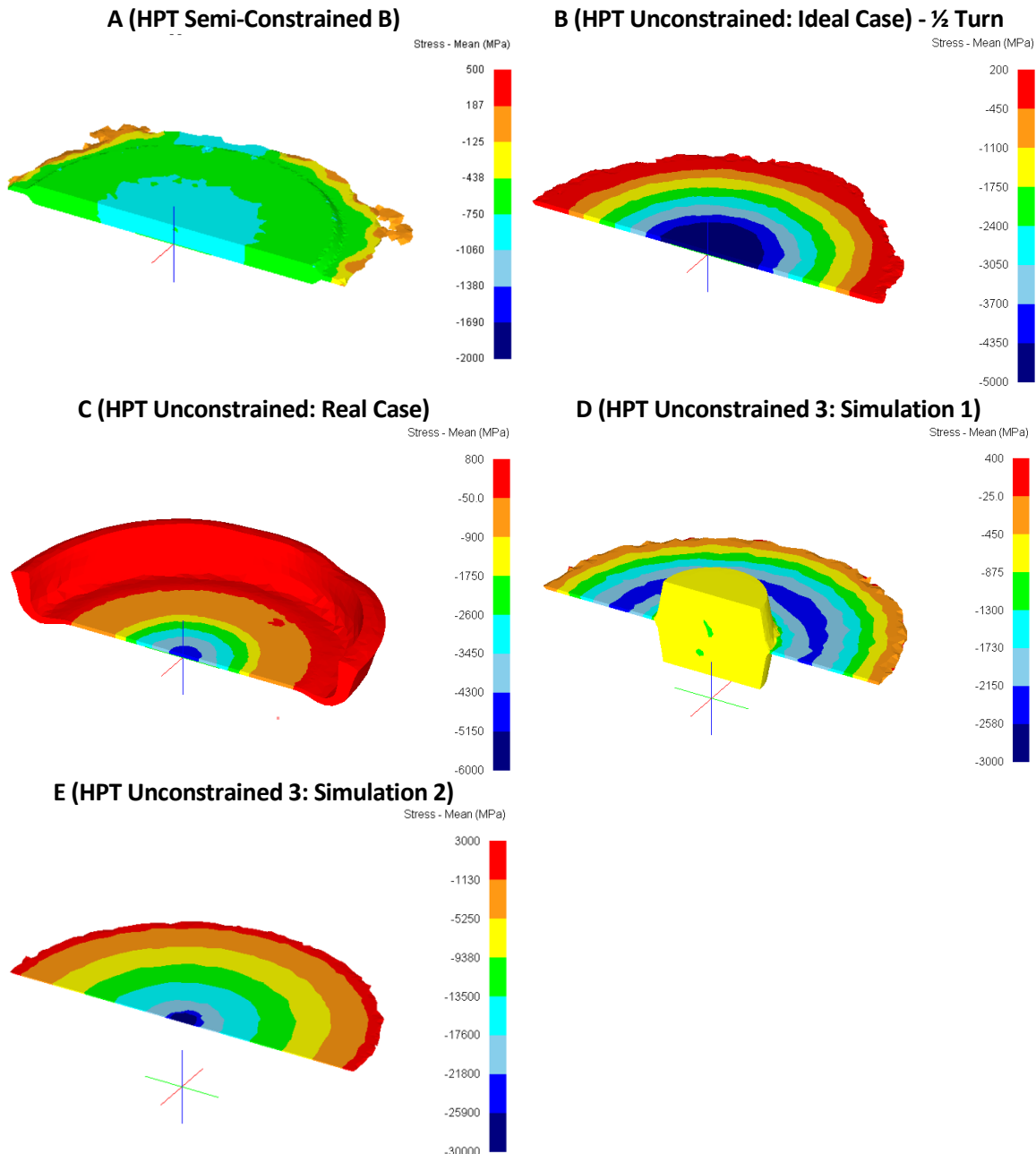


Figure 96. Stress distribution of Aluminium samples under different simulations at the end of the process. A illustrates the HPT semi-constrained type B simulation under ideal solicitations, B illustrates the HPT unconstrained simulation under ideal solicitations, C illustrates the HPT unconstrained simulation under real solicitations, D and E illustrates the HPT unconstrained simulation under case 3 simulation set; pressure and torsion applied at the same time.

These values are due to the compression loads of the dies over the sample and due to the shear forces, which taking in account the deformation and outflows, gives the different pattern. As it can be seen, the zone with the highest compression is normally located at the centre except for the image D, which is a special case where the stress distribution locates the maximum pressure in a range of 7-10 mm around the sample. The highest compression area is normally located at the centre as it is the one which must withstand all the surface equi-axial loads as long as it is the zone with less material outflow and the one with less torsion due to the radius. Under ideal circumstances, as shown in Pre-processor study, the stress distribution should be equal.

### 6.5.2.2. Copper

Copper samples simulations stress distribution (Figure 97) shows the main difference between the real case and the ideal one. Under ideal circumstances, the stress distribution is homogenous, while under real experiments the stress differs from the centre to the borders as image A and B show.

It can be seen that the loads are the established ones, 1.25 GPa compressive load for A and B and 6.0 GPa for C.

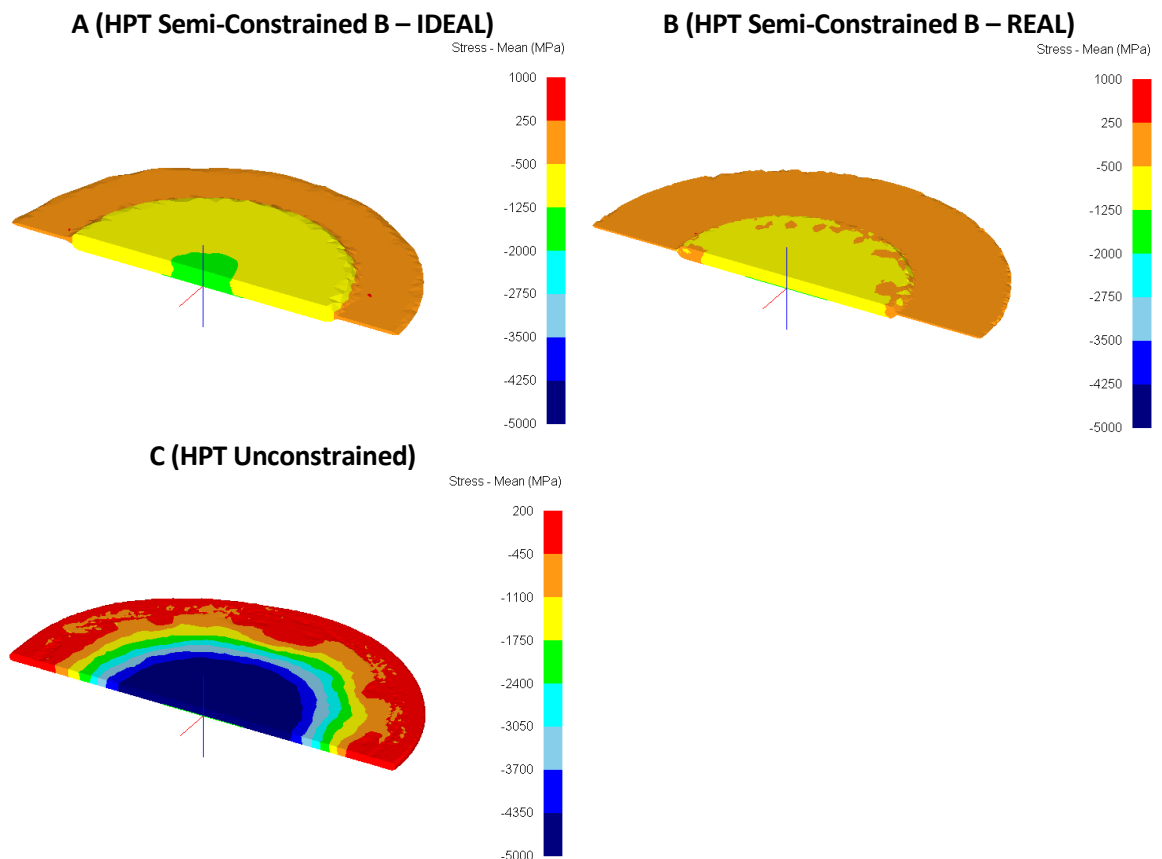


Figure 97. Stress distribution of Copper samples under different simulations at the end of the process. A illustrates the HPT semi-constrained type B simulation under ideal solicitations, B illustrates the HPT semi-constrained type B simulation under real solicitations and C illustrates the HPT unconstrained simulations results.

The image C distribution shows a more homogenous stress distribution at the centre than the one shown at Figure 96.B, this might be strongly related to the elasticity modulus of the materials.

### 6.5.3. Comparison of torque evolution

#### 6.5.3.1. Aluminium and Copper

Comparing the torque evolution along the time under the angular speed of 1 RPM (60 seconds equals one turn) one can clearly see that copper requires a higher torque for similar simulations (with the same solicitations) than Aluminium 1100. That is due to the fact that to deform the material the shear forces must overcome the internal forces of the material itself, characterised by the Young Modulus (or elastic modulus). As copper modulus is higher than Aluminium, these results were expected from the beginning.

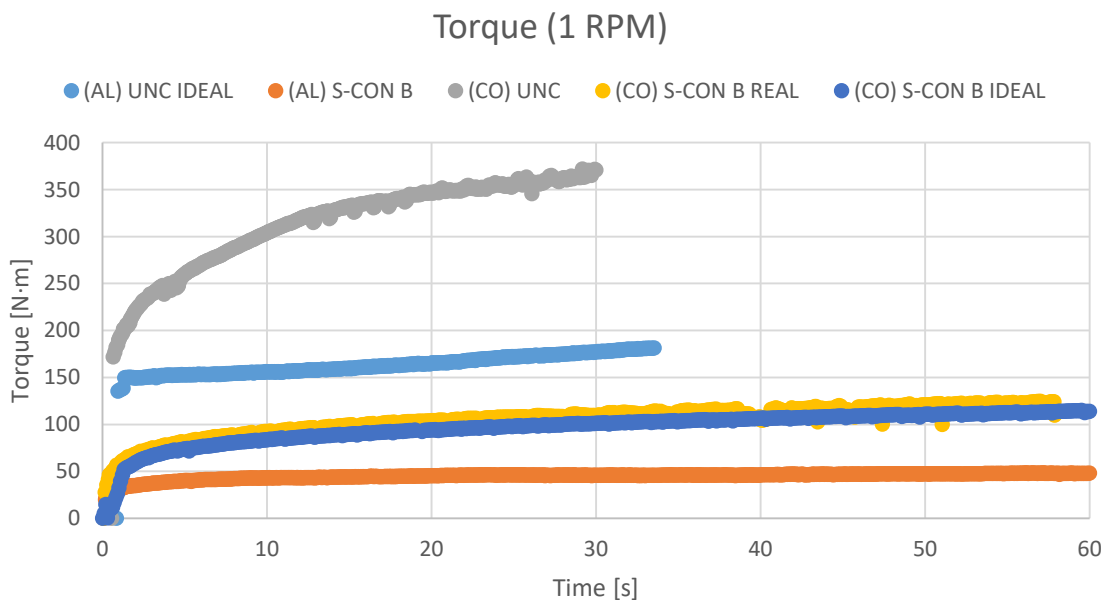


Figure 98. Torque evolution as a function of time for the different simulation cases under 1 RPM angular speed. (AL) stand for Aluminium 1100 sample and (CO) stands for Copper sample. UNC stands for Unconstrained, while S-CON B stands for Semi-Constrained type B HPT simulations.

It is interesting to observe that under all the simulations solicitations, a saturation point where the torque remains almost constant is observed for both materials. One must be aware as well to the fact that the semi-constraint type B case for Aluminium and Copper under 1.25 GPa pressure shows a similar and very early saturation at a very low torque, while under the 6.00 GPa unconstrained simulations the Aluminium material shows an already saturated material from almost the very beginning of the torsion process, with a huge jump from 0 to 150 N·m for the first torsion, probably due to the fact that the twisted movement of the die must overcome the inner forces of the sample material to start deforming.

On the other hand, copper unconstraint simulation under 6.00 GPa shows a late saturation point around half turn at a very high value ( $\sim 375 \text{ N}\cdot\text{m}$ ) comparing to Aluminium, once again due to the different needed stress to deform.

Given the extracted results an assuming a 1.5 security coefficient, a 600 N·m torque would be enough for an HPT machine in order to achieve the desired results.

The values obtained for the torque after the presented simulations (HPT Cases 1, 2 and 3) are in accordance with literature (Halloumi, Busquet, and Descartes 2014; Ivanisenko et al. 2016; Ruslan Z. Valiev, Zhilyaev, and Langdon 2013; Figueiredo, Cetlin, and Langdon 2011) in terms of values, order of magnitude, needed torque along turns and plot distribution, which motivates the acceptance of the results and their corroboration under empirical experimentations.

## 7. Multi-Directional Forging (MDF)

### 7.1. Introduction and previous works

The present section is related with SPD processes as the previous techniques, but is a continuation or better an extension of an already presented and approved master thesis developed in the same laboratory. The previous work (Torres Maldonado and Cadena Hernández 2017) was based on a new development on a SPD technique, the multi-axial forging, as presented in the section Multidirectional Forging (MDF). The thesis developed very good experimental results, in very much accordance with the simulations performed on a FEM code. Even though the project was done, multiple projects following the work of Torres Maldonado and Cadena Hernández under the supervision of PhD. Zhilyaev and Professor Cabrera have been continued. As such continuation, a thermal analysis during the process forging was performed showing interesting results, which motivated a simulation analysis to comprehend the behaviour during the process itself, as it will be shown during the next sections.

### 7.2. Case Study: Thermal Simulation

#### 7.2.1.1. Geometrical Model

The geometrical model is exactly the same as used in the mechanical analysis performed by Torres Maldonado and Cadena Hernández to determine the amount of strain, stress and stress on dies, load, etc...

The model consists of 4 dies parts; the upper and lower die and 2 walls that block the flow of the material. All of them consist of AISI H13 Tool Steel. On the other hand, the sample is just an aluminium cylinder, which fits in the cavity between dies.

##### 7.2.1.1.1 Sample

The sample is an aluminium rod of 105 mm length and 20mm diameter, which is introduced between dies with the purpose to be deformed multiple times.

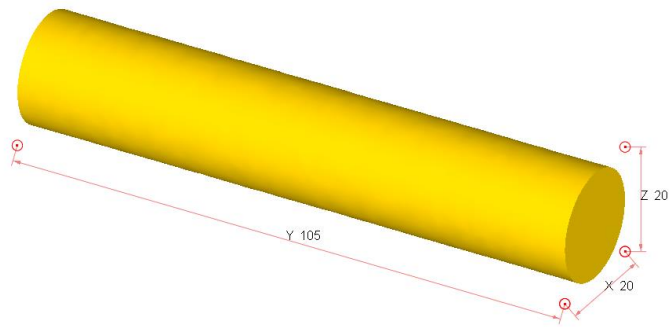


Figure 99. Sample for the MDF Thermal simulation

#### 7.2.1.1.2 Dies

The dies are two symmetrical upper and lower anvils with a particular depression form. The sole purpose of this depression is to deform the material in a way it can be deformed again when it's rotated 90° along the y-axis. The problem with a plain depression is that a deformed sample would slip and therefore recover the first deformed position. To avoid so, the researchers develop a new method to maintain the piece in the correct position, an underlying guide just in the middle of the depression and at the border of the depression. This creates a more stable guide, which allows the piece not to move or slip, while it is being pressed in the following steps.

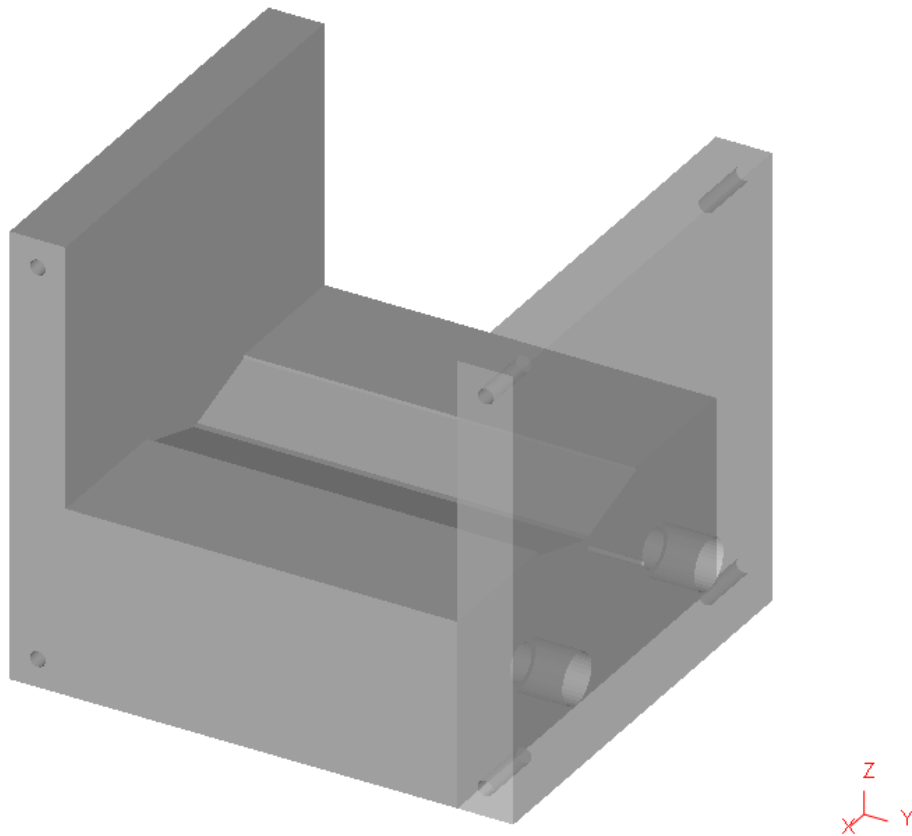


Figure 100. Dies set-up in their configuration (except top die) with the holding depression for the sample

### 7.2.1.2. Boundary Conditions; Solicitations and assumptions

In order to go through the simulation, it must be established again the solicitations and boundary conditions based on laboratory like assumptions. This time, the simulation will be performed as a thermal model, and therefore new considerations will be assumed.

- **Mechanical Assumptions:**
  - The elastic deformation of the punch and die are neglected. (Rigid condition)
  - No (material) diffusion is considered between the die, punch and sample.
  - The boundary conditions on the sample, punch and die are established just as pure mechanical, thermal and time dependant (Time Domain Mechanical Deformation study).
  - The full stroke will be performed in 1 second.
  - The Shear's Friction Coefficient between anvils and sample is set-up as:
    - 0.61 Shear Coefficient
- **Thermal Assumptions:**
  - The temperature is established initially as room temperature and constant (20°C).
  - The thermal parameters of Aluminium are assumed as:
    - Thermal Conductivity :  $180.195 \text{ W} \cdot \text{m}^{-1} \cdot \text{K}^{-1}$  (constant)
    - Heat Capacity :  $2.43328 \text{ J} \cdot \text{Kg}^{-1} \cdot \text{°C}^{-1}$  (constant)
    - Emissivity : 0.7 (constant)
  - The thermal parameters of AISI H-13
    - Thermal Conductivity : Function of temperature
    - Heat Capacity : Function of temperature
    - Emissivity : 0.7 (constant)
  - Heat Transfer Coefficient between Aluminium and AISI H-13
    - Constant and set as  $20 \frac{\text{N}}{\text{mm} \cdot \text{s} \cdot \text{°C}}$

No boundary conditions were set up for the sample, letting it flow in each and every direction without any constraints (understanding that the punch and die are geometrical constraints by themselves).

The constitutive equation for flow stress assures that the material maintains a homogenous structure following an elastic-plastic deformation; ruled by the following equation:

$$\bar{\sigma} = c \cdot \bar{\epsilon}^n \cdot \dot{\bar{\epsilon}}^m + y \quad (\text{Eq. 7.1})$$

This equation has been chosen due to maintain the consistency with the previous work on the subject.



### 7.2.1.3. External Loads and Efforts; Thermal evolution

The external loads will be exerted by a mechanical press attached on the upper die with a 1mm/sec die stroke set-up that will press until the upper and lower die touch (full stroke).

The thermal evolution will be studied along the pressure process and along the time that takes until the system is cooled.

### 7.2.1.4. Mesh

In order to perform the thermal evolution, the dies and the sample must be meshed. As it is as important the heat evolution inside the work piece as it is inside the dies, the same meshing size has been determined for all of them. After several studies, an around 30.000 elements mesh per piece was determined as a good amount for reaching good results in an acceptable time.

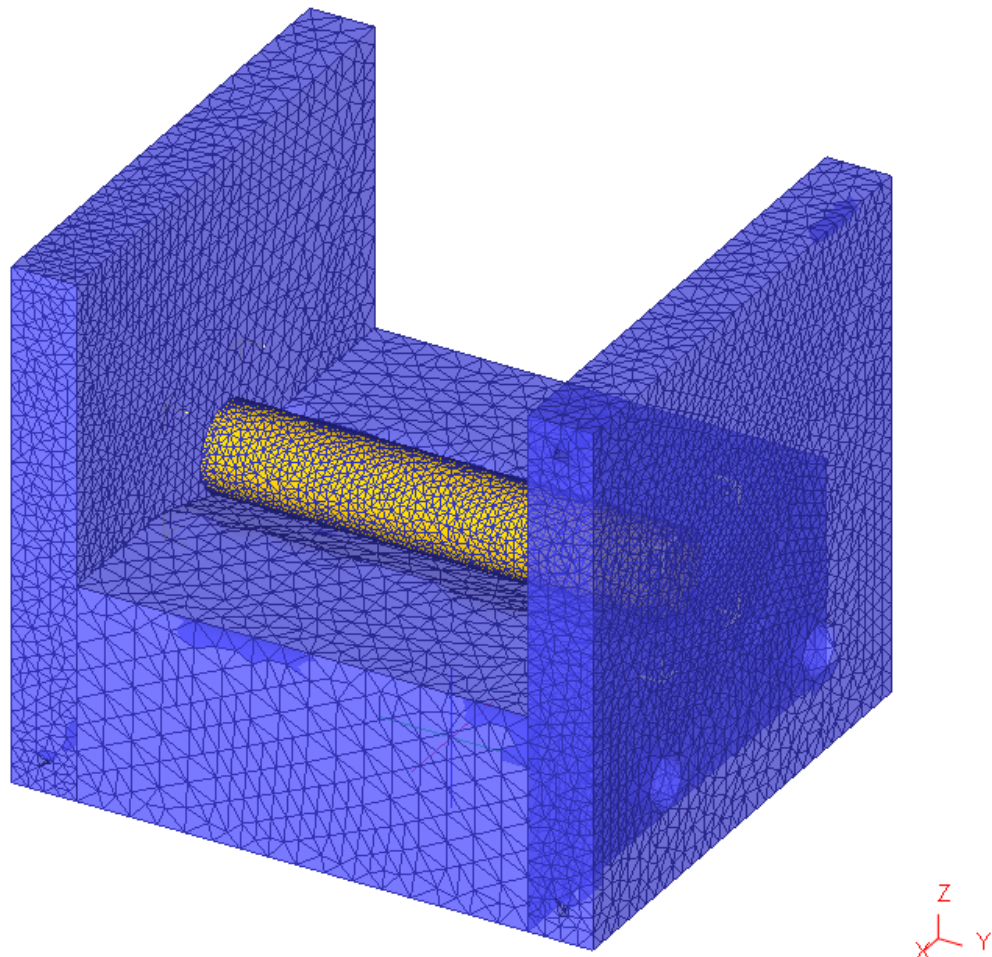


Figure 101. Mesh applied to the dies and sample. The amount of elements is approximately the same.

## 7.3. Results for Aluminium sample

### 7.3.1. Short Term Evolution (Sample heating)

The temperature distribution along the rod just at the maximum shows the same distribution as the stress or strain distribution, which can be seen in the Figure 102. A possible explanation might be that the temperature changes (or heat generation) is due to the mechanical plastically deformations performed in the material, which are correlated with the most strained parts.

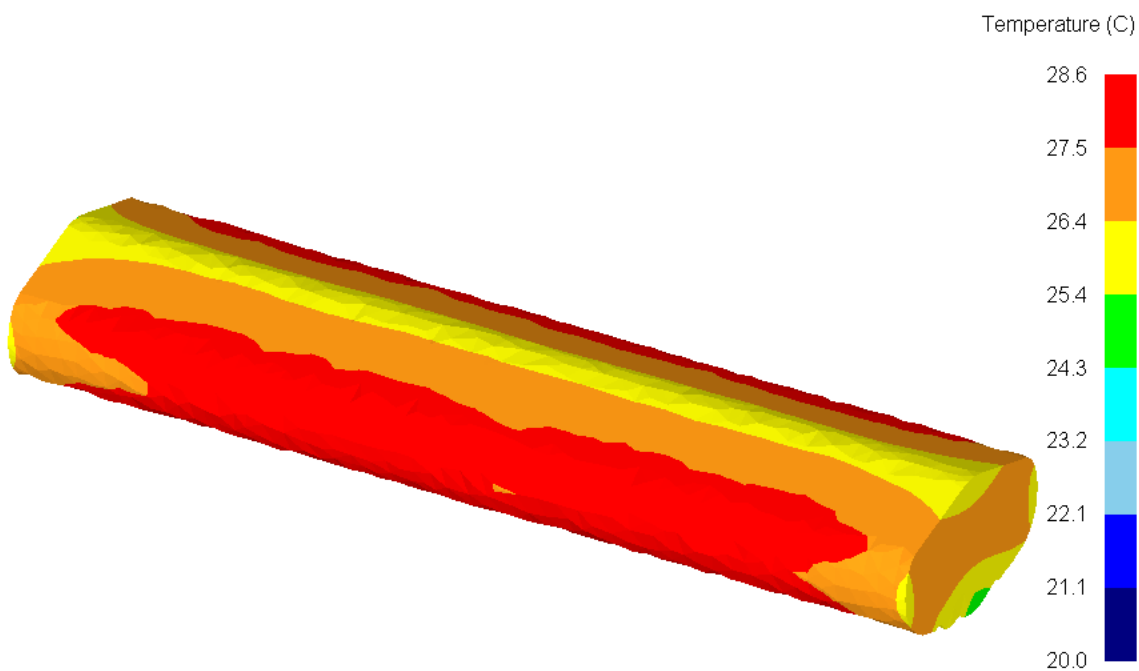


Figure 102. Temperature distribution along the sample once forged for a whole stroke

As it can be seen, the temperature evolution is of 8.6 °C from the initially 20 °C laboratory temperature set. This increment is quite dependant of the compression time, set as 1 second during the first forging cycle.

On the early stages of the simulation, between the first time that the upper anvil and the second that it takes to put it down till the limit, no significant changes are observed in the dies, just at the sample as it has been already discussed. The die does not show any further changes as the heat flux needs some time to flow along the dies as it can be seen in Figure 103.

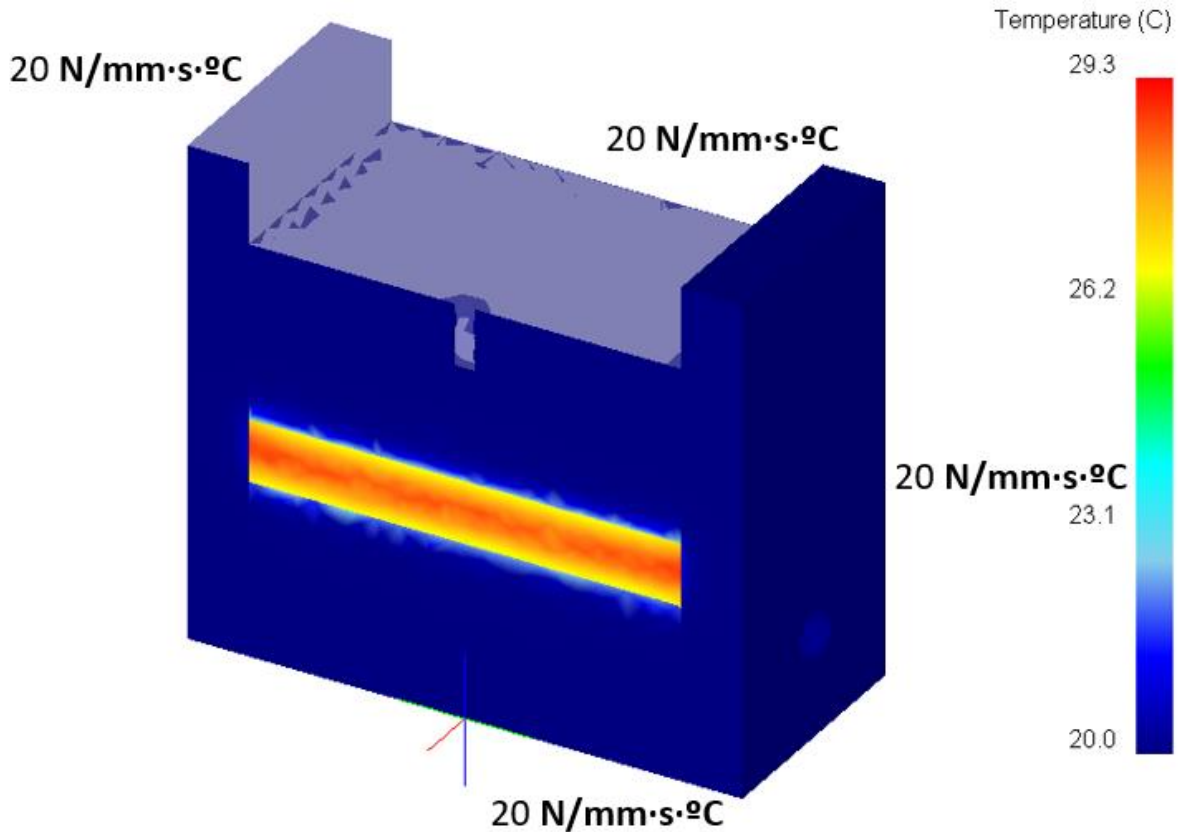


Figure 103. Temperatures changes at the end of the first cycle compression in the sample and dies. All dies are set up as  $20 \text{ N}\cdot\text{mm}^{-1}\cdot\text{s}^{-1}\cdot\text{°C}^{-1}$  heat transference between sample (Aluminium) and dies (AISI H13)

An actual evolution of the temperature distribution can be seen in figures A-F in Figure 104 and Figure 105.

The first set of figures shows the temperature distribution along the sample and dies under a range of temperature from  $20 \text{ °C}$  to  $28 \text{ °C}$  and along time within a difference between pictures of 1.5 seconds. It can be seen that during the first instances (A and B) the temperature in the rod reaches  $28 \text{ °C}$ , whereas the temperature changes inside the dies are still very low and centralize in the specific contact areas between sample and walls. It can be seen in picture C to D a drastic temperature drop inside the sample in barely 5 seconds after compressing ends, it can be assumed that the heat is flowing to the dies. It can be established that the temperature drop is due to the heat flow between dies and the aluminium rod. Finally, the end of the simulation shows a slow decreasing of the temperature, which might be due to low thermal difference compared with previous situations.

It is expected eventually to disperse the heat to the exterior due to a thermal exchange going back to the initial room temperature.

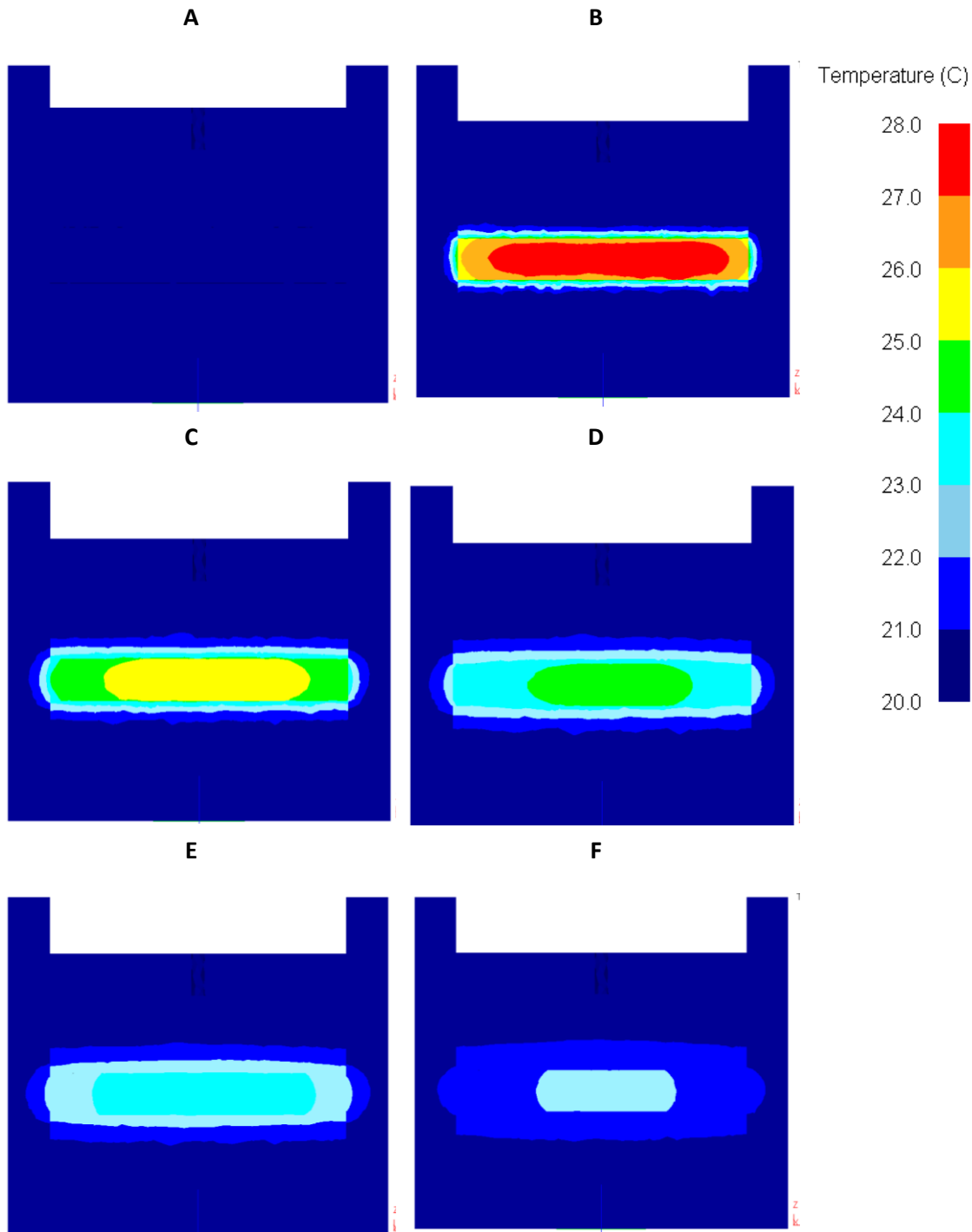


Figure 104. Thermal evolution along time from the MDF simulation with an Aluminium 1100 sample rod and Tool Steel dies. From A to E there is an instant capture of temperature distribution with a 1.5 seconds between them (1.5s; 3.0s; 4.5s; 6s; 7.5s), fixing A as the first contact between the upper anvil and the sample. Figure F shows the temperature distribution at 11 seconds of figure A.

On the other hand, in the second set of simulations the sample has been avoided for clarity reasons, as the new range is set between 20 °C and 22 °C and it will appear all at maximum colour. Along A to F a constant evolution inexorably from the sample to the outside is noticed, where the

temperature is set as 20 °C (room temperature). It can be seen that the maximum temperature that reaches the outside of the dies is 21 °C, which is exactly the 1°C calculated in a parallel project that it's been developed right now in the PROCOMAME laboratory.

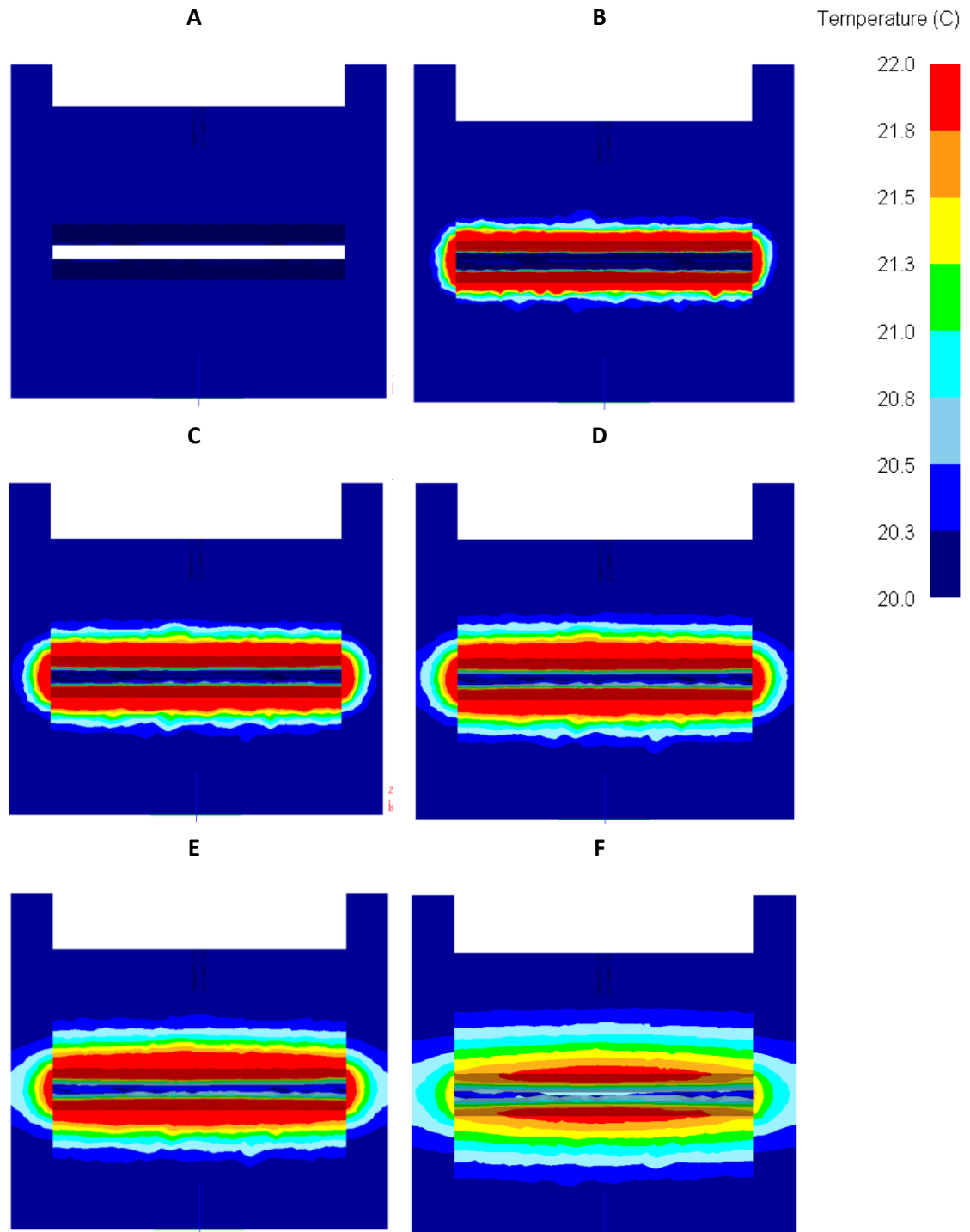


Figure 105. Thermal evolution along time from the MDF simulation with an Aluminium 1100 sample rod (not showed) and Tool Steel dies. From A to E there is an instant capture of temperature distribution with a 1.5 seconds between them (1.5s ; 3.0s; 4.5s; 6s; 7.5s), fixing A as the first contact between the upper anvil and the sample. Figure F shows the temperature distribution at 11 seconds of figure A. The scale has been set from 20 minimum to 22 maximum to better observe evolution in the dies.



## Conclusion

Along the following project it has been assured that the obtained results follow the theoretical equations under idealistic cases and that the simulations under more realistic conditions follow experimental validated data from literature.

It has been successfully studied as well the evolution of the pre-processor mesh and re-meshing for the FEM code software to obtain the most accurate data with minimums losses.

Under more specific case simulations, the results of HPT Unconstrained and HPT semi-constrained type B severe plastic deformation have been studied under different solicitations. The results show that the Aluminium 1100 sample needs normally less torque than pure Copper and the load to press the material is higher. It has been shown as well that Copper reaches saturation later than Aluminium. The obtained data follows accurately the curves obtained in various experimentations found along literature, which validates the good results of the simulations.

The maximum value of torque obtained is around 400 N·m, so a value up to 600 N·m would have a 1.5 security coefficient and would be enough for a mechanical screw machine to perform the HPT.

In terms of Multi-Directional Forging, the thermal simulations analysis shows the heat flux and thermal evolution along the dies and sample under the experimental conditions performed in the laboratories. These results helps to comprehend the thermal distribution along time of the process to better understand the dispersion of heat.





## Sources

- ASM International Handbook, Volume 2. 1990. *Properties and Selection: Nonferrous Alloys and Special-Purpose Materials. ASM Metals Handbook*. Vol. 2. doi:10.1016/S0026-0576(03)90166-8.
- Autodesk. 2017. "Autodesk Inventor - Overview." <https://www.autodesk.com/products/inventor/overview>.
- Azushima, A., R. Kopp, A. Korhonen, D. Y. Yang, F. Micari, G. D. Lahoti, P. Groche, et al. 2008. "Severe Plastic Deformation (SPD) Processes for Metals." *CIRP Annals - Manufacturing Technology* 57 (2): 716–35. doi:10.1016/j.cirp.2008.09.005.
- Beer, F P, and E R Johnston. 1988. *Vector Mechanics for Engineers - Statics and Dynamics*. McGraw-Hill, New York. Vol. 5. doi:10.1017/CBO9781107415324.004.
- CALLISTER, WILLIAM D. 2009. *Introduccion a La Ciencia E Ingenieria De Los Materiales*.
- COMSOL. 2017. "Detailed Explanation of The Finite Element Method (FEM)." <https://www.comsol.es/multiphysics/finite-element-method>.
- EngineeringToolBox. 2017. "Friction and Friction Coefficients." Accessed December 10. [https://www.engineeringtoolbox.com/friction-coefficients-d\\_778.html](https://www.engineeringtoolbox.com/friction-coefficients-d_778.html).
- Erickson, Jeff. 2012. "Theoretical Advances in Hexahedral Mesh Generation."
- Figueiredo, Roberto B., Paulo R. Cetlin, and Terence G. Langdon. 2011. "Using Finite Element Modeling to Examine the Flow Processes in Quasi-Constrained High-Pressure Torsion." *Materials Science and Engineering A* 528 (28). Elsevier B.V.: 8198–8204. doi:10.1016/j.msea.2011.07.040.
- Halloumi, A, M Busquet, and S Descartes. 2014. "Parametric Study of Unconstrained High-Pressure Torsion- Finite Element Analysis." doi:10.1088/1757-899X/63/1/012036.
- Henry, S.D., B.R. Sanders, N. Hrivnak, J.A. Kinson, and W.W. Scott. 2001. *ASM Specialty Handbook: Copper and Copper Alloys*. ASM International. doi:10.1097/00000433-198206000-00020.
- Hutton, David. 2005. "Fundamentals of Finite Element Analysis."
- Ivanisenko, Yu, R. Kulagin, V. Fedorov, A. Mazilkin, T. Scherer, B. Baretzky, and H. Hahn. 2016. "High Pressure Torsion Extrusion as a New Severe Plastic Deformation Process." *Materials Science and Engineering A* 664. Elsevier: 247–56. doi:10.1016/j.msea.2016.04.008.
- Joun, M. S., H. G. Moon, I. S. Choi, M. C. Lee, and B. Y. Jun. 2009. "Effects of Friction Laws on Metal Forming Processes." *Tribology International* 42 (2): 311–19. doi:10.1016/j.triboint.2008.06.012.
- Miura, Hiromi, Wataru Nakamura, and Masakazu Kobayashi. 2014. "Room-Temperature Multi-Directional Forging of AZ80Mg Alloy to Induce Ultrafine Grained Structure and Specific Mechanical Properties." *Procedia Engineering* 81 (October). Elsevier B.V.: 534–39. doi:10.1016/j.proeng.2014.10.035.

- Pedersen, Ketill O., Ida Westermann, Trond Furu, Tore B??rvik, and Odd Sture Hopperstad. 2015. "Influence of Microstructure on Work-Hardening and Ductile Fracture of Aluminium Alloys." *Materials and Design* 70. Elsevier Ltd: 31–44. doi:10.1016/j.matdes.2014.12.035.
- Scientific Forming Technologies Corporation (SFTC). 2011. "Integrated 2D3D System Manual" 0.
- SFTC. 2017. "Deform." <http://www.deform.com/>.
- Stráská, Jitka, Josef Strásky, Peter Minárik, Miloš Janeček, and Robert Kral. 2016. "Microstructure Evolution in Ultrafine-Grained Magnesium Alloy AZ31 Processed by Severe Plastic Deformation." In *Modern Electron Microscopy in Physical and Life Sciences*. InTech. doi:10.5772/61611.
- Torres Maldonado, Mario Javier, and Homero David Cadena Hernández. 2017. "MODELIZACIÓN DE UN PROCESO DE SEVERA DEFORMACIÓN PLÁSTICA POR FORJA MÚLTIPLE."
- Valiev, R. Z., R. K. Islamgaliev, and I. V. Alexandrov. 2000. *Bulk Nanostructured Materials from Severe Plastic Deformation. Progress in Materials Science*. Vol. 45. doi:10.1016/S0079-6425(99)00007-9.
- Valiev, Ruslan Z., Alexander P. Zhilyaev, and Terence G. Langdon. 2013. *Bulk Nanostructured Materials. Bulk Nanostructured Materials*. Hoboken, NJ: John Wiley & Sons, Inc. doi:10.1002/9781118742679.
- Weck, Olivier de, and Il Yong Kim. 2004. "Finite Element Method." *Engineering Design and Rapid Prototyping* 810: 26. [http://web.mit.edu/16.810/www/16.810\\_L4\\_CAE.pdf](http://web.mit.edu/16.810/www/16.810_L4_CAE.pdf).
- Wikipedia. 2017a. "Computer-Aided Engineering." [https://en.wikipedia.org/w/index.php?title=Computer-aided\\_engineering&oldid=795071809](https://en.wikipedia.org/w/index.php?title=Computer-aided_engineering&oldid=795071809).
- . 2017b. "Finite Element Method." [https://en.wikipedia.org/w/index.php?title=Finite\\_element\\_method&oldid=801543557](https://en.wikipedia.org/w/index.php?title=Finite_element_method&oldid=801543557).
- Xu, Shubo, Guoqun Zhao, Yiguo Luan, and Yanjin Guan. 2006. "Numerical Studies on Processing Routes and Deformation Mechanism of Multi-Pass Equal Channel Angular Pressing Processes." *Journal of Materials Processing Technology* 176 (1–3): 251–59. doi:10.1016/j.jmatprotec.2006.03.167.
- Yousefi Mehr, Vahid, Mohammad Reza Toroghinejad, and Ahmad Rezaeian. 2014. "Mechanical Properties and Microstructure Evolutions of Multilayered Al-Cu Composites Produced by Accumulative Roll Bonding Process and Subsequent Annealing." *Materials Science and Engineering A* 601 (April). Elsevier: 40–47. doi:10.1016/j.msea.2014.02.023.
- Zhilyaev, A. P., T. R. McNelley, and T. G. Langdon. 2007. "Evolution of Microstructure and Microtexture in Fcc Metals during High-Pressure Torsion." *Journal of Materials Science* 42 (5): 1517–28. doi:10.1007/s10853-006-0628-0.

**Equations:**

(Eq. 3.1)	3
(Eq. 3.2)	5
(Eq. 3.3)	5
(Eq. 3.4)	12
(Eq. 3.5)	12
(Eq. 3.6)	13
(Eq. 4.1)	16
(Eq. 4.2)	23
(Eq. 5.1)	24
(Eq. 5.2)	25
(Eq. 6.1)	33
(Eq. 6.2)	69
(Eq. 7.1)	96

**Figures:**

- Figure 1. Principle of SPD High-pressure torsion (HPT) method schema (left) and stages (right) (Azushima et al. 2008) and (Stráská et al. 2016) respectively. \_\_\_\_\_ 4
- Figure 2. Representation (schematic) of unconstrained (a) and constrained type a (b) and type b (c) HPT process. (Zhilyaev, McNelley, and Langdon 2007) \_\_\_\_\_ 5
- Figure 3. Schematic illustration of the MDF technique. The bold black arrows and  $\sigma$  indicate the forging axes and stress. (Miura, Nakamura, and Kobayashi 2014) \_\_\_\_\_ 6
- Figure 4. ECAP Schematic process and parts (Xu et al. 2006) \_\_\_\_\_ 7
- Figure 5. Schematic representation and steps of ARB process. (Yousefi Mehr, Toroghinejad, and Rezaeian 2014) \_\_\_\_\_ 7
- Figure 6. Different Elements in function of the Space Dimension and the amount of nodes (black dots). <http://illustrations.marin.ntnu.no/structures/analysis/FEM/theory/index.html>. \_\_\_\_\_ 9
- Figure 7. Comparison of metal flow lines formed from compression of the ring with large aspect ratio and large ratio of contact region: (a) Coulomb friction's model and (b) constant shear friction model. (Joun et al. 2009) \_\_\_\_\_ 13
- Figure 8. Euler's buckling test samples. (<https://www.manufacturingguide.com/en/eulers-buckling-test>) \_\_\_\_\_ 14
- Figure 9. (left) First experiment setup with "infinite-like" anvils and (right) Second Experimental setup with "geometry-like" sample. Units are given in mm. \_\_\_\_\_ 16
- Figure 10. Strain distribution on a cylinder Work piece with Finer Grain Mesh after Ideal (no friction) compression \_\_\_\_\_ 17
- Figure 11. Strain distribution on a cylinder Work piece with Finer Grain Mesh after real compression (establishing Coulomb's friction model between sample and die). \_\_\_\_\_ 18
- Figure 12. Manual mesh with relative element size of 5,4,3 on the top surface, cylinder surface and bottom surface. \_\_\_\_\_ 18
- Figure 13. Strain distribution on a manual mesh with relative element size of 5,4,3 on the top surface, cylinder surface and bottom surface. \_\_\_\_\_ 19

Figure 14. Strain distribution on a disk Work piece with Finer Grain Mesh after Ideal (no friction) compression \_\_\_\_\_ 20

Figure 15. Manual mesh. \_\_\_\_\_ 22

Figure 16. Manual mesh with a cylinder window meshing equiaxial and with 10mm diameter. \_ 23

Figure 17. DEFORM Port-view of the sliced sample over the lower anvil depression. \_\_\_\_\_ 25

Figure 18. Strain evolution along the distance from the centre based on literature (black and white) and comparison with simulation results (colour) \_\_\_\_\_ 26

Figure 19. Total velocity comparison between literature (left) and simulation (right). \_\_\_\_\_ 27

Figure 20. Effective Strain distribution comparison between literature (left) and simulation (right). 27

Figure 21. Mean stress distribution of literature model (top left) and obtained simulation with 2.0 shear coefficient model (top right) and comparison with Coulomb's friction model with coefficients 0.5 (A), 0.6 (B) and 0.7 (C). \_\_\_\_\_ 28

Figure 22. Sample CAD model (Autodesk Inventor) with technical data. Thickness can be 1.00 mm or 0.80 mm \_\_\_\_\_ 32

Figure 23. Upper and Lower anvil dies CAD model (Autodesk Inventor) with technical data. \_\_\_\_ 32

Figure 24. Mesh example at the beginning of the Torsion simulation. The mesh is finer at the borders of the depression with an empty cylindrical mesh window. \_\_\_\_\_ 34

Figure 25. Stress distribution on a Copper sample during an HPT Semi-Constrained Type B experiment with a Shear Coefficient 2.0. 1 Turn at 1 RPM. 1 GPa. \_\_\_\_\_ 36

Figure 26. Strain distribution on a Copper sample during an HPT Semi-Constraint Type B experiment with a Shear Coefficient 2.0. 1 Turn at 1 RPM. 1 GPa. \_\_\_\_\_ 37

Figure 27. Torque evolution in function of time. Angular speed set at 1RPM. \_\_\_\_\_ 37

Figure 28. Total displacement (in mm) of the nodes and elements of the HPT semi-constrained type B copper sample simulation. \_\_\_\_\_ 38

Figure 29. Stress distribution on a Copper sample during an HPT Semi-Constrained Type B experiment with a Frictional Coefficient 0.63. 1 Turn at 1 RPM. 1 GPa. \_\_\_\_\_ 39

Figure 30. Strain distribution on a Copper sample during an HPT Semi-Constrained Type B experiment with a Frictional Coefficient 0.63. 1 Turn at 1 RPM. 1 GPa. _____	40
Figure 31. Torque evolution as a function of time along 1 turn. _____	40
Figure 32. Mesh configuration for the last step of the simulation. _____	41
Figure 33. Total nodal displacement of the aluminium semi-constraint sample at 1 turn. _____	41
Figure 34. Mean stress after 1 turn of the sample. _____	42
Figure 35. Effective Strain after 1 turn in the Aluminium 1100 sample. _____	43
Figure 36. Torque time dependence for the Aluminium 1100 sample under the semi-constrained type B HPT process for 1 turn. _____	43
Figure 37. Upper and Lower anvil dies CAD model (Autodesk Inventor) with technical data. ____	45
Figure 38. Upper and Lower anvil dies CAD model (Autodesk Inventor) with technical data. ____	46
Figure 39. Initial mesh configuration with approximately 120.000 elements with a finer element size at the outside compare to the inside _____	49
Figure 40. Mesh distribution with approximately 55.000 elements with a constant element size distribution after compression. $h = 0.3214$ mm; $d = 17.7157$ mm _____	50
Figure 41. Mesh distribution with approximately 50.000 elements with a finer element size distribution at the outside compare to the inside. _____	50
Figure 42. Total element displacement after compression. _____	51
Figure 43. Total element displacement after the torsion rate. Rear part of the sample. _____	51
Figure 44. Effective Strain distribution of the sample. _____	52
Figure 45. Effective strain distribution of the sample at half turn. _____	53
Figure 46. Plot of the Theoretical Model Equation (yellow) against the simulation data obtained (grey) evaluated at the same geometrical point. It shows the evolution of Effective Strain in function of time. _____	53
Figure 47. Mean stress distribution of the sample after compression. _____	54

Figure 48. Mean stress distribution of the sample after half turn torsion. _____	54
Figure 49. Torque as a function of time _____	55
Figure 50. Initial mesh configuration with approximately 120.000 elements with a finer element size at the outside compare to the inside _____	56
Figure 51. Mesh distribution with approximately 110.000 elements with a a finer element size at the outside compare to the inside. Manual re-meshing performed. _____	57
Figure 52. Mesh distribution with approximately 190.000 elements with a a finer element size at the outside compare to the inside after half a turn torsion. Automatic re-mesh performed by DEFORM v10 due to Mesh Windows set-up. _____	57
Figure 53. Total element displacement after compression. _____	58
Figure 54. Total element displacement after compression after half turn torsion. Rear part of the sample. _____	58
Figure 55. Effective Strain distribution of the sample after compression. _____	59
Figure 56. Effective Strain distribution of the sample after half turn Torsion of the sample. ____	59
Figure 57. Plot of the Theoretical Model Equation (yellow) against the simulation data obtained (grey) evaluated at the same geometrical point. It shows the evolution of Effective Strain in function of time. _____	60
Figure 58. Mean stress distribution after compression. _____	61
Figure 59. Mean stress distribution after half turn torsion. _____	61
Figure 60. Torque evolution along time estimated by simulation. _____	62
Figure 61. (left) Effective strain and (right) Contact points between dies and sample (left). Not full contact is shown in right figure, as the contact points is not well set-up. _____	63
Figure 62. Mesh configuration along the real HPT aluminium 1100 simulation. _____	64
Figure 63. (left) Effective strain and (right) Contact points between dies and sample (left). Not full contact is shown in right figure, as the contact points is not well set-up. _____	64

Figure 64. From A to D; evolution of effective strain for a realistic dies and coefficient model on an Aluminium 1100. A shows one quarter turn, B shows two quarters turn, C shows three quarters turn and D shows one turn. Green dots on left parts of the figures show the contact points between sample and the die (from 0 to 5mm constant radius)	65
Figure 65. From A to D; evolution of effective strain for a realistic dies and coefficient model on an Aluminium 1100. A shows one turn, B shows two turns, C shows three turns and D shows four turns. Green dots on left parts of the figures show the contact points between sample and the die (from 0 to 5mm constant radius)	66
Figure 66. Strain evolution along time of different points of the sample	67
Figure 67. Exemplary sketch received by mail with the specifications for the simulations	68
Figure 68. Second Moment of Area of a circle. (Beer and Johnston 1988)	69
Figure 69. Plot showing the function between the sample length and the amount of load to buckle.	70
Figure 70. Upper and Lower anvil for the first set of simulations.	71
Figure 71. Different lengths in function of the depression length ( $L_d$ ), total length ( $L_t$ ) and distance between die's surfaces ( $L$ )	72
Figure 72. Sample evolution for a 13mm length sample	73
Figure 73. Strain distribution at the end of the process for a 13 mm length sample.	74
Figure 74. Strain distribution at the end of the process for a 13 mm length sample.	74
Figure 75. Load as a function of the sample length (for sample length within dies of 5mm)	75
Figure 76. Torque evolution as a function of the sample length (length within dies of 5mm)	75
Figure 77. Sample evolution for a 48mm length sample	76
Figure 78. Strain distribution for a 48mm length rod with the new HPT method.	77
Figure 79. Strain distribution at the end of the process for the 48 mm length sample.	77
Figure 80. Load vs time evolution for the sample length of 48 mm sample (40 mm between dies)	78



Figure 81. Torque evolution of in function of the sample length for a 48 mm sample (40 mm between dies)	78
Figure 82. Buckling effect due to meshing effects in the 78 mm sample	79
Figure 83. Total length (Lt) and distance between die's surfaces (L) are equal under this new simulation set with no depression.	80
Figure 84. Deformation evolution at the beginning and at the end of the Aluminium 1100.	80
Figure 85. Strain distribution of the sample	81
Figure 86. Stress distribution of the sample	82
Figure 87. Load evolution as function of time.	82
Figure 88. Torque evolution as function of time.	83
Figure 89. Deformation evolution at the beginning and at the end of the Aluminium 1100.	83
Figure 90. Strain distribution of the sample at the end of the process	84
Figure 91. Stress state of the sample after the HPT case 3 process	85
Figure 92. Load and torque evolution as function of time.	85
Figure 93. Deformation of the sample (Buckling)	86
Figure 94. Strain distribution of Aluminium samples under different simulations at the end of the process. A illustrates the HPT semi-constrained type B simulation under ideal solicitations, B illustrates the HPT unconstrained simulation under ideal solicitations, C illustrates the HPT unconstrained simulation under real solicitations, D and E illustrates the HPT unconstrained simulation under case 3 simulation set; pressure and torsion applied at the same time.	88
Figure 95. Strain distribution of Copper samples under different simulations at the end of the process. A illustrates the HPT semi-constrained type B simulation under ideal solicitations, B illustrates the HPT semi-constrained type B simulation under real solicitations and C illustrates the HPT unconstrained simulations results.	89
Figure 96. Stress distribution of Aluminium samples under different simulations at the end of the process. A illustrates the HPT semi-constrained type B simulation under ideal solicitations, B illustrates the HPT unconstrained simulation under ideal solicitations, C illustrates the HPT	

unconstrained simulation under real solicitations, D and E illustrates the HPT unconstrained simulation under case 3 simulation set; pressure and torsion applied at the same time. \_\_ 90

Figure 97. Stress distribution of Copper samples under different simulations at the end of the process. A illustrates the HPT semi-constrained type B simulation under ideal solicitations, B illustrates the HPT semi-constrained type B simulation under real solicitations and C illustrates the HPT unconstrained simulations results. \_\_\_\_\_ 91

Figure 98. Torque evolution as a function of time for the different simulation cases under 1 RPM angular speed. (AL) stand for Aluminium 1100 sample and (CO) stands for Copper sample. UNC stands for Unconstrained, while S-CON B stands for Semi-Constrained type B HPT simulations. \_\_\_\_\_ 92

Figure 99. Sample for the MDF Thermal simulation \_\_\_\_\_ 95

Figure 100. Dies set-up in their configuration (except top die) with the holding depression for the sample \_\_\_\_\_ 95

Figure 101. Mesh applied to the dies and sample. The amount of elements is approximately the same. \_\_\_\_\_ 97

Figure 102. Temperature distribution along the sample once forged for a whole stroke \_\_\_\_\_ 98

Figure 103. Temperatures changes at the end of the first cycle compression in the sample and dies. All dies are set up as  $20 \text{ N}\cdot\text{mm}^{-1}\cdot\text{s}^{-1}\cdot\text{°C}^{-1}$  heat transference between sample (Aluminium) and dies (AISI H13) \_\_\_\_\_ 99

Figure 104. Thermal evolution along time from the MDF simulation with an Aluminium 1100 sample rod and Tool Steel dies. From A to E there is an instant capture of temperature distribution with a 1.5 seconds between them (1.5s ; 3.0s; 4.5s; 6s; 7.5s), fixing A as the first contact between the upper anvil and the sample. Figure F shows the temperature distribution at 11 seconds of figure A. \_\_\_\_\_ 100

Figure 105. Thermal evolution along time from the MDF simulation with an Aluminium 1100 sample rod (not showed) and Tool Steel dies. From A to E there is an instant capture of temperature distribution with a 1.5 seconds between them (1.5s ; 3.0s; 4.5s; 6s; 7.5s), fixing A as the first contact between the upper anvil and the sample. Figure F shows the temperature distribution at 11 seconds of figure A. The scale has been set from 20 minimum to 22 maximum to better observe evolution in the dies. \_\_\_\_\_ 101

**Tables:**

Table 1. Column Effective Length Factor (K) in function of the constraint condition. (*free to move laterally) _____	14
Table 2. Mesh variances under different cases. Experiment 1: Ideal case. _____	17
Table 3. Mesh variances under different cases. Experiment 2: Sample like Geometry _____	20
Table 4. Element loss under different cases under different re-meshing functions _____	22
Table 5. Selected discreet variables, units and values for the following simulations. _____	29
Table 6. Material properties for the samples and dies and DEFORM v10 integrated material library equivalent. _____	30
Table 7. Buckling parameters for the HPT case 3 simulation _____	69

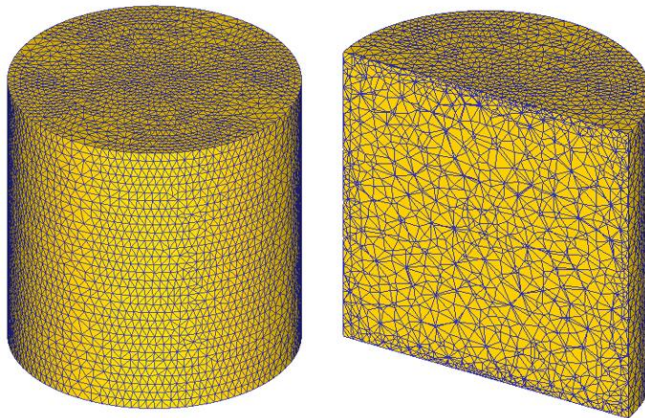


## Annex A. Mesh and re-mesh Study

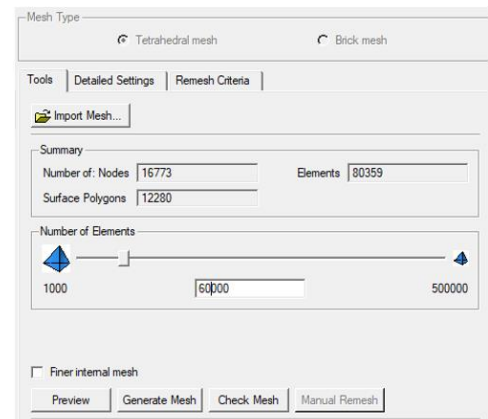
### A1. Mesh Study 1

## Mesh Generation; Tools

60.000 Elements



Without finer internal mesh

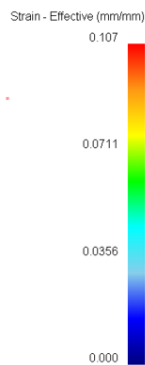
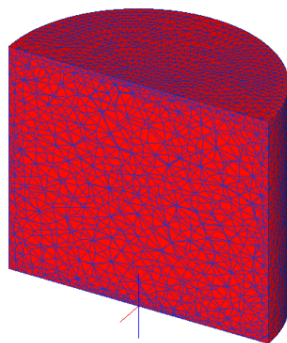


## FEM Simulation Results

Coulomb Friction : 0

$l_0 = 10\text{mm}$  ,  $l = 9\text{mm}$

DEFORM\_TEST - Compression : 1 s [step: 100]



FEM Final Strain: 0.1055

Theoretical Strain : 0.1054

Error : 0.13%

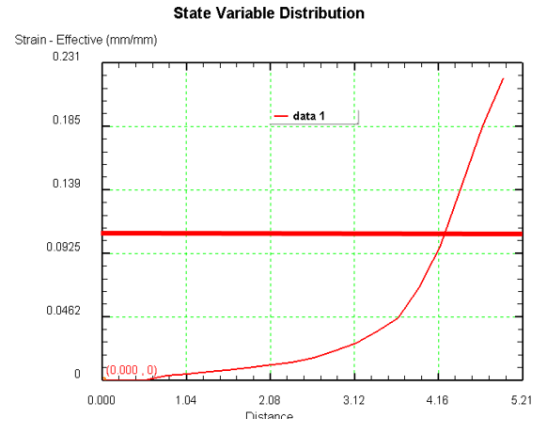
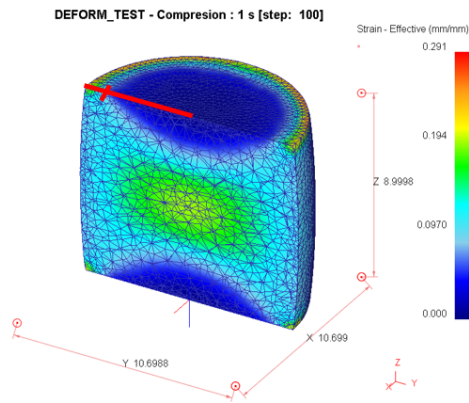
$$\varepsilon = \ln\left(\frac{l_0}{l}\right)$$

## FEM Simulation Results (No Remesh)

Coulomb Friction : 1.0  
 $l_0 = 10\text{mm}$ ,  $l = 9\text{mm}$

Theoretical Strain : 0.1054

$$\varepsilon = \ln\left(\frac{l_0}{l}\right)$$

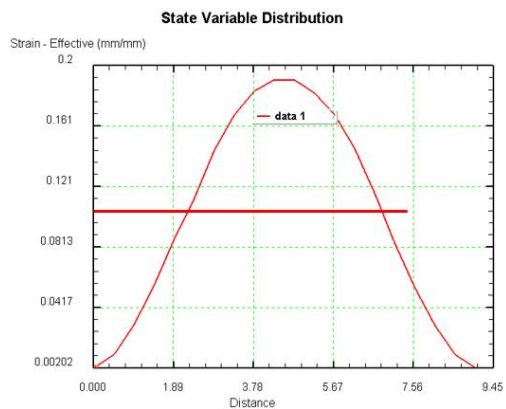
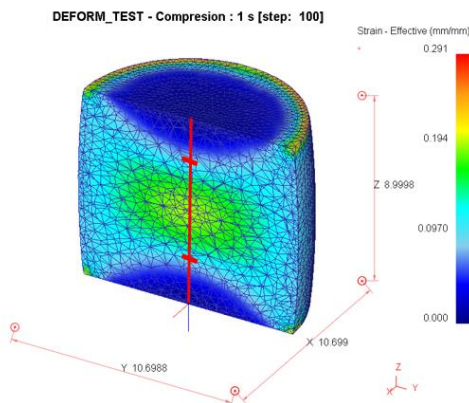


## FEM Simulation Results (No Remesh)

Coulomb Friction : 1.0  
 $l_0 = 10\text{mm}$ ,  $l = 9\text{mm}$

Theoretical Strain : 0.1054

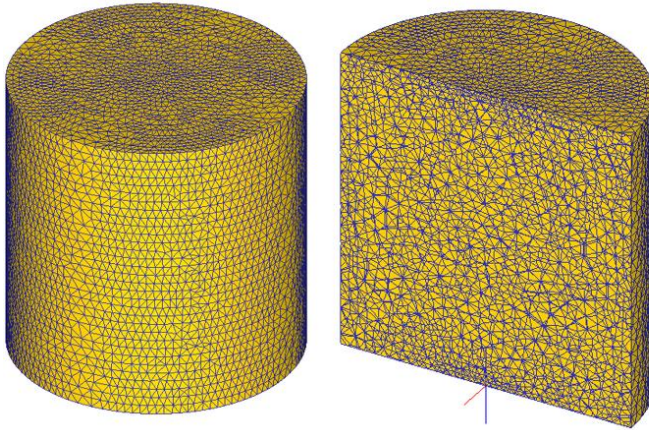
$$\varepsilon = \ln\left(\frac{l_0}{l}\right)$$



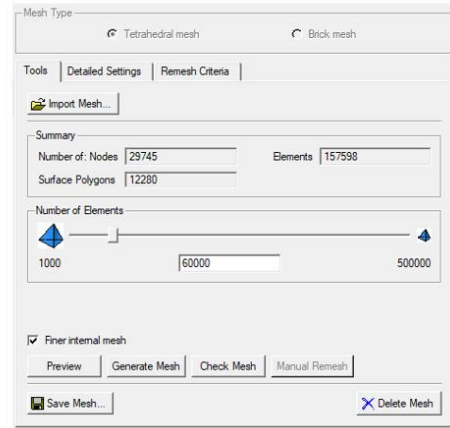
## A2. Mesh Study 2

# Mesh Generation; Tools

60.000 Elements



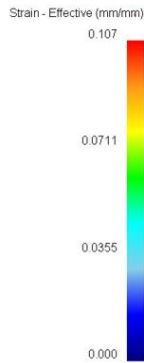
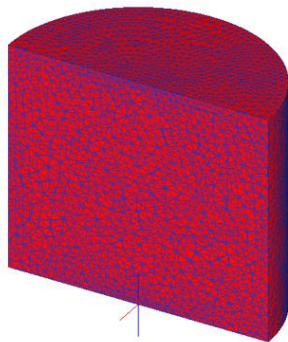
With finer internal mesh



## FEM Simulation Results (No Remesh)

Coulomb Friction : 0  
 $l_0 = 10mm, l = 9mm$

DEFORM\_TEST - Compression : 1 s [step: 100]



FEM Final Strain: 0.1055  
 Theoretical Strain : 0.1054  
 Error : 0.13%

$$\epsilon = \ln\left(\frac{l_0}{l}\right)$$



NOTE: SAME RESULTS AS PREVIOUS SIMULATION

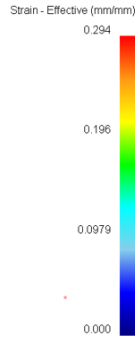
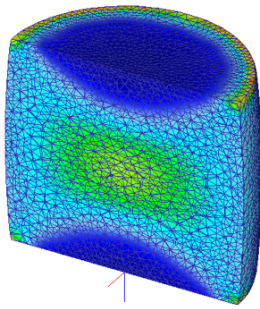
# FEM Simulation Results (No Remesh)

**Coulomb Friction : 1.0**  
 $l_0 = 10mm, l = 9mm$

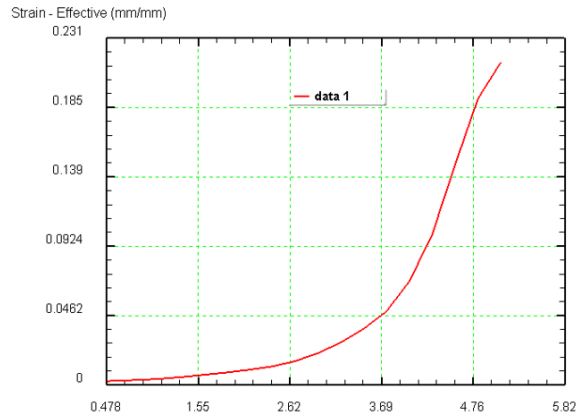
**Theoretical Strain : 0.1054**

$$\varepsilon = \ln\left(\frac{l_0}{l}\right)$$

DEFORM\_TEST - Compression : 1 s [step: 100]



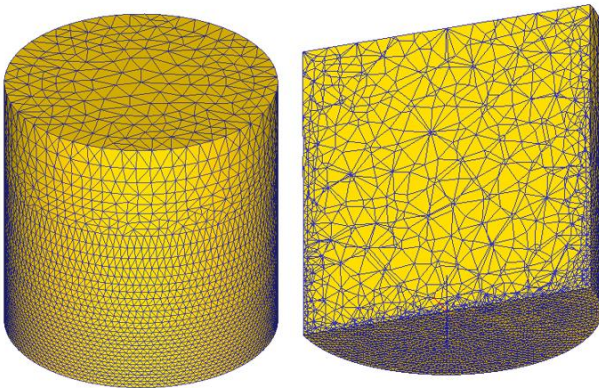
State Variable Distribution



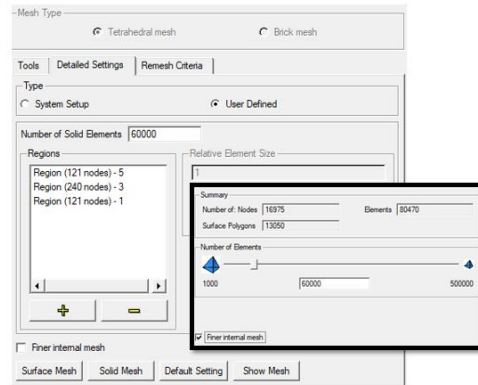
## A3. Mesh Study 3

# Mesh Generation; Detailed Settings

**60.000 Elements (5,3,1)**



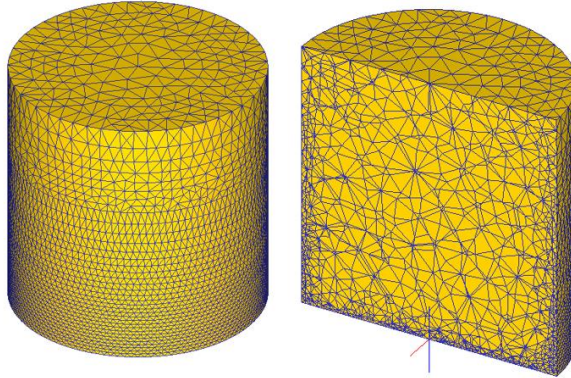
**User Defined Surface Mesh  
 (With Finer Internal Mesh)**



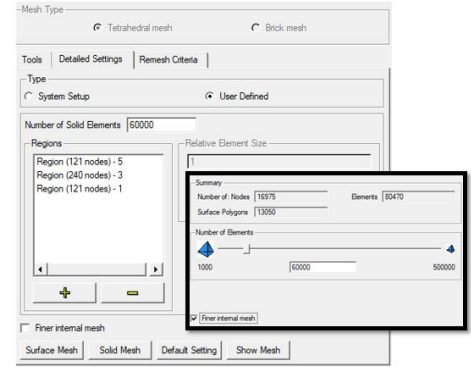


## Mesh Generation; Detailed Settings

60.000 Elements (5,3,1)



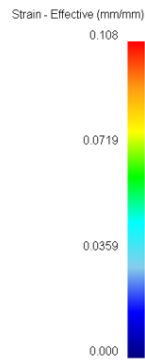
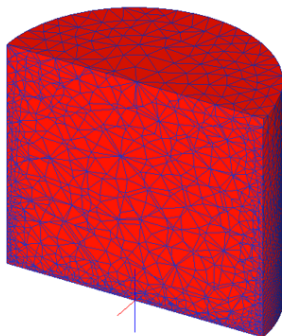
User Defined Surface Mesh  
(With Finer Internal Mesh)



## FEM Simulation Results (No Remesh)

Coulomb Friction : 0  
 $l_0 = 10\text{mm}$  ,  $l = 9\text{mm}$

DEFORM\_TEST - Compression : 1 s [step: 100]



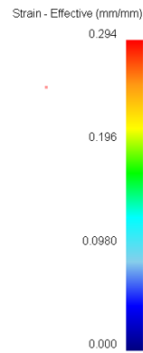
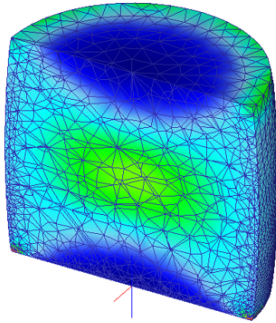
FEM Final Strain: 0.1055  
Theoretical Strain : 0.1054  
Error : 0.13%

$$\varepsilon = \ln\left(\frac{l_0}{l}\right)$$

## FEM Simulation Results (No Remesh)

Coulomb Friction : 0  
 $l_0 = 10\text{mm}$  ,  $l = 9\text{mm}$

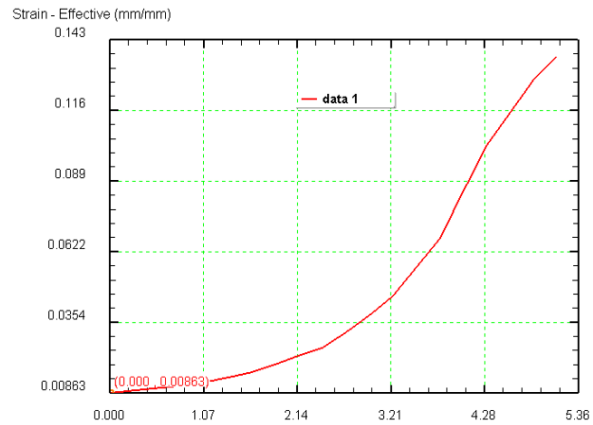
DEFORM\_TEST - Compression : 1 s [step: 100]



Theoretical Strain : 0.1054

$$\varepsilon = \ln\left(\frac{l_0}{l}\right)$$

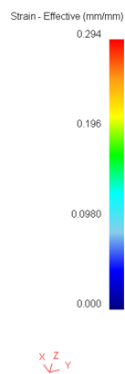
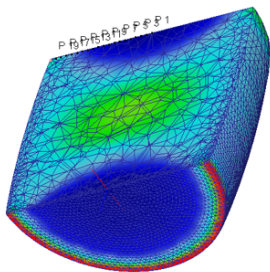
State Variable Distribution



## FEM Simulation Results (No Remesh)

Coulomb Friction : 0  
 $l_0 = 10\text{mm}$  ,  $l = 9\text{mm}$

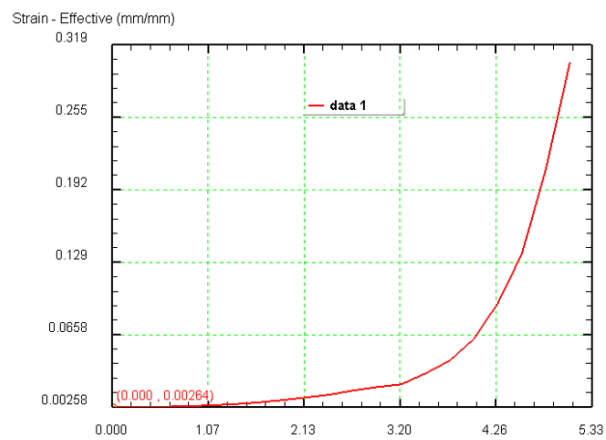
DEFORM\_TEST - Compression : 1 s [step: 100]



Theoretical Strain : 0.1054

$$\varepsilon = \ln\left(\frac{l_0}{l}\right)$$

State Variable Distribution



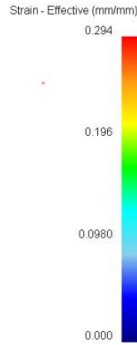
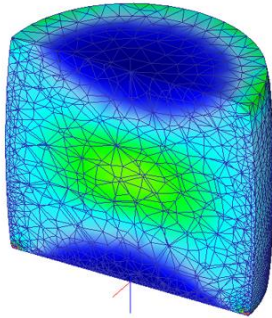
# FEM Simulation Results (No Remesh)

**Coulomb Friction : 0**  
 $l_0 = 10\text{mm}, l = 9\text{mm}$

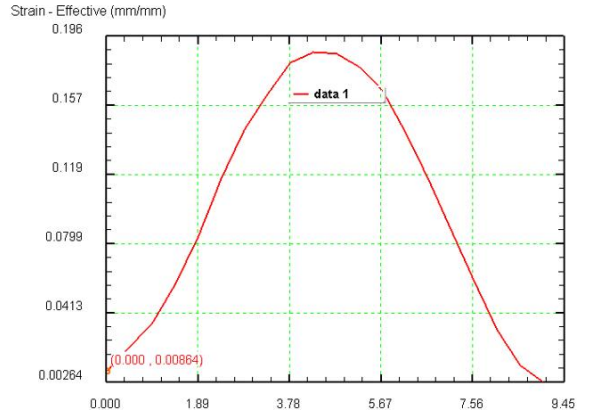
**Theoretical Strain : 0.1054**

$$\varepsilon = \ln\left(\frac{l_0}{l}\right)$$

DEFORM\_TEST - Compression : 1 s [step: 100]



**State Variable Distribution**

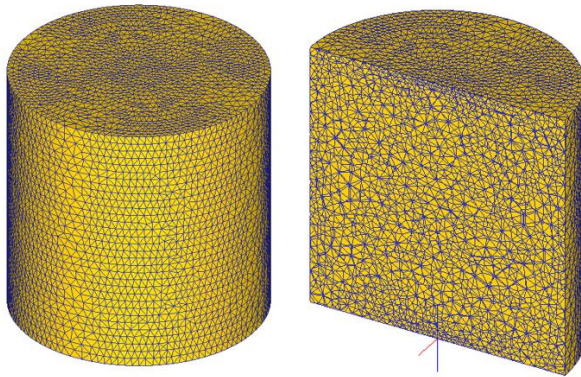


## A4. Mesh Study 4

### Mesh Generation; Detailed Settings

**No initial mesh changes are observed, none in the inside nor outside mesh.**

**Detailed Settings:**  
**System Setup > Weighting Factors**



Type:  System Setup  User Defined

General | **Weighting Factors** | Mesh Window | Coating

Surface Curvature:

Temperature Distribution:

Strain Distribution:

Strain Rate Distribution:

Mesh Density Windows:

Finer internal mesh

---

Summary

Number of Nodes	29745	Elements	157598
Surface Polygons	12280		

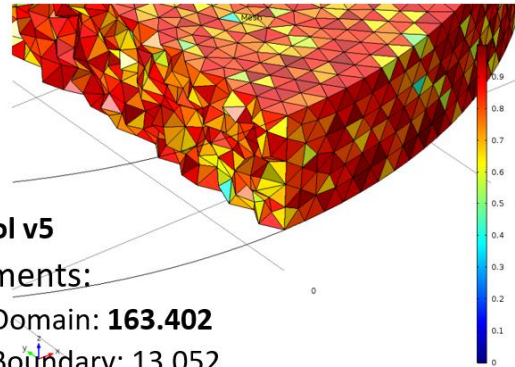
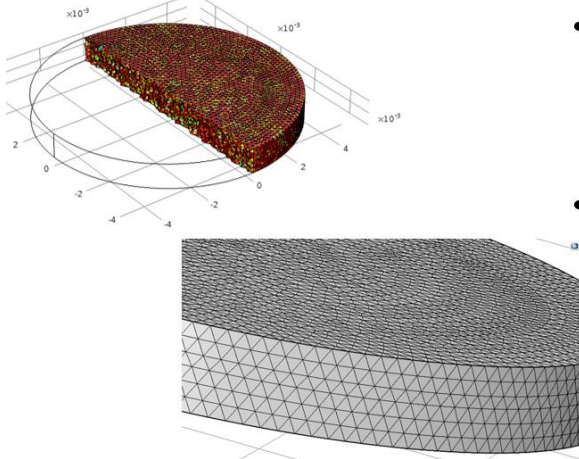


## A5. Mesh Study 5

### Import Mesh

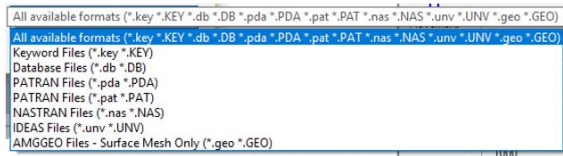
*NOTE: DEFORM HAS PROBLEMS WITH UNITS INTEGRATION*

#### COMSOL MESH GENERATED

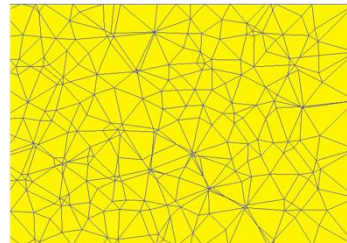


#### Comsol v5

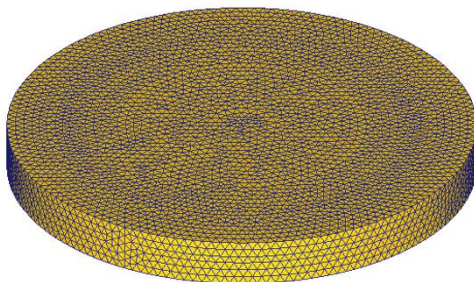
- Elements:
  - Domain: **163.402**
  - Boundary: 13.052
  - Edge elements: 340
- Mesh export : NASTRAN



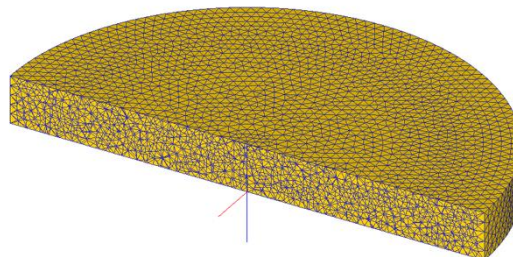
### Import Mesh



#### DEFORM MESH INTEGRATION



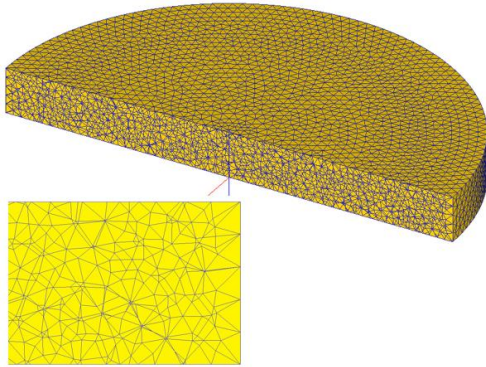
#### IMPORTED MESH SLICE



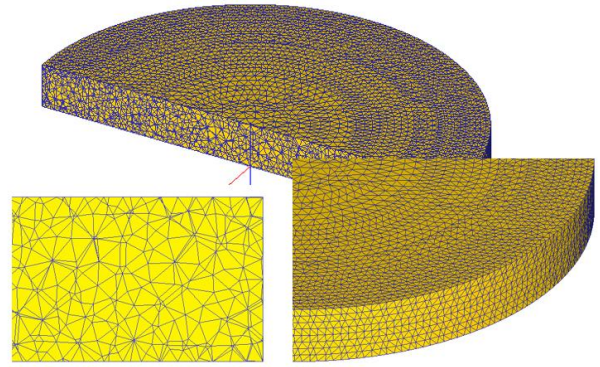
## Import Mesh .vs. Generated Mesh

*NOTE: BOTH CASES, NON HOMOGENEOUS INSIDE MESH*

**Imported Mesh (163.402 elements)**



**Generated Mesh (165.001 elements)**



### A6. Mesh Study 6

*NOTE: DEFORM IMPORTED MESH RUN PROVOKES THE CRUSH OF THE 3D MESH*

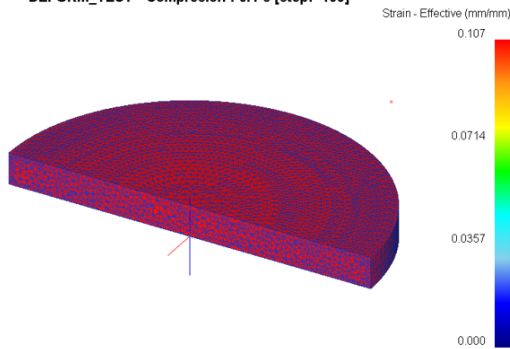
## FEM Simulation Results (No Remesh)

**Coulomb Friction : 0**  
 $l_0 = 1mm, l = 0.9mm$

DEFORM\_TEST - Compression : 0.1 s [step: 100]

**FEM Final Strain: 0.107**  
**Theoretical Strain : 0.1055**  
**Error : 0.14%**

$$\epsilon = \ln\left(\frac{l_0}{l}\right)$$



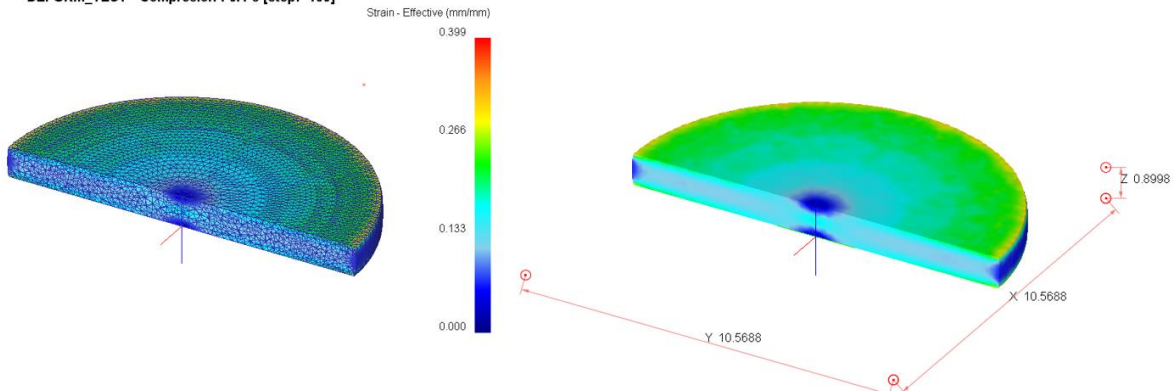
## FEM Simulation Results (No Remesh)

Coulomb Friction : 1.0  
 $l_0 = 1\text{mm}, l = 0.9\text{mm}$

Theoretical Strain : 0.1054

$$\varepsilon = \ln\left(\frac{l_0}{l}\right)$$

DEFORM\_TEST - Compression : 0.1 s [step: 100]



*NOTE: SIMILAR RESULTS AS ESTABLISHED FOR THE UNCONSTRAINT SIMULATIONS*

## FEM Simulation Results (No Remesh)

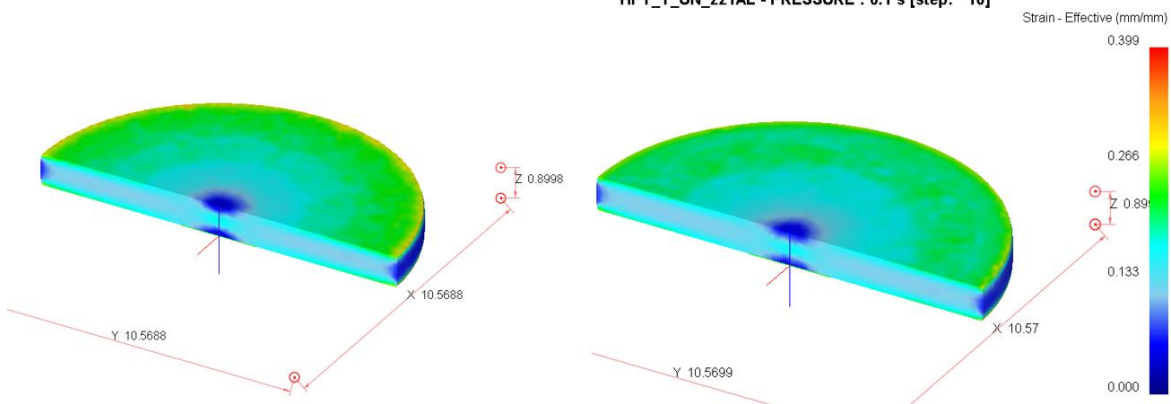
Coulomb Friction : 1.0  
 $l_0 = 1\text{mm}, l = 0.9\text{mm}$

Theoretical Strain : 0.1054

$$\varepsilon = \ln\left(\frac{l_0}{l}\right)$$

OBSERVATION : C. Friction : 0.61 (ALUMINIUM)

HPT\_T\_UN\_221AL - PRESSURE : 0.1 s [step: 10]

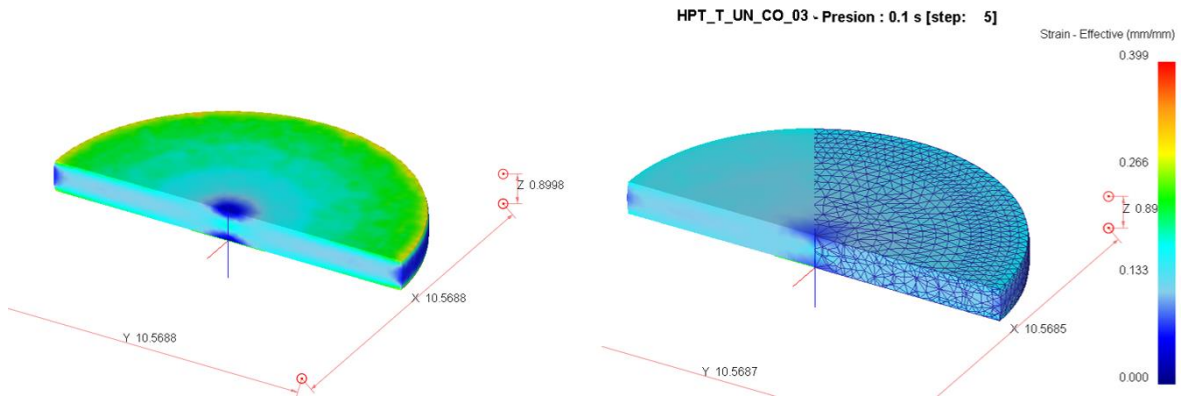


NOTE: SIMILAR RESULTS AS ESTABLISHED FOR THE UNCONSTRAINT SIMULATIONS

## FEM Simulation Results (No Remesh)

Coulomb Friction : 1.0  
 $l_0 = 1mm, l = 0.9mm$

Theoretical Strain : 0.1054  $\varepsilon = \ln\left(\frac{l_0}{l}\right)$   
 OBSERVATION : C. Friction : **0.51 (COPPER)**

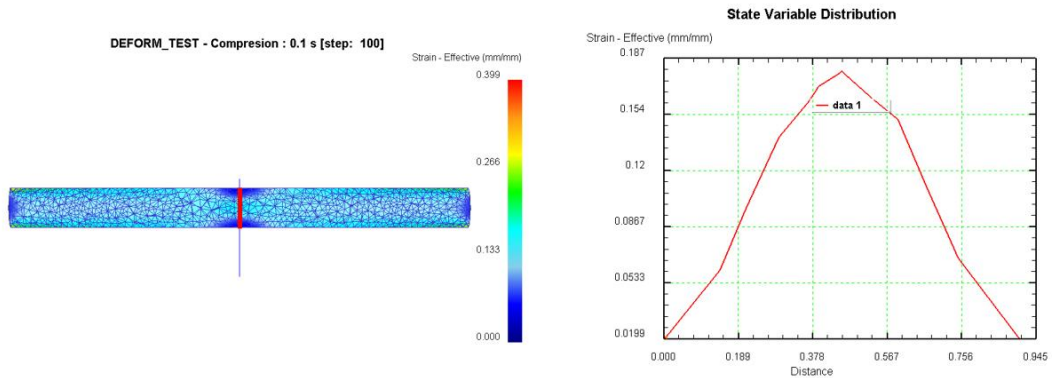


NOTE: DEFORM IMPORTED MESH RUN PROVOKES THE CRUSH OF THE 3D MESH

## FEM Simulation Results (No Remesh)

Coulomb Friction : 1.0  
 $l_0 = 1mm, l = 0.9mm$

Theoretical Strain : 0.1054  $\varepsilon = \ln\left(\frac{l_0}{l}\right)$





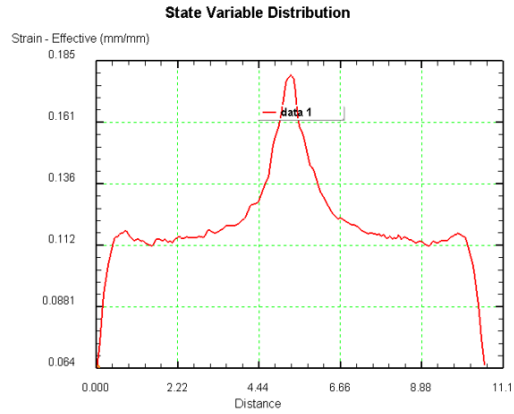
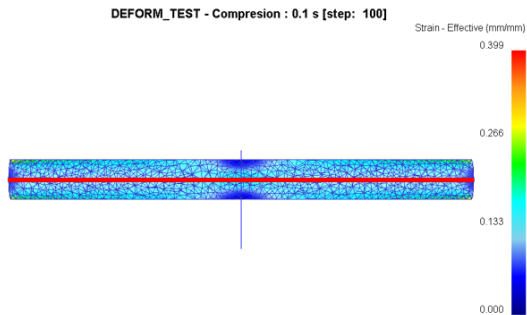
*NOTE: DEFORM IMPORTED MESH RUN PROVOKES THE CRUSH OF THE 3D MESH*

## FEM Simulation Results (No Remesh)

**Coulomb Friction : 1.0**  
 $l_0 = 1\text{mm} , l = 0.9\text{mm}$

**Theoretical Strain : 0.1054**

$$\varepsilon = \ln\left(\frac{l_0}{l}\right)$$



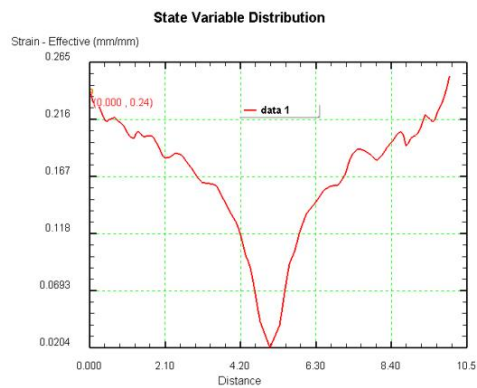
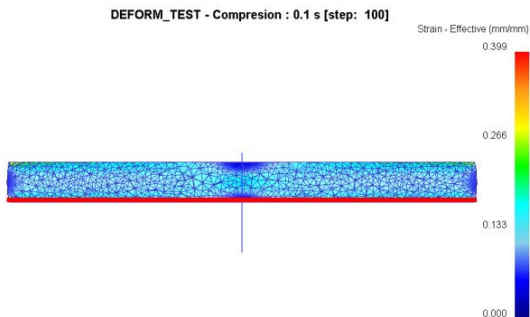
*NOTE: DEFORM IMPORTED MESH RUN PROVOKES THE CRUSH OF THE 3D MESH*

## FEM Simulation Results (No Remesh)

**Coulomb Friction : 1.0**  
 $l_0 = 1\text{mm} , l = 0.9\text{mm}$

**Theoretical Strain : 0.1054**

$$\varepsilon = \ln\left(\frac{l_0}{l}\right)$$

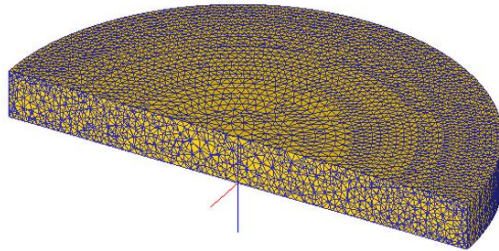




## A7. Mesh Study 7

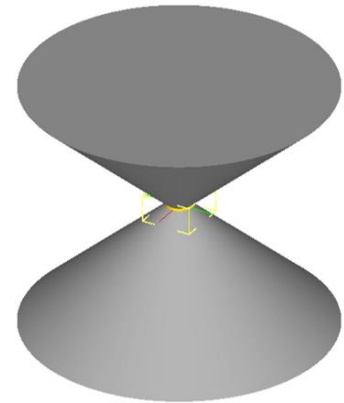
### Mesh evolution for 2 conic anvils

Coulomb Coefficient : 0.0



FEM Final Strain: 0.1055  
Theoretical Strain : 0.1054  
Error : 0.13%

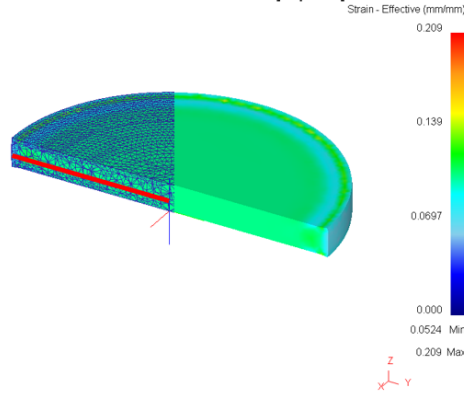
$$\varepsilon = \ln\left(\frac{l_0}{l}\right)$$



### Mesh evolution for 2 conic anvils (No Remesh)

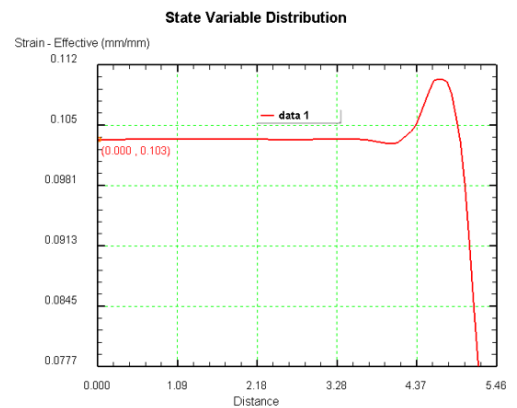
Coulomb Friction : 0.0  
 $l_0 = 1mm, l = 0.9mm$

DEFORM SIMULATION - OPERATION 1 : 0.1 s [step: 100]



FEM Final Strain: 0.1055  
Theoretical Strain : 0.1054  
Error : 0.13%

$$\varepsilon = \ln\left(\frac{l_0}{l}\right)$$

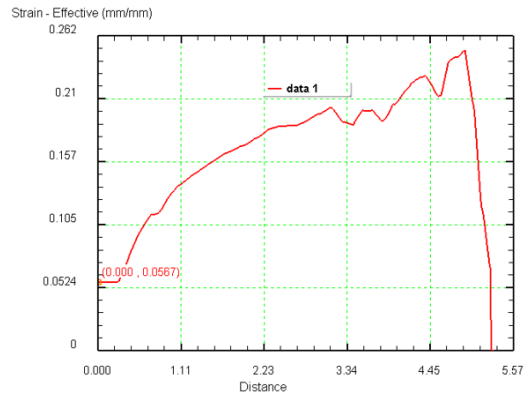
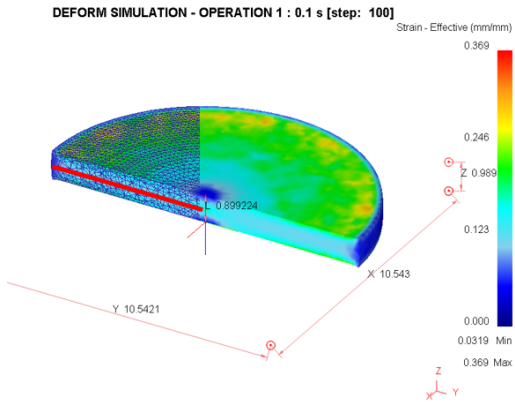


## Mesh evolution for 2 conic anvils (No Remesh)

Coulomb Friction : 1.0  
 $l_0 = 1\text{mm} , l = 0.9\text{mm}$

FEM Final Strain: 0.1055  
 Theoretical Strain : 0.1054  
 Error : 0.13%

$$\varepsilon = \ln\left(\frac{l_0}{l}\right)$$

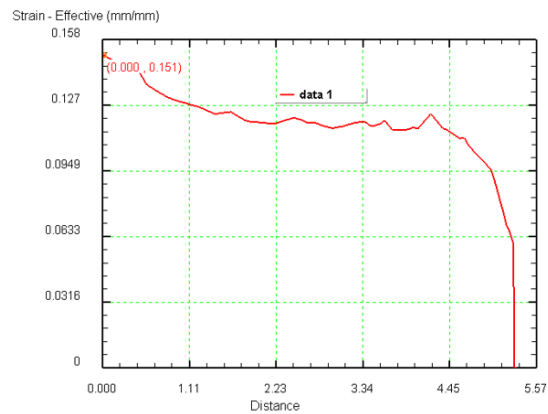
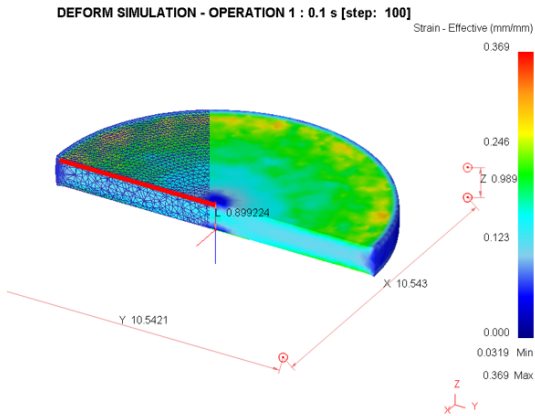


## Mesh evolution for 2 conic anvils (No Remesh)

Coulomb Friction : 1.0  
 $l_0 = 1\text{mm} , l = 0.9\text{mm}$

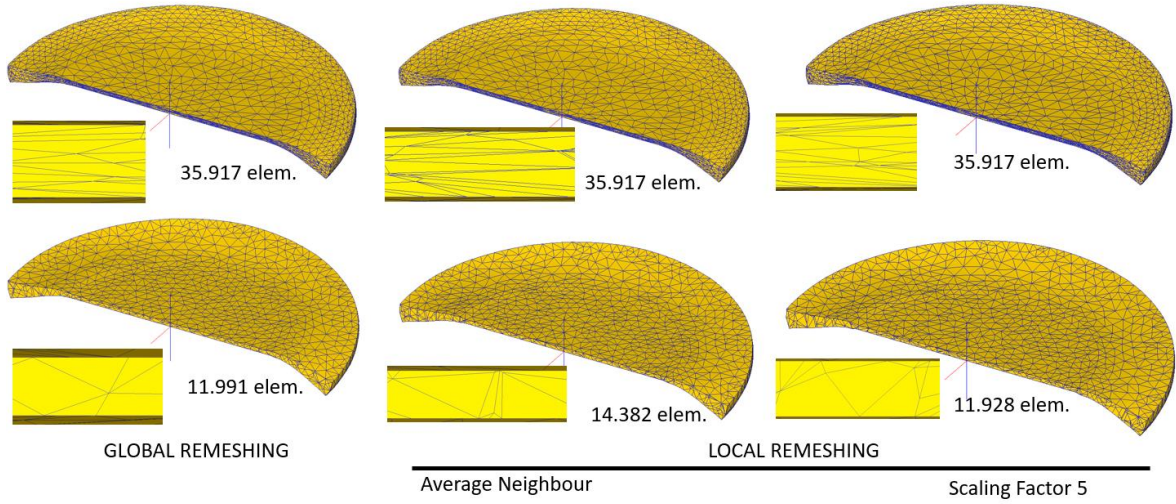
FEM Final Strain: 0.1055  
 Theoretical Strain : 0.1054  
 Error : 0.13%

$$\varepsilon = \ln\left(\frac{l_0}{l}\right)$$

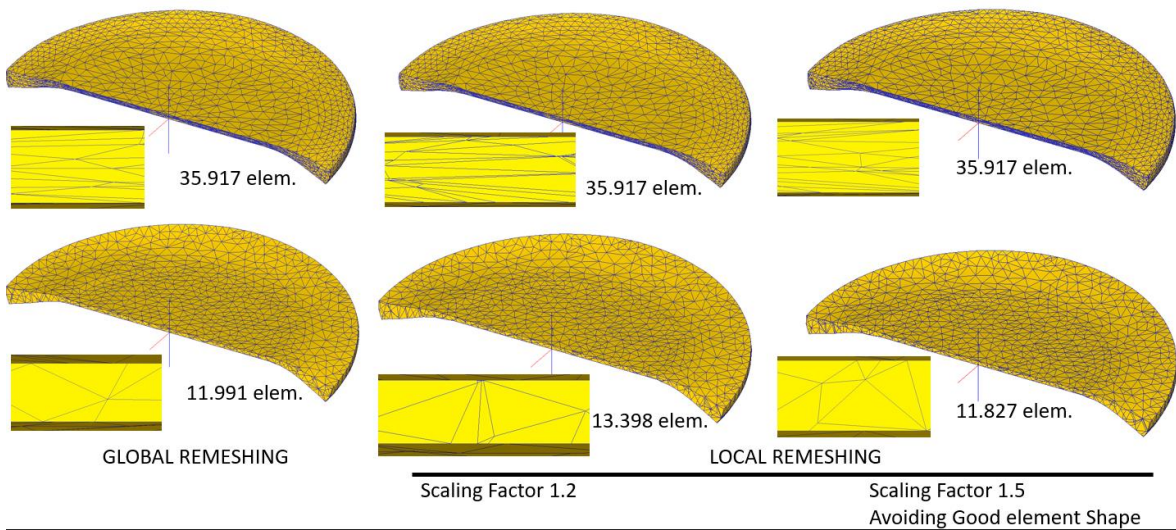


## A8. Mesh Study 8 : Re-mesh evolution

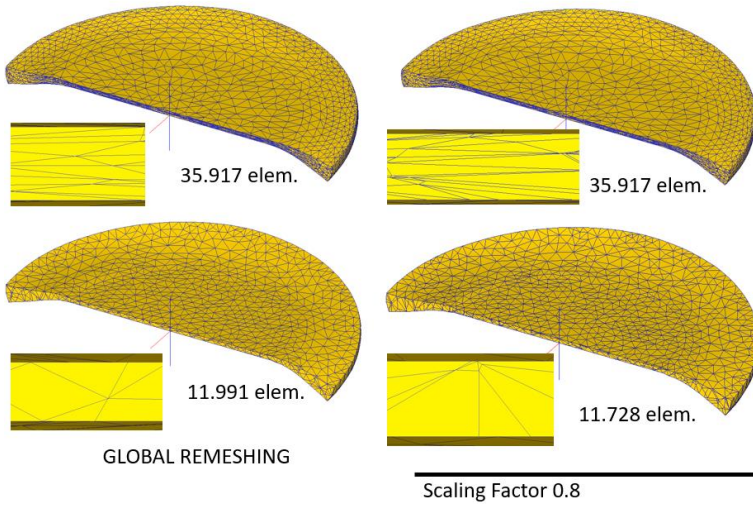
### Re-mesh comparison



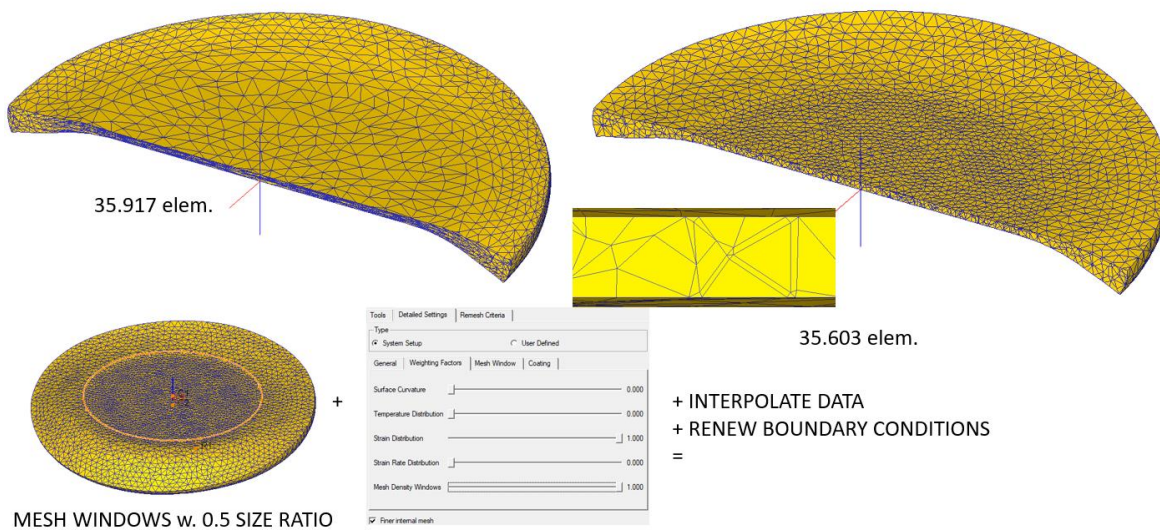
### Re-mesh comparison



## Re-mesh comparison



## Another solution : Manual remesh

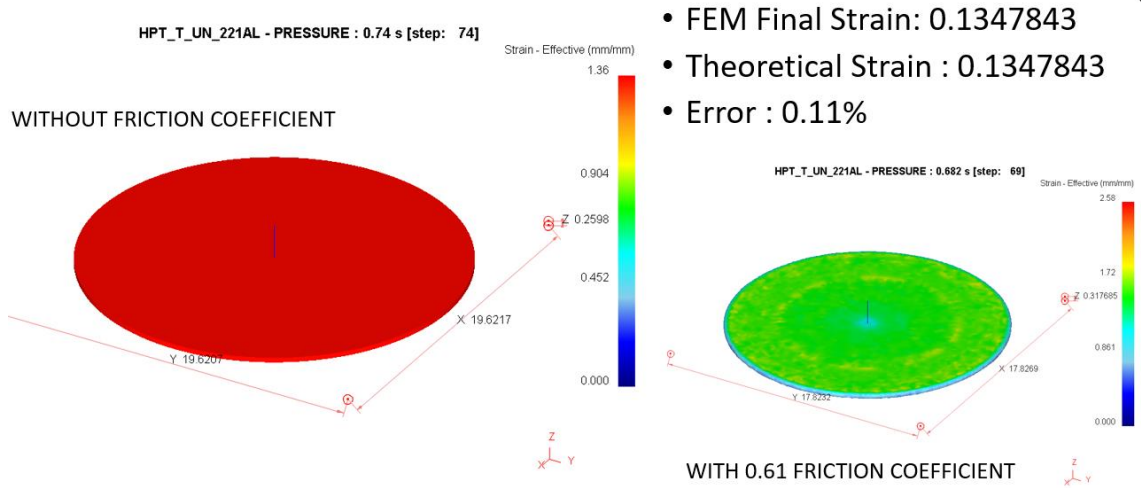




## A9. Mesh Study 9 : Friction Effect

### Unconstraint Compression without friction

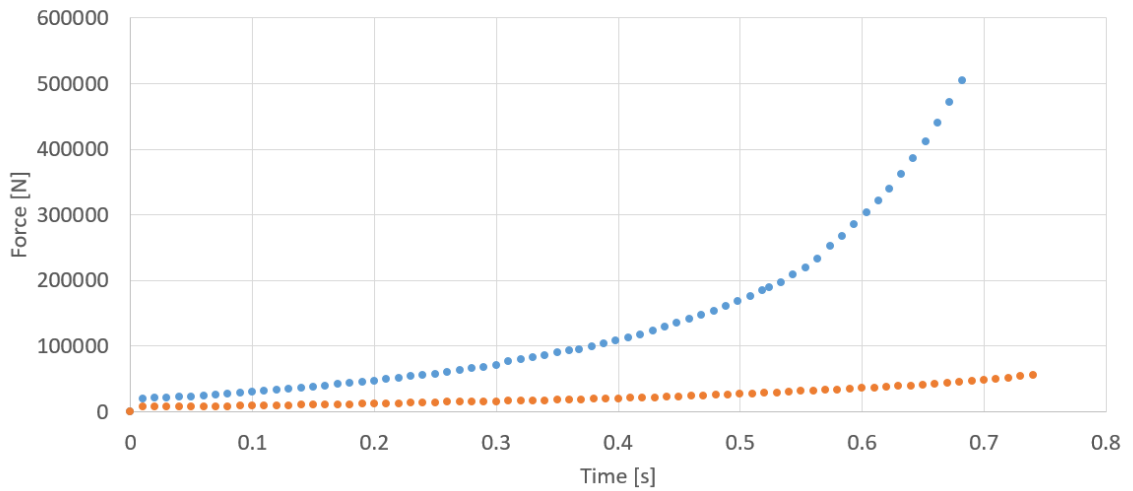
$$\varepsilon = \ln\left(\frac{l_0}{l}\right)$$



### Unconstraint Compression without friction

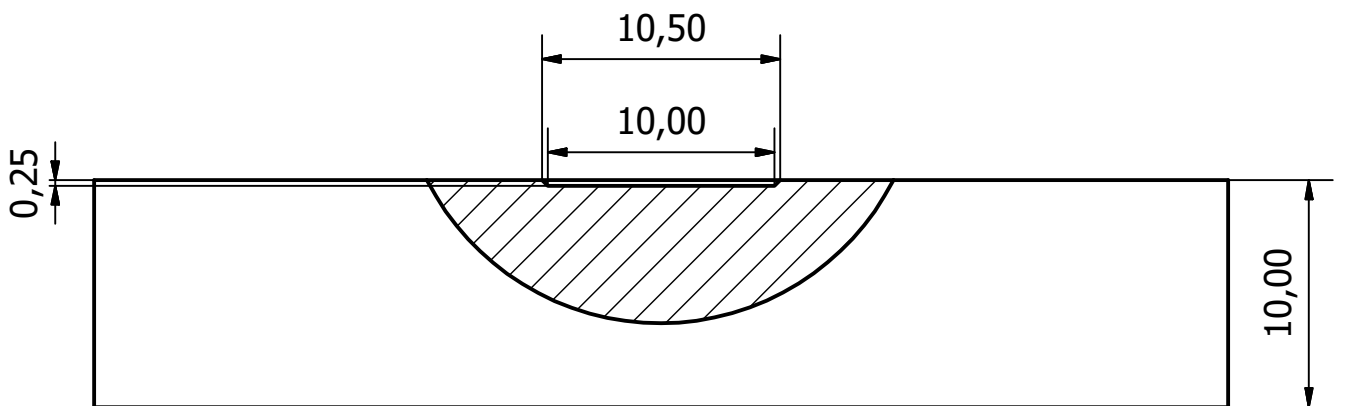
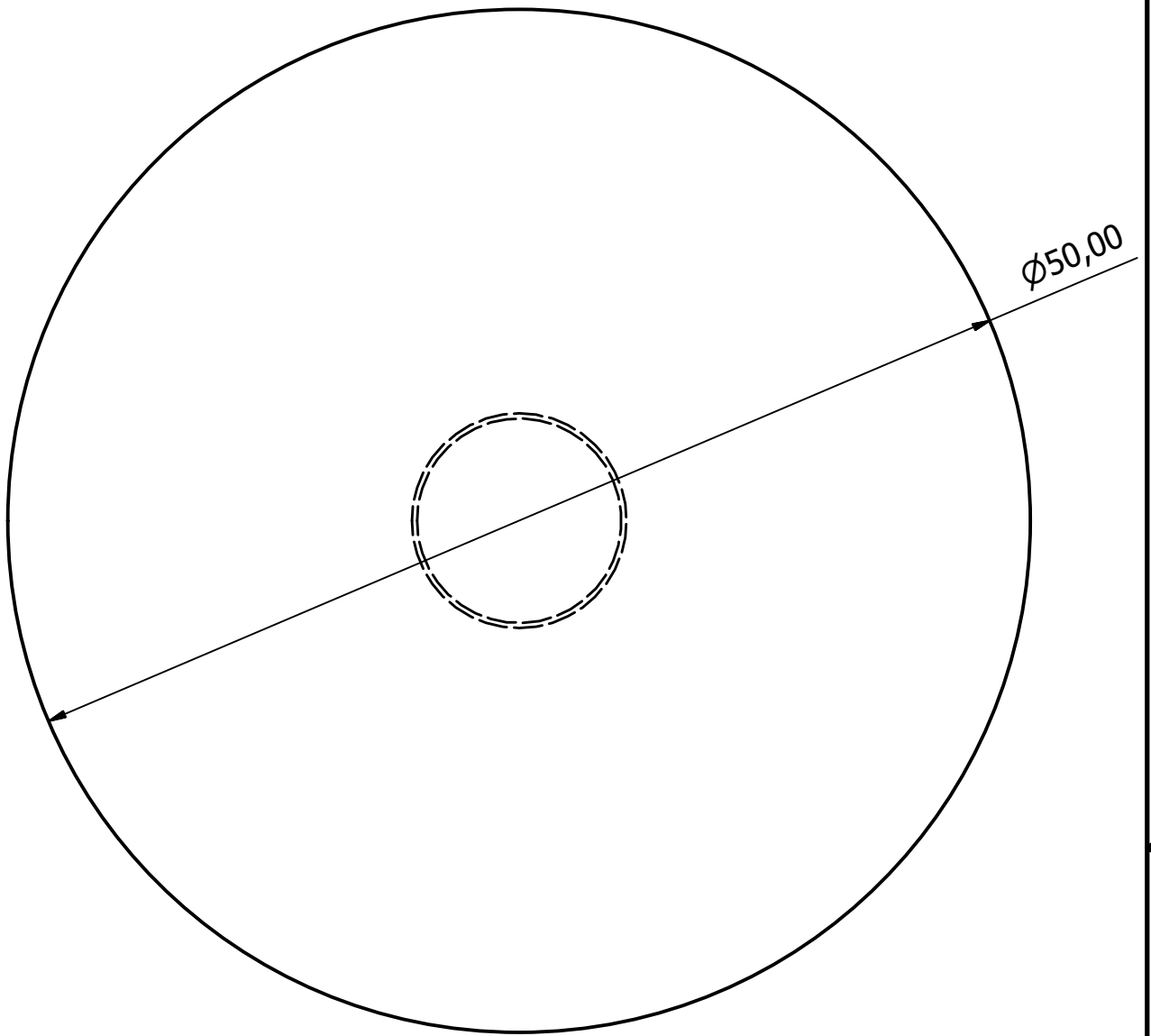
Force evolution along time stroke      1 mm = 1 second

• WITH FRICTION      • WITHOUT FRICTION




## Annex B. Technical Drawings

### B1. HPT Prelude & HPT Case 1 : Semi-Constraint B

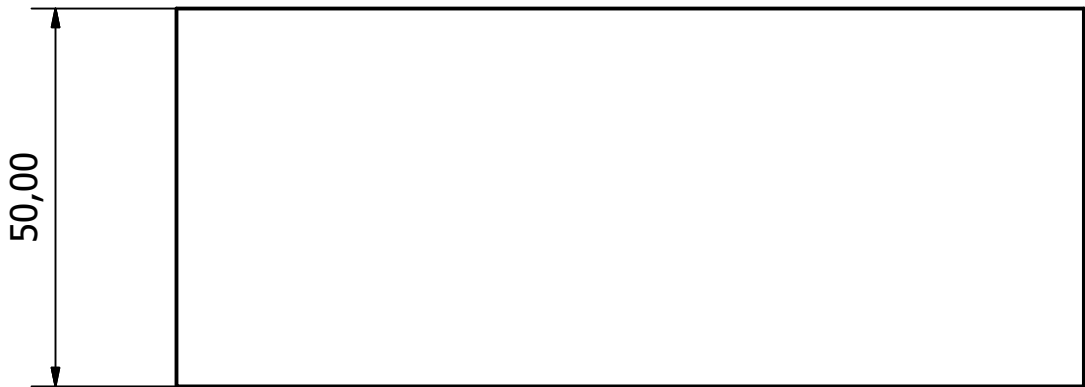
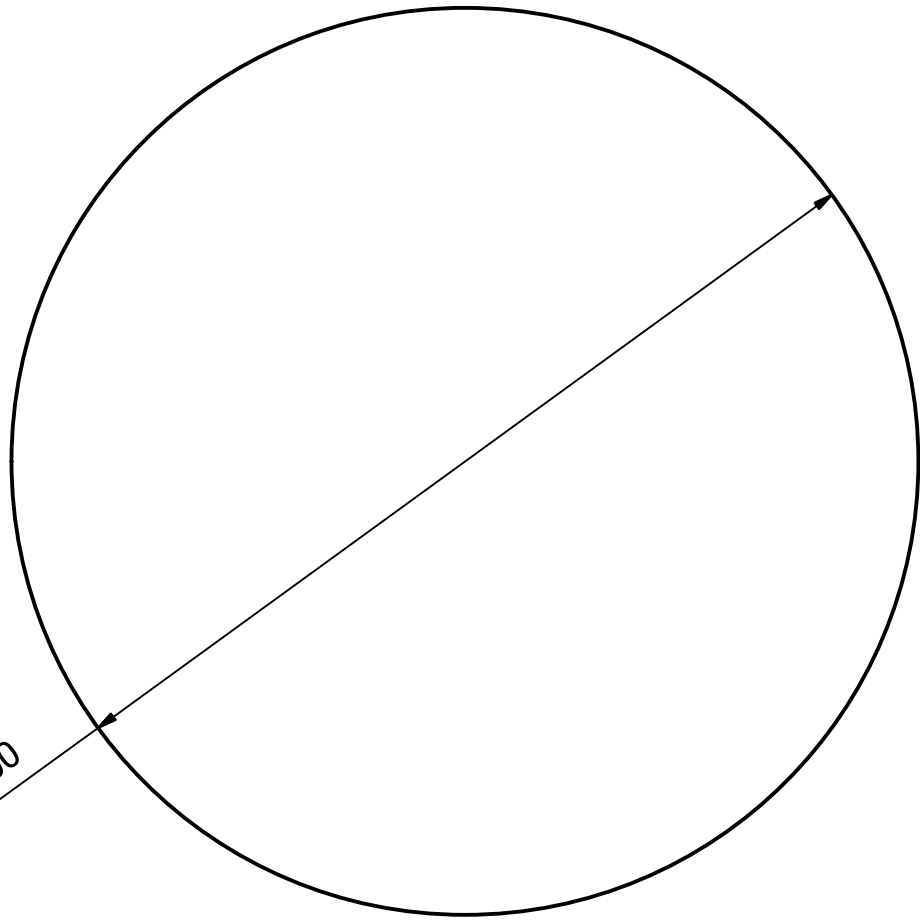


Designed by juanj	Checked by	Approved by Jose Ma Cabrera	Date	Scale 3:1	Date of creation 21/01/2018	Date of check
----------------------	------------	--------------------------------	------	--------------	--------------------------------	---------------


 EEBE - Escola d'Enginyeria Barcelona Est Observations	Design and Study of SPD Processes; HPT	
	HPT_SEMI-CON_B_DIES	Edition Sheet 1 / 1

## B2. HPT Case 2

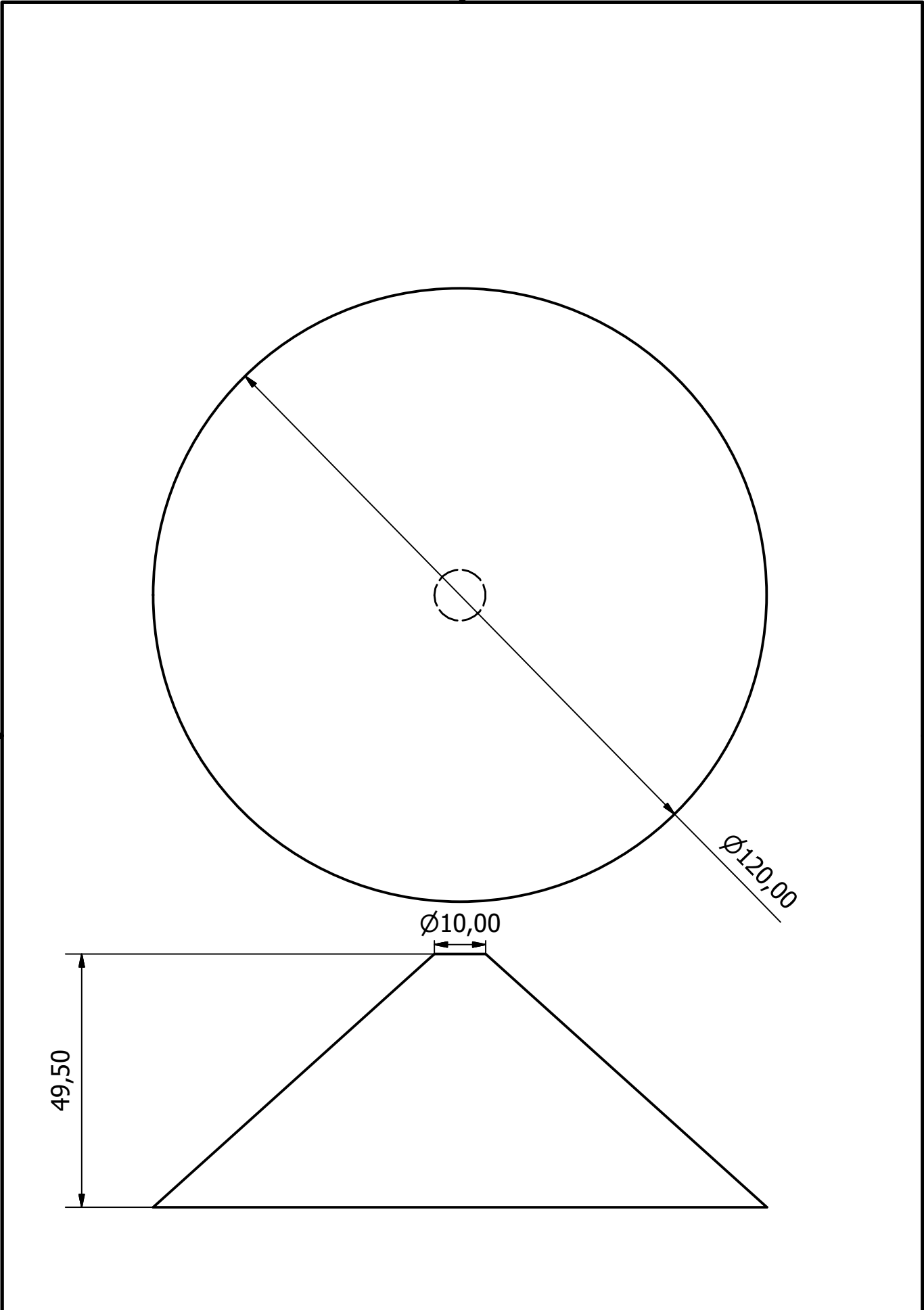





Designed by juanj	Checked by	Approved by <b>Jose M<sup>a</sup> Cabrera</b>	Date	Scale <b>1:1</b>	Date of creation 21/01/2018	Date of check
----------------------	------------	--	------	---------------------	--------------------------------	---------------

	EEBE - Escola d'Enginyeria Barcelona Est	Design and Study of SPD Processes; HPT	
	Observations	HPT_UNCON_IDEAL_DIES	Edition Sheet <b>1 / 1</b>





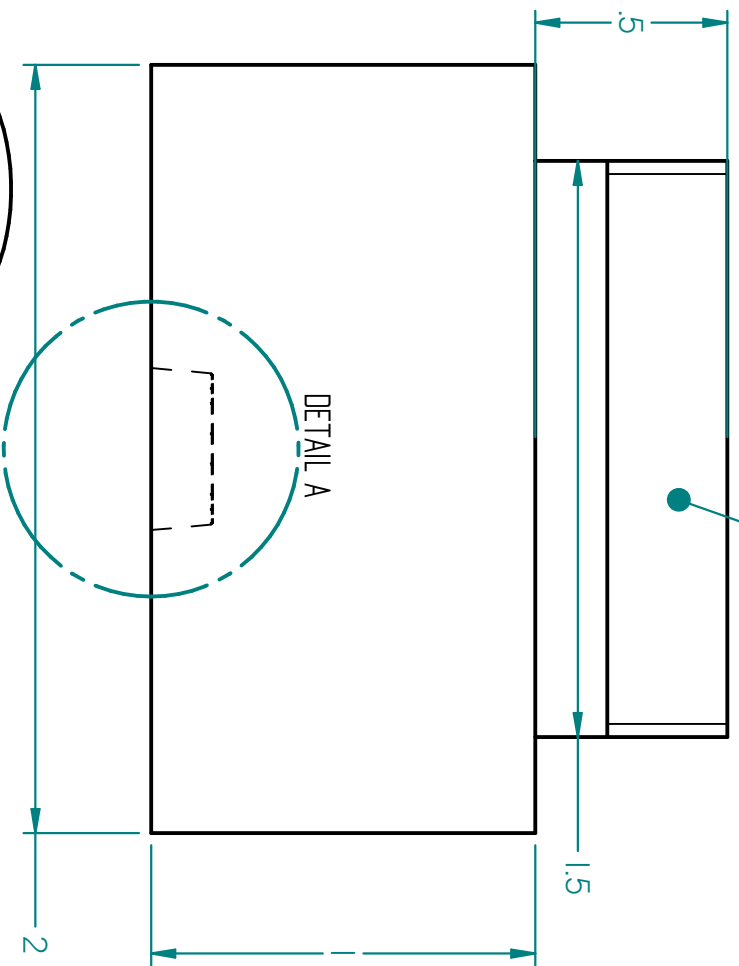
Designed by juanj	Checked by	Approved by <b>Jose M<sup>a</sup> Cabrera</b>	Date	Scale <b>1:1</b>	Date of creation 21/01/2018	Date of check
----------------------	------------	--	------	---------------------	--------------------------------	---------------


 EEBE - Escola d'Enginyeria Barcelona Est  
 Observations

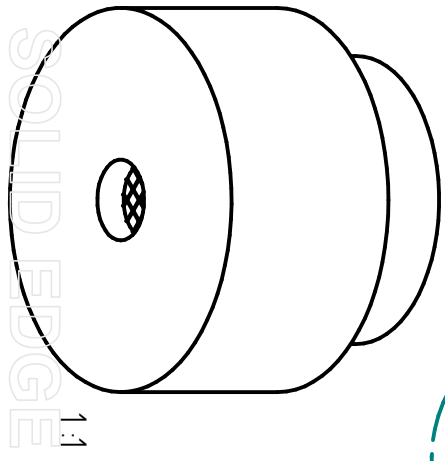
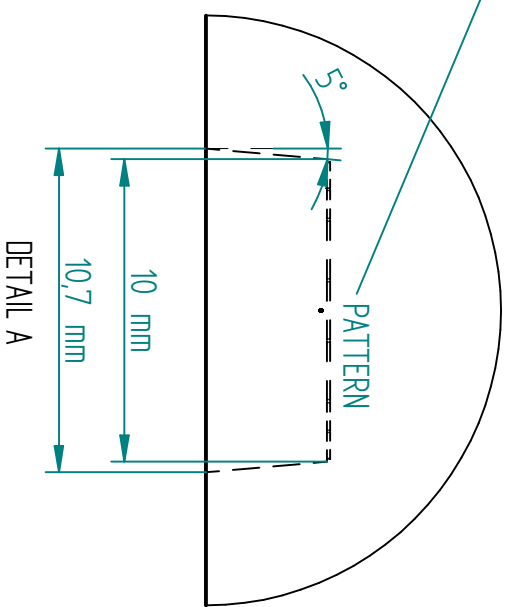
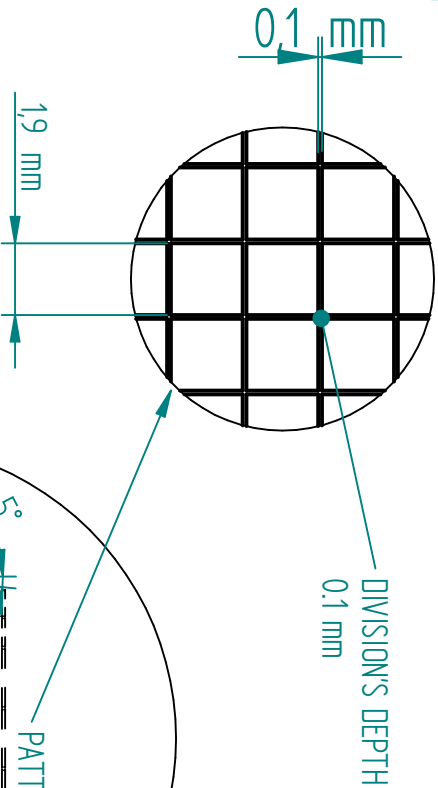
Design and Study of SPD Processes; HPT	
HPT_UNCON_REAL_DIES	Edition Sheet <b>1 / 1</b>

### B3. HPT Case 3

THREAD:  
12 [THREADS/INCH]  
FOR 5/16 [INCH]



REVISION HISTORY			
REV	DESCRIPTION	DATE	APPROVED



1:1

SOLID EDGE ACADEMIC COPY

	NAME	DATE	TITLE
DRAWN	Sebastián	26/Sep/17	<b>HPT_BS Adaptor</b>
CHECKED			
ENG APPR			
MGR APPR			

UNLESS OTHERWISE SPECIFIED DIMENSIONS ARE IN INCHES		FILE NAME: HPT_Bulk_Stat.dft	SCALE: 2:1	WEIGHT:	SHEET 1 OF 1
BASED ON	Horita Z, Langdon T.G. Achieving exceptional superplasticity in a bulk aluminum alloy processed by high-pressure torsion. Scripta Materialia, 58 (2008) p. 1029-1032.	SIZE	DWG NO	2	REV
		A4			





